Search for Axion-Like Dark Matter and Exotic Yukawa-Like Interaction

Inauguraldissertation
der Philosophisch-naturwissenschaftlichen Fakultät
der Universität Bern

vorgelegt von
Ivo Schulthess
von Melchnau (BE)

Leiter der Arbeit:
Prof. Dr. Florian M. Piegsa
Albert Einstein Center for Fundamental Physics
Laboratorium für Hochenergiephysik
Physikalisches Institut

Search for Axion-Like Dark Matter and Exotic Yukawa-Like Interaction

Inauguraldissertation
der Philosophisch-naturwissenschaftlichen Fakultät
der Universität Bern

vorgelegt von
Ivo Schulthess
von Melchnau (BE)

Leiter der Arbeit:
Prof. Dr. Florian M. Piegsa
Albert Einstein Center for Fundamental Physics
Laboratorium für Hochenergiephysik
Physikalisches Institut

Von der Philosophisch-naturwissenschaftlichen Fakultät angenommen.

Bern, 7. Dezember 2022

Der Dekan
Prof. Dr. Marco Herwegh

Abstract

Despite the undoubted success of the Standard Model of particle physics, it fails to answer many longstanding questions, such as the strong *CP* problem, the observed effects of dark matter, and the baryon asymmetry in our universe. Many theoretical models that try to answer those questions require new particles and gauge bosons which have to be verified or excluded experimentally.

Here, we present the search for two such candidates. The first candidate is an ultralight pseudo-scalar particle called axion or axion-like particle (ALP). We searched for them using a Ramsey-type apparatus for cold neutrons. A hypothetical coupling of ALPs to gluons would manifest itself in a neutron electric dipole moment signal oscillating in time. Twenty-four hours of data have been analyzed in a frequency range from $23\ \mu\mathrm{Hz}$ to $1\ \mathrm{kHz}$, and no significant oscillating signal has been found. The usage of present dark-matter models allows for constraining the coupling of ALPs to gluons in the mass range from 10^{-19} to $4 \times 10^{-12}\ \mathrm{eV}$. This extends the previously tested range by over three orders of magnitude. The best limit of $C_G \ / \ f_a m_a = 2.7 \times 10^{13}\ \mathrm{GeV}^{-2}$ $(95\%$ C.L.) is reached in the mass range from 2×10^{-17} to $2 \times 10^{-14}\ \mathrm{eV}$. Together with the results of two other laboratory experiments, a large region of the ALP-gluon coupling parameter space could be excluded.

The second candidate is an axial-vector gauge boson that could mediate a Yukawa-like interaction in the millimeter range between Standard Model fermions like protons, neutrons, and electrons. We built a tabletop experiment that applies Ramsey's technique to the proton spins of hydrogen in water. We performed a proof-of-principle search for this exotic interaction for the first time using protons as probe particles. Even though we could not yet detect or constrain the existence of such an interaction with statistical arguments, developments of the apparatus are underway that will allow to do this in the near future. With the apparatus we additionally investigated radio-frequency effects like the Bloch-Siegert shift and dressed spin states. This is to our knowledge the first time that the dressed spin states of protons were measured.

Zusammenfassung

Trotz des unbestrittenen Erfolgs des Standardmodells der Teilchenphysik scheitert es seit langem bei der Beantwortung einiger Fragen. Dazu gehören das Problem der fehlenden *CP*-Verletzung in der starken Wechselwirkung (engl.: strong *CP* problem), eine fehlende Erklärung für die beobachteten Effekte der Dunklen Materie und die Asymmetrie zwischen Materie und Antimaterie im Universum. Viele theoretische Modelle, die versuchen diese Fragen zu beantworten, erfordern neue Teilchen und Wechselwirkungen. Diese müssen experimentell nachgewiesen oder ausgeschlossen werden.

In dieser Arbeit beschreiben wir die Suche nach zwei möglichen Kandidaten. Der erste Kandidat ist ein ultraleichtes, pseudoskalares Teilchen, das Axion oder axionähnliches Teilchen (engl.: axion-like particle, ALP) genannt wird. Danach suchten wir mit kalten Neutronen und einer Ramsey-Apparatur. Die hypothetische Wechselwirkung der ALPs zu den Gluonen würde in einem zeitlich oszillierenden elektrischen Dipolmoment des Neutrons resultieren. Wir analysierten Daten, die über einen Zeitraum von 24 Stunden gemessen wurden. In einem Frequenzbereich zwischen $23\ \mu\mathrm{Hz}$ und $1\ \mathrm{kHz}$ konnten wir kein oszillierendes Signal feststellen. Mittels aktueller Modelle der Dunklen Materie konnten wir jedoch die Wechselwirkung zwischen den ALPs, mit Massen zwischen 10^{-19} und $4\times10^{-12}\mathrm{eV}$, und den Gluonen einschränken. Dies erweiterte den bisher untersuchten Massenbereich um über einen Faktor Tausend. Der beste Grenzwert der Wechselwirkung von $C_G/f_a m_a = 2.7\times10^{13}\mathrm{GeV}^{-2}$ $(95\%$ KI) konnte für Massen zwischen 2×10^{-17} und $2\times10^{-14}\mathrm{eV}$ bestimmt werden. Zusammen mit den Resultaten zweier weiterer Laborexperimente kann die Wechselwirkung der ALPs zu Gluonen somit in einem grossen Teil des Phasenraums ausgeschlossen werden.

Der zweite Kandidat ist axialvektorielles Eichboson, das eine Yukawa-ähnliche Kraft zwischen Standardmodell-Fermionen wie Protonen, Neutronen und Elektronen auf der Längenskala von Millimetern vermitteln könnte. Wir entwickelten und bauten ein Kleinstexperiment, welches die Ramsey-Methode an den Spins der Wasserstoff-Protonen im Wasser anwendet. Wir untersuchten die Machbarkeit der Messung dieser exotischen Wechselwirkung. Zum ersten Mal wurden für eine solche Suche Protonen verwendet. Obwohl wir die Existenz dieser Kraft nicht nachweisen oder statistisch signifikant einschränken konnten, wird eine Erweiterung des Experiments dies in naher Zukunft ermöglichen. Wir untersuchten zudem Hochfrequenz-Effekte wie die Bloch-Siegert Frequenzverschiebung und die verkleideten Spin-Zustände (engl.: dressed spin states). Unseres Wissens wurden letztere zum ersten Mal an Protonen gemessen.

Contents

Part I

Axion-Like Dark Matter

1 Introduction

Despite the undoubted success of the Standard Model of particle physics (SM), it fails to answer many longstanding questions. They include, the observed effects of dark matter and the baryon asymmetry in our universe [1]. Many new theoretical models that try to answer those questions require new particles and forces. Their existence has to be verified or excluded experimentally. One group of new particles are light spin-0 particles that interact with the SM particles. They can be *CP*-even or *CP*-odd and are then called scalar or pseudoscalar, respectively. A subgroup of the latter which are massive but ultra-light is also known as axions or axion-like particles (ALPs) [2].

In the following part of this thesis we report on the search for ALPs using cold neutrons. First, we introduce the axion and the more general group of ALPs. We also summarize experimental searches for ALPs in different mass regions and with various approaches. Additionally, we explain some constraints from cosmology and astrophysics. In Sec. 2 we elucidate the *Beam EDM* apparatus that was used to search for the ALPs with cold neutrons. We then describe in detail the measurements that we performed to characterize the apparatus and to deduce its sensitivity to ALPs in Sec. 3. At last in Sec. 4, we show the analysis of the neutron data, the results of the search, and summarize in Sec. 5.

This search for the axion-like dark matter led to new constraints and many sections throughout Part I of the thesis can be found in the preprint on arXiv [3]. The manuscript has been accepted by *Physical Review Letters* on the 26th of September, 2022.

1.1 The Axion and Axion-Like Particles

The axion was initially suggested to solve the strong *CP* problem of quantum chromodynamics (QCD) [4–7]. One part of the QCD Lagrangian is the well-known θ term

$$\mathcal{L}_\theta = \theta \frac{g^2}{32\pi^2} G_c^{\mu\nu} \tilde{G}_{\mu\nu}^c, \tag{1}$$

where θ is the vacuum angle/phase, $G_c^{\mu\nu}$ the gluon field tensor with color index c, $\tilde{G}_{\mu\nu}^c = \frac{1}{2}\epsilon_{\mu\nu\rho\sigma}G_c^{\rho\sigma}$ with $\epsilon_{\mu\nu\rho\sigma}$ the rank-4 Levi-Civita symbol, and g the coupling strength of the quark field to the gluon fields. This Lagrangian is renormalizable and gauge invariant, but not *CP* invariant. A problem appears from the measurement of the neutron electric dipole moment (EDM). It is connected to the θ term via $d_n = 2.4 \times 10^{-16}\,\bar{\theta} e\,\mathrm{cm}$, where $\bar{\theta} = \theta + \arg\det M$ includes the weak interaction with M being the quark mass matrix [8, 9]. The latest measurement of $|d_n| < 1.8 \times 10^{-26}\,e\,\mathrm{cm}$ at a confidence level (C.L.) of 90% [10] implies that $\left|\bar{\theta}\right| \lesssim 10^{-10}$. Although any value in the range $-\pi < \bar{\theta} < \pi$ would be perfectly fine, the question of why $\bar{\theta}$ is so small without any known mechanism remains a fine-tuning problem and is called the strong *CP* problem.

One solution to the strong *CP* problem (besides e.g. a zero mass quark and a $\bar{\theta} = 0$ solution) is an additional chiral $U(1)_{\mathrm{PQ}}$ symmetry to the SM [4, 5]. This was suggested by R. Peccei and H. Quinn and is the most promising solution since over 40 years. The spontaneous and explicit breaking of this symmetry results in a massive but ultra-light spin-0 pseudo-Nambu-Goldstone boson, the axion. Due to this $U(1)_{\mathrm{PQ}}$ symmetry, the QCD Lagrangian gets the new terms

$$\mathcal{L}_{\text{axion}} = \underbrace{-\frac{1}{2}\partial_\mu a \partial^\mu a}_{\mathcal{L}_{\text{kin}}} + \underbrace{C_G \frac{a}{f_a}\frac{g^2}{32\pi^2} G_c^{\mu\nu}\tilde{G}^c_{\mu\nu}}_{-V_{\text{eff}}} + \mathcal{L}_{\text{int}}\left[\frac{\partial_\mu a}{f_a}; \psi\right] \ , \tag{2}$$

where a is the axion field, C_G a model-dependent parameter, and f_a the axion decay constant. Here, the first part describes the axion kinematics, the second part represents an effective potential and ensures that the symmetry has the chiral anomaly, and the last term are further interactions that are model dependent. There exist two well-known axion models that suggest interactions with other particles such as SM fermions (DFSZ model [11, 12]) or a new exotic heavy quark (KSVZ model [13, 14]).

When calculating the vacuum expectation value from the effective potential of $\mathcal{L}_{\text{axion}}$, it has a minimum at $\langle a \rangle = -\frac{f_a}{C_G}\bar{\theta}$ which cancels the $\bar{\theta}$ term in the QCD Lagrangian and, therefore, solves the strong *CP* problem [15].

The mass of the axion can be calculated by chiral perturbation theory including quantum electrodynamics (QED) and next-to-next-to-leading order corrections: [16]

$$m_a = (5.691 \pm 0.051)\left(\frac{10^9\ \text{GeV}}{f_a}\right)\ \text{meV} \ . \tag{3}$$

It is clear from Eq. (3) that the relation between the mass and the decay constant is fixed for the axion. There are a few theories that also allow other masses than Eq. (3) such as the recently developed $\mathcal{Z}_{\mathcal{N}}$ model [17–19]. There exists also a more general class of ALPs where the the mass and decay constant are independent. These particles can not solve the strong *CP* problem, but explain other phenomena.[a]

One of those phenomena is dark matter which makes up roughly 27% of our universe's

---

[a] Note that the terms axion and axion-like particle (ALP) are often used interchangeably. Strictly speaking, the axion is only the QCD-axion that solves the strong *CP* problem and all other particles should be referred to be ALPs.

total mass-energy content [20].[b] So far, no dark-matter model has been experimentally verified, but promising candidates remain the ALPs. Since this pseudo-scalar particle must satisfy the Klein-Gordon equation, it results in an oscillating field. Because they are ultra-light, they are stable on cosmological time scales and could therefore explain the dark-matter content in our universe [21–25].

Besides being a solution to the strong *CP* problem and an explanation for dark matter, ALPs could also serve as an explanation for the baryogenesis [26, 27]. This may be called axiogenesis. The baryogenesis is the hypothetical physical process that led to the matter-antimatter asymmetry in the early universe. In the higher MeV to GeV mass range, they are not long-lived enough to be relevant for cosmology but could serve as an explanation for the muon's anomalous magnetic moment or as a portal to the dark sector [28, 29].

With the axion model, the strong *CP* problem is solved dynamically. In other words, the physically observable parameter $\bar{\theta}$ is converted into the form of an oscillating axion field and thus leading to an oscillating neutron EDM [30]

$$d_n^a(t) \approx 2.4 \times 10^{-16}\, e\,\mathrm{cm} \cdot \frac{C_G}{f_a} a_0 \cos\left(m_a t\right) \,, \tag{4}$$

where a_0 is the axion oscillation amplitude and e the elementary charge. Note that this term is independent of the value of the constant neutron EDM.

The parameter space of ALPs is defined by their mass and the decay constant C_G/f_a. It is restricted by various laboratory searches and astrophysical/cosmological constraints that are summarized in Sec. 1.2 and Sec. 1.3, respectively.

1.2 Experimental Searches

There are various types of ALP searches. A recent summary can be found in the review of particle physics [31] and a comparison of published results and projections in the repository of C. O'Hare [32].

Most experiments make use of the coupling to photons and their constraints and projections are summarized in Fig. 1. Helioscope experiments like CAST or the planned IAXO at CERN [33] search for ALPs from the sun in the sub-eV mass range. Haloscope experiments, such as ADMX at the University of Washington [34], use resonant microwave cavities to search for axion dark matter in the local galactic halo of the Milky Way. Their target

---

[b] The two reported numbers in the Planck 2018 report are the Hubble constant $H_0 \equiv 100h\ \mathrm{kms}^{-1}\mathrm{Mpc}^{-1} = 67.32\ \mathrm{kms}^{-1}\mathrm{Mpc}^{-1}$, where h is a dimensionless cosmological parameter, and the cold-dark-matter density parameter $\Omega_c h^2 = 0.12011$. Together, this leads to the dark-matter mass-energy content of $\Omega_c = 0.268$.

masses are in the $\mu\mathrm{eV}$ regime. Another type of experiment is the ALPS-I/II at DESY [35]. It is a light-shining-through-wall experiment where ALPs are produced and measured in the laboratory using high-power laser cavities and strong magnetic fields.

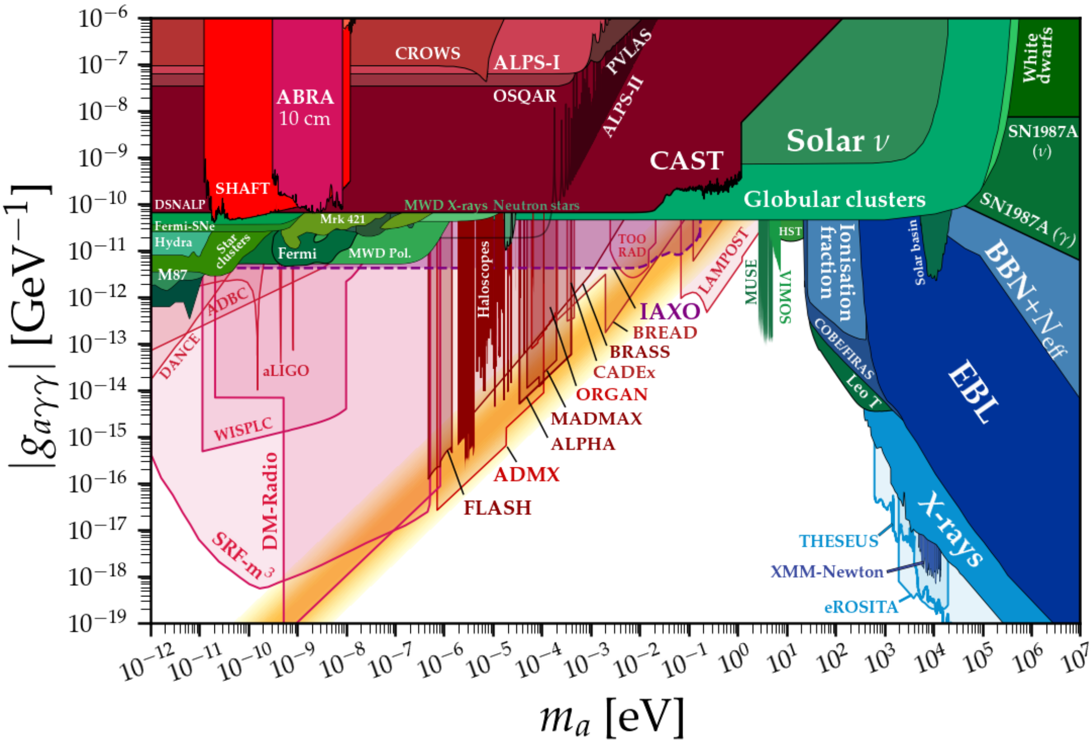

Figure 1: *Constraints of the coupling of ALPs to photons. Shown is the coupling as a function of the mass for various experiments (red), astrophysical (green), and cosmological (blue) observations. The QCD-axion band is shown in yellow. The light shaded areas correspond to projections and the opaque areas to experimental constraints. Different assumptions, uncertainties, and C.L. may have been applied. Picture courtesy of C. O'Hare [32].*

There are also collider experiments such as Belle-II at SuperKEKB, searching for the production of ALPs in the MeV to GeV range in e^+e^- collisions [36]. In the high-energy collisions, the ALPs are produced and almost immediately decay into two photons which can be detected.

Beam dump experiments also cover a mass range in the MeV to GeV regime. In these experiments, a particle beam, usually protons or electrons, collides with a high-Z target, e.g., copper. Due to the interaction of the particles with the target nuclei, new particles can be created via the Primakoff process [37]. Because of their weak coupling to the SM sector, they acquire a long enough lifetime to leave the target. On their way to the detector that is placed a few meters up to hundreds of meters away, they decay back to SM particles, such as two photons. These decay particles can be measured and related to the new particle. An example of such an experiment is the NA62-dump at the Super Proton Synchrotron at CERN [38]. Another example of a similar search is the FASER detector [39]. It is searching for new physics behind the neutral particle absorber after the ATLAS interaction point at the LHC. They are looking for various types of particles, including scalar and pseudo-scalar particles with photon dominance.[c] A summary of all beam dump experiments at CERN can be found in the Physics Beyond Colliders initiative report [40].

Various experiments search for ALPs via their coupling to the EDM of particles. The CASPEr experiment at the University of Mainz is dedicated to searching for an axion signal using nuclear magnetic resonance techniques in a solid-state-EDM experiment. The collaboration recently published an upper limit in a narrow frequency band around $39\ \mathrm{MHz}$ [41, 42]. Two other experiments, nEDM at the Paul Scherrer Institut (PSI) and HfH$^+$-EDM at the University of Colorado, search for a permanent EDM of the the neutron, using ultra-cold neutrons in a storage experiment, and the electron, using trapped molecular ions. Both experiments analyzed their data for oscillating signals. However, no significant signal from the nHz-region up to $0.4\ \mathrm{Hz}$ was found [43, 44]. Another proposed experiment is the deuteron storage ring EDM. They plan to test a frequency range from $10^{-9}\ \mathrm{Hz}$ to $10^{8}\ \mathrm{Hz}$ [45].

Here, we present the results of the *Beam EDM* experiment, which employs a continuous cold neutron beam with intrinsic sub-ms time resolution [46, 47]. Thus, the accessible frequency range is extended to $1\ \mathrm{kHz}$. This allowed us to probe for ALP masses more than three orders of magnitude heavier than tested by previous EDM laboratory experiments.

It is important to notice that searches for an oscillating EDM are the only experiments that can find the axion, the pseudo-Nambu-Goldstone boson of the $U(1)_{\mathrm{PQ}}$ symmetry breaking. Furthermore, the amplitude of the oscillating EDM is proportional to the coupling constant $g_a \ll 1$. On the other hand, experiments that make use of the coupling to photons have a conversion probability that is proportional to g_a^2. The situation is even worse for the light-shining-through-wall experiments where the ALPs additionally have to be produced in the laboratory, resulting in a conversion probability proportional to g_a^4.

---

[c] There are many interaction channels for those particles, like fermions, gluons, photons, and others. Photon dominance assumes that the coupling of the new particle to photons is dominant and other channels negligible.

1.3 Cosmological and Astrophysical Constraints

Besides the experimental constraints described in Sec. 1.2, there are various constraints from cosmology and astrophysical observations. A lower bound on the mass can be set from measurements of galaxy luminosity functions at high red-shifts. The galaxy luminosity function describes the distribution of stars per luminosity interval in a galaxy. As dark matter influences the star formation and evolution, these distributions are model-dependent. Comparing data with high-resolution N-body simulations allowed to constrain $m_a \gtrsim 10^{-22}$ eV [48]. Another way to get a rough estimate of this lower bound comes from the de Broglie wavelength of the ALP field. As dark matter is located in the halo of a galaxy, the de Broglie wavelength has to be smaller than the smallest dwarf galaxies. This results in roughly the same lower bound [49].

An important constraint can be set by Big Bang nucleosynthesis (BBN) models and measurements of the ^{4}He abundance in the universe. The ALPs would change the chiral Lagrangian and in particular a term that includes the neutron-proton mass splitting. This mass difference between the neutron and the proton defines their abundance during the BBN and therefore the ratio n/p which defines the ^{4}He abundance. The measurement of the latter [31] can be compared to the ALP model and constrains $f_a m_a \gtrsim 1.8 \times 10^{-9}\ \mathrm{GeV}^2 \left(\frac{m_a}{10^{-16}\ \mathrm{eV}}\right)^{3/4}$ for $m_a < 10^{-16}$ eV. In this mass region, the oscillation of the field is slow compared to the time scale of the BBN and approximately constant. For masses $m_a > 10^{-16}$ eV, the oscillation is faster and the mass-splitting has to be averaged which leads to a constrain of $f_a m_a \gtrsim 10^9\ \mathrm{GeV}^2$ [50, 51]. An additional effect is the change of the neutron freeze-out temperature that is small compared to the above explained effect.

A third constraint originates in the measurement of the neutrino number and arrival time after the collapse of supernova SN1987A. In such a collapse, about 99% of the gravitational energy is converted into neutrinos. After the collapse of SN1987A, 25 neutrinos were measured at three detectors within a time frame of less than 13 seconds [52]. This is in good agreement with theoretical supernova models [53]. If there was another channel of energy loss, e.g., axions or ALPs, then the number of detected neutrinos and the burst duration would be different. Therefore, a rough constraint of $f_a \gtrsim 10^6$ GeV for masses lower than a few meV can be set [54].

2 Beam EDM Apparatus

We use the *Beam EDM* apparatus for our ALP search, which is described and characterized in more detail in the Ph.D. thesis of E. Chanel [55]. It applies Ramsey's method of separated oscillatory fields [56, 57]. This method has been used very successfully in atomic clocks [58, 59], to measure the Newtonian gravitational constant [60], to search for the neutron EDM [10, 46, 47], to search for new particles and interactions [61], and many more.

We use this technique applied to neutrons to search for an axion-like dark-matter signal. The neutrons act as a spin clock at their Larmor precession frequency in the magnetic field B_0, which allows to precisely detect magnetic or pseudo-magnetic field changes. In a first step, the polarized neutrons are flipped by an oscillating field B_1 into the plane orthogonal to B_0. Then, they can precess for a certain time until they are flipped again by a second oscillating B_1 field. Usually the frequency of the oscillating fields is scanned around the resonance while the phases of the two signals are locked. This results in an interference pattern with typical Ramsey fringes as shown in Fig. 2a.

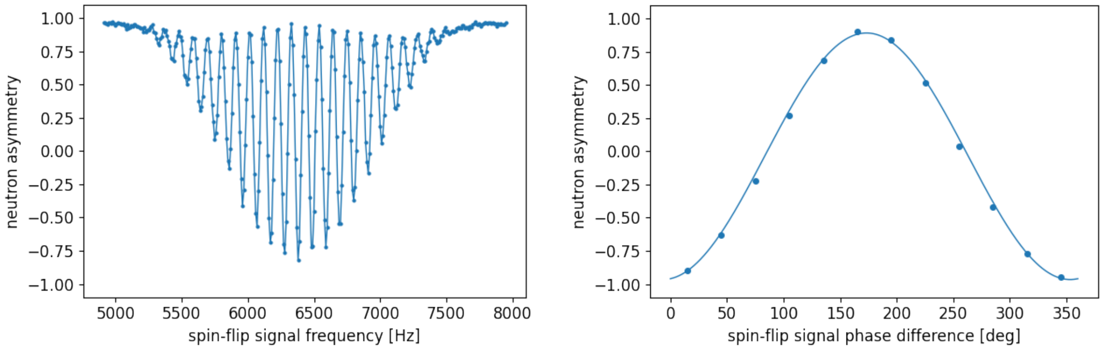

(a) (b)

Figure 2: *Ramsey-type measurements for a monochromatic beam with a wavelength of* 9 *Å at a magnetic field of* $B_0 = 220\ \mu\mathrm{T}$*. (a) Typical interference pattern of the neutron asymmetry (compare definition in Eq. (6)) as a function of the spin-flip signal frequency. The overall envelop comes from the single spin-flip resonance. The oscillations in the interference pattern are also called Ramsey fringes and the central fringe corresponds to the resonance frequency. The solid lines serve only as a guide for the eyes. (b) Signal of a Ramsey phase scan. It shows the neutron asymmetry as a function of the phase difference between the two spin-flip signals. The solid line corresponds to a least-squares fit of a sinusoidal function with a fixed period of* $360°$*.*

Another option for a Ramsey-type measurement is to keep the frequencies of both spin-flip signals fixed on resonance but scan the relative phase between the two oscillating signals. This has the advantage of always being on resonance and obtaining data in the shape of a simple sinusoidal curve that can be fitted easily as shown in Fig. 2b. In this case, the quantity of interest is the phase that a neutron spin acquires due to its coupling to a magnetic field change $\Delta B(t)$ and an electric field E

$$\varphi = \int_0^{T_{\rm int}} \left(\gamma_n \Delta B(t) + \frac{2d_n(t)}{\hbar} E \right) \, {\rm d}t \,, \tag{5}$$

where γ_n is the gyromagnetic ratio of the neutron, $d_n(t)$ its EDM including the constant and the oscillating term for the ALP search, $\hbar$ the reduced Planck constant, and $T_{\rm int}$ the interaction time which depends on the neutron velocity. Figure 3 shows a schematic of the experimental setup installed at the cold neutron beam facility PF1b at the Institut Laue-Langevin in Grenoble, France [62].

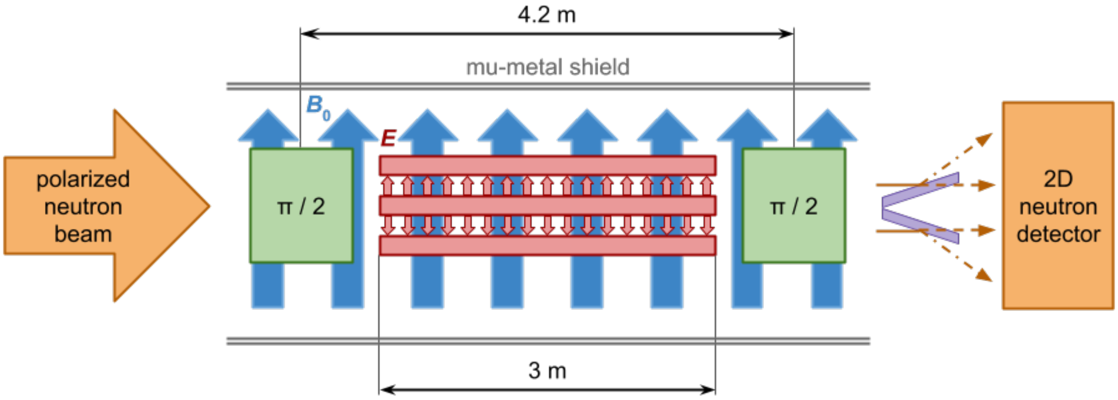

Figure 3: *Schematic of the experimental setup where a polarized neutron beam enters from the left. It shows the 6 m-long mu-metal shield around the interaction region and the two 40 cm-long radio-frequency (RF) spin-flip coils for the* $\pi/2$*-flips in green. The electrodes and the electric field direction are shown in red and the magnetic field direction is indicated in blue. The spin analyzer (purple) reflects one spin state and transmits the other. The neutrons are detected using a 2D pixel detector with a sensitive area of* $10 \times 10\ {\rm cm}^2$ *with* 16×16 *pixels. The vacuum beam pipe surrounding the electrodes is not shown.*

In the following sections we give an overview of the individual elements of the experiment. First we describe the neutron source and characteristic in Sec. 2.1. We then explain the magnetic mu-metal shielding and the magnetic field stabilization in Sec. 2.2, as well as the spin-flip coils in Sec. 2.3. We further describe the vacuum beam pipes with the high-voltage electrodes inside in Sec. 2.4. Finally, we describe the spin-analyzer and neutron detector in Sec. 2.5 and finish with the data acquisition system (DAQ) software in Sec. 2.6.

2.1 Neutron Source

We performed the search for axion-like dark matter at the cold neutron beam facility PF1b. The neutrons are provided by a nuclear fission source via the cold neutron guide H113 [62]. For all measurements, the new advanced super-mirror solid-state polarizer of the facility was installed that can achieve a polarization of 99.8% [63]. The neutron rate is about $3 \times 10^9\ \mathrm{n/cm^2/s}$ after the polarizer with a mean neutron wavelength of 4.0 Å - 4.5 Å. There is also an adiabatic fast passage spin-flipper at the facility that allows to flip the spins before the experimental area with an efficiency of more than 99.5%.

In the casemate before the experimental area we placed the neutron chopper shown in Fig. 4. The chopper allows to create a pulsed beam from the continuous fission neutron source. It is a Fermi chopper with a Soller-slit-type collimator [64]. It has a rotating casket with gadolinium sputtered silicon wafers in a vertical and parallel arrangement. If the wafers are parallel to the beam the neutrons can pass through. If the casket is rotated by a small angle, the slits become closed and the neutrons get absorbed in the gadolinium layers. The number of wafers, and therefore the slit width, defines the duty-cycle of the chopper. In the configuration we used, the duty-cycle was 2%. The pulse rate was $19\ \mathrm{Hz}$ for most measurements with a pulsed beam.

For all measurements related to the ALP search we had the chopper in the open position with the wafers parallel to the neutron beam. Nevertheless, to measure the spectrum a pulsed beam is required. With the distance from the chopper to the detector of $10.41\ \mathrm{m}$ in this measurement, and the detector in a time-of-flight mode, we measured the spectrum presented in Fig. 5.

The spectrum is in principle not necessary to know for the ALP search. It can be helpful to understand the neutron characteristics and to optimize the setup. Additionally, it was used as an input parameter for the simulations presented in Sec. 3.1.4.

2.2 Magnetic Field and Mu-Metal Shield

The magnetic field in the *Beam EDM* apparatus can be measured with eight SENSYS FGM3D/250 fluxgate sensors [65]. Four of them are placed above the vacuum beam pipe and the spin-flip coils and four below. All of them are inside the mu-metal shield. They have a range of $\pm 250\ \mu\mathrm{T}$ and measure the field in all three spatial directions. At the beamtime at PF1b in 2020 there were also five Stefan Mayer Instruments FLC3-70 fluxgates [66]

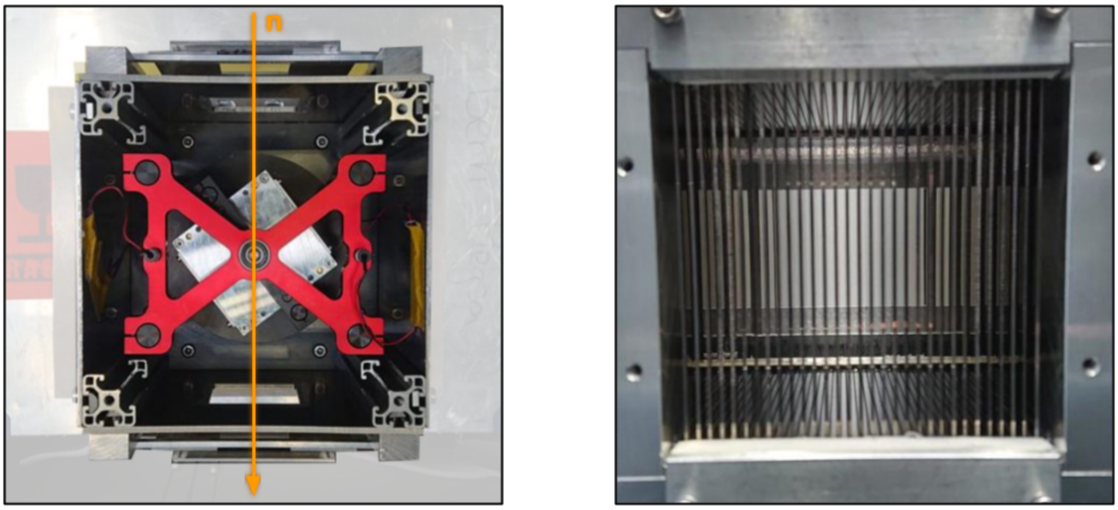

(a) (b)

Figure 4: *Images of the Fermi chopper of the Beam EDM apparatus. (a) Top view into the chopper with a size of* $26 \times 26\ \mathrm{cm}^2$ *and a height of* $35.4\ \mathrm{cm}$*. The neutron path is vertical through the center. The rotating casket with the Soller-slit-type collimator is visible as a box in the center below the red holding structure. It has an inner cross-section of* $8 \times 8\ \mathrm{cm}^2$*. The rotation frequency is measured with a laser and a photo-diode. (b) View through the casket with the Soller-slit-type collimator in the open position. The gadolinium-coated silicon wafers are visible as dark vertical lines. The number of wafers can be changed to adapt the duty-cycle. In this configuration the duty-cycle is* 2%*.*

at different positions outside of the mu-metal for monitoring the external magnetic fields. All fluxgate channels were sampled at a rate of $10\ \mathrm{kHz}$. The data were averaged over 10000 samples and stored at a rate of $1\ \mathrm{Hz}$.

The magnetic field can be controlled via a 3D-coil system shown in Fig. 6. The coils are in a rectangular-shaped Helmholtz-type arrangement that can create homogeneous fields in the region of the neutron beam. The target magnetic field can be set by applying currents through the corresponding coils in all three spatial directions plus the gradient field in the vertical direction of the main magnetic field. The main magnetic field was set to $B_0 = 220\ \mu\mathrm{T}$ and all other fields were adjusted to zero.

Additionally, there is a magnetic field stabilization in all three spatial directions and the vertical gradient field direction. The stabilization applies a PID-algorithm using the data from the four fluxgates around the vacuum beam pipe as an input value. The algorithm calculates the output value that is first converted into an analog voltage via a 20-bit analog-digital converter AD5791 [67] and then into a current via a self-made voltage-current converter.

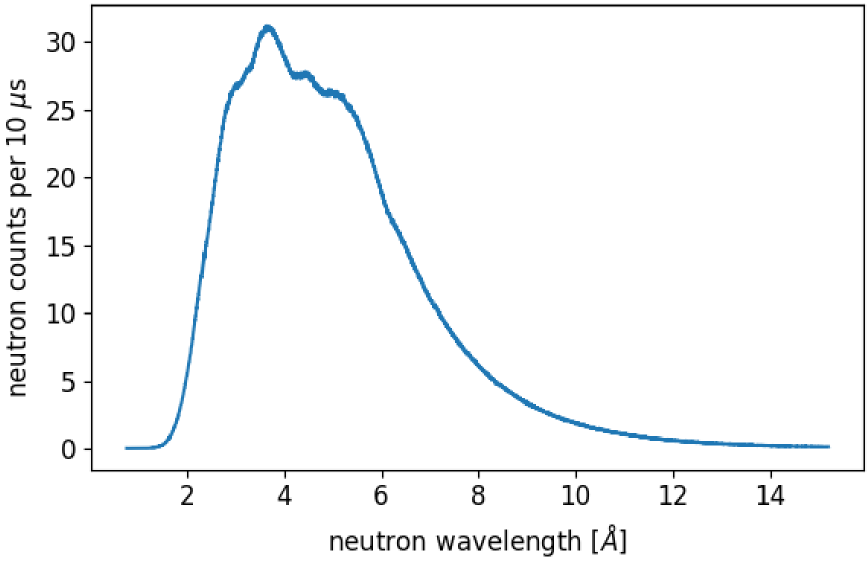

Figure 5: *Observed neutron spectrum of the detector at the PF1b beamline at the Institut Laue-Langevin (ILL) averaged over* 2000 *neutron pulses. It shows the neutron counts per time bin of* $10\ \mu\mathrm{s}$ *for a single neutron pulse as a function of the de Broglie wavelength of the neutrons. The distribution is peaking at about* 4 *Å (*$1000\ \mathrm{m/s}$*).*

This current is applied through dedicated windings via $20\ \Omega$ resistors. For the stabilization, the magnetic field data were only averaged over 1000 samples such that the field can be stabilized at a rate of $10\ \mathrm{Hz}$ to the sub-nT level.

The interaction region of the experiment is inside a $6\ \mathrm{m}$-long passive magnetic mu-metal shield. The shield is built from panels of size $1 \times 1\ \mathrm{m}^2$ with two layers of mu-metal. It is open at the two sides along the beam axis. Additionally, there are access tubes on the sides for the high-voltage feed-through and vacuum components.

The magnetic field and the mu-metal shield were thoroughly simulated and characterized in the master's theses of A. Gsponer [68] and A. Gottstein [69]. The field was determined at 47 positions over a distance of $5.3\ \mathrm{m}$ along the neutron beam path with five FLC3-70 fluxgates mounted in a cross-shaped arrangement on a magnetic field mapper. The magnetic field was recorded with a sampling rate of $10\ \mathrm{kHz}$ for two seconds at each position. A photo of the mapper in the experimental apparatus is presented in Fig. 7.

With the mapper, we measured the main magnetic field B_0 as a function of the longitudinal position in the experiment as shown in Fig. 8. Since the FLC3-70 fluxgates can only measure up to $200\ \mu\mathrm{T}$, we performed the measurement at much lower field values and normalized the data to have a mean value of $B_0 = 220\ \mu\mathrm{T}$ in the electric field region. The

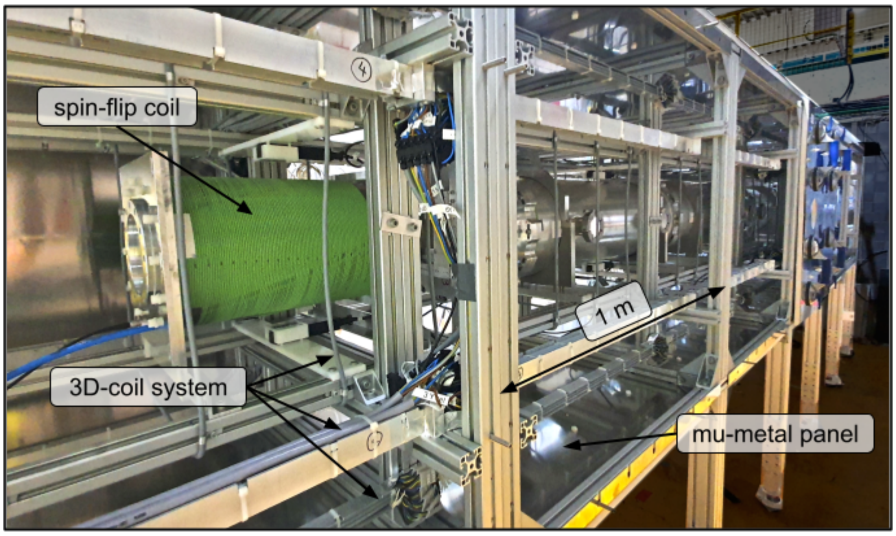

Figure 6: *Photo of the Beam EDM apparatus with the 3D-coil system to set and stabilize the magnetic field. The coils are mounted to the aluminum frame of the experiment. The mu-metal panels on top and below the experiment, as well as the one on the backside, are mounted. One of the two spin-flip coils is visible in green on the left side.*

field was averaged over all five fluxgates. It has a relative homogeneity of 4.6×10^{-4} in the interaction region.

We also measured the shielding factor by applying various external fields with and without the mu-metal shield mounted. The ratio of the two measurements gives the shielding factor presented in Fig. 9. We performed the measurement for various frequencies as a function of the longitudinal position in the experiment. The mu-metal has the highest shielding factor at $20\ \mathrm{Hz}$.

2.3 Spin-Flip Coils

The *Beam EDM* apparatus has two spin-flip coils to manipulate the neutron spins. One of them is visible in Fig. 6. The wire is wound around a polyoxymethylene (POM) tube with a length of $400\ \mathrm{mm}$ and a diameter of $250\ \mathrm{mm}$. It that can be evacuated to reduce the neutron scattering in air. The oscillating signals are generated by Keysight waveform generators [70] that are synchronized with a GPS atomic clock [71]. The signals are amplified with a $1\ \mathrm{kW}$ audio amplifier STA-1000 [72]. The magnetic field of $B_0 = 220\ \mu\mathrm{T}$ corresponds to a resonance frequency of approximately $6.4\ \mathrm{kHz}$. We applied a spin-flip signal at $6379\ \mathrm{Hz}$ in the Ramsey-phase-scan mode. The signal amplitude was optimized to flip the spins by $\pi/2$ in Ramsey-type measurements.

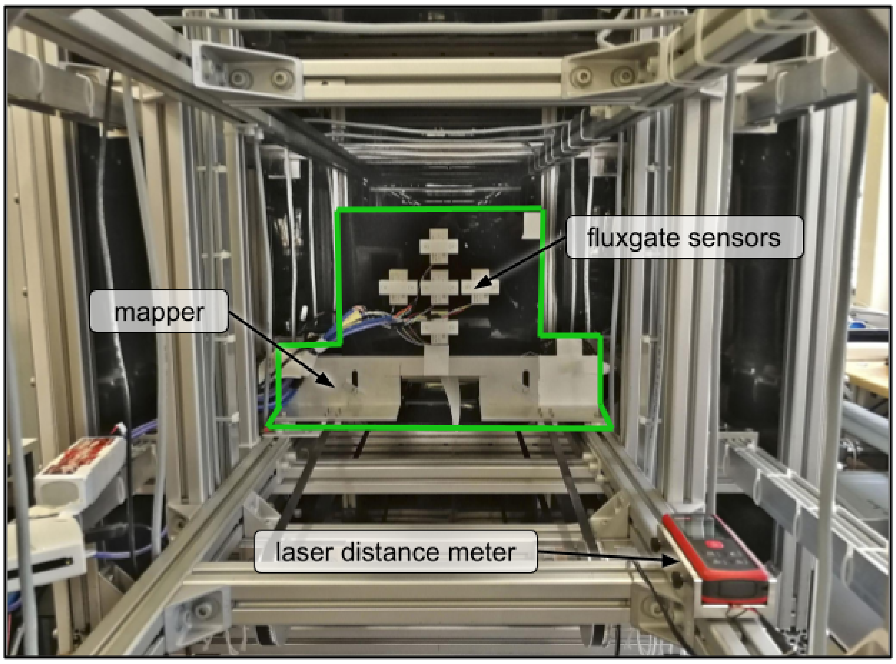

Figure 7: *Photo of the magnetic field mapper (indicated by the green line) within the Beam EDM apparatus in the laboratory in Bern. The five fluxgate sensors in a cross-shape arrangement measure the magnetic field approximately at the neutron beam cross-section. A laser distance meter measures the position of the mapper along the beam axis.*

We used the spin-flippers in two different modes. In the first mode we applied a continuous sinusoidal signal. This was mostly used when measuring with continuous neutron beam and, therefore, during all measurements related to the ALP search. The spin-flip field in sinusoidal mode can actually achieve a perfect $\pi/2$-flip only for one specific wavelength. The second mode was used when the chopper was running and the neutron beam was pulsed. Then, we also applied a sinusoidal signal but additionally modulated the signal amplitude. The modulation was triggered by the chopper and synchronized with the neutron pulse. With the proper modulation function, a $\pi/2$-flip can achieved for almost all neutron wavelengths.

The spin-flip signal frequency was chosen at $6379\ \mathrm{Hz}$ because this is a prime number. The pulse frequency of the chopper is $19\ \mathrm{Hz}$ and, therefore, a prime number as well. This way it is assured that the phase of the sinusoidal signal is not in sync with the neutron pulse. Indeed, simulations of a pre-study have shown that a randomized phase is required to perform our measurements. Otherwise, the shape of the Rabi and Ramsey measurements becomes systematically distorted.

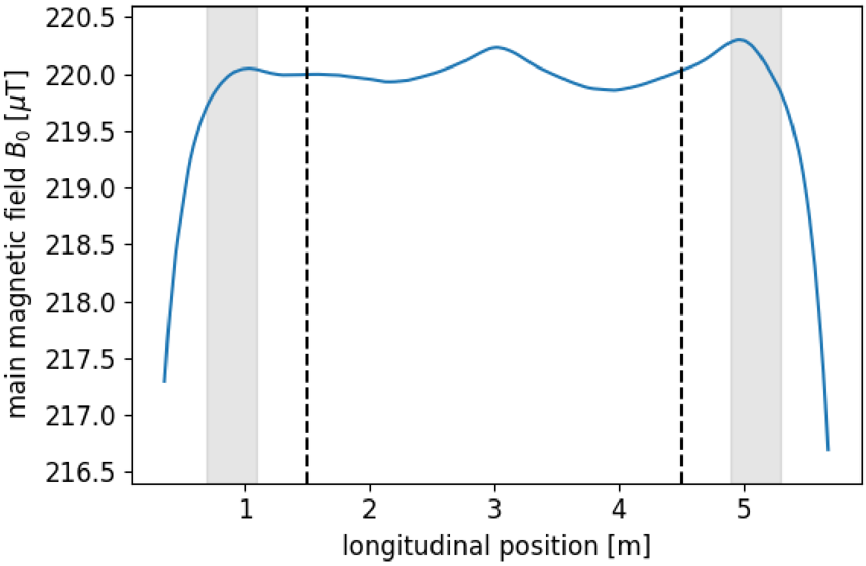

Figure 8: *Measurement of the main magnetic field B_0 in the vertical direction as a function of the longitudinal position in the experiment. The measured data (blue) is averaged over all five fluxgates. The two vertical dashed lines indicate the beginning and end of the electric field region. The vertical gray bars indicate the position of the spin-flip coils.*

2.4 Vacuum Beam Pipes and High-Voltage Electrodes

The region were the neutrons can interact with the electric field has a length of $3\ \mathrm{m}$ and is inside a vacuum beam pipe between the spin-flip coils. There are three sets of one-meter-long electrode stacks with a high-voltage electrode in the center and two ground electrodes on top and bottom. The electrode separation is $1\ \mathrm{cm}$. This setup allows for two neutron beams passing between the electrodes, simultaneously sensing the electric field direction parallel and anti-parallel to the magnetic field. This double beam arrangement provides the possibility to compensate for global field drifts and common-mode noise.

The high-voltage potential of $\pm 35\ \mathrm{kV}$ was provided by an FUG HCP [73] during all ALPs measurements.[d] This resulted in an electric field of $35\ \mathrm{kV/cm}$. A measurement of the electric field using the relativistic $\vec{v} \times \vec{E}$-effect can be found in Sec. 3.3. The potential was applied to the central electrode via a custom-made non-magnetic feed-through.

To have a good high-voltage performance and to reduce the neutron scattering in air, the

---

[d] A more powerful power supply was used for all other measurements but was not made available to us for the ALP search.

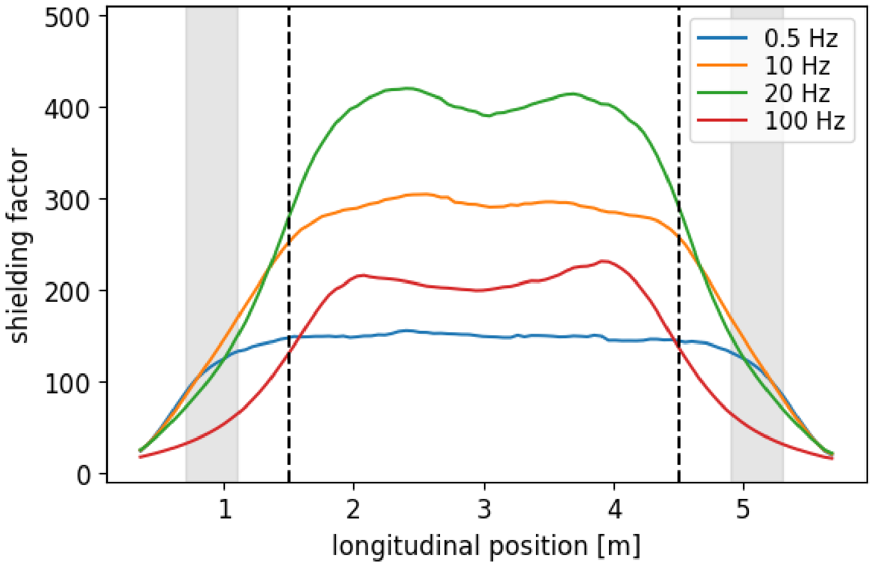

Figure 9: *Shielding factor of the mu-metal in the vertical direction as a function of the longitudinal position in the center of the experiment. The factor was measured for multiple frequencies between DC and* $1\ \mathrm{kHz}$*. Only the ones at* $0.5\ \mathrm{Hz}$ *(blue),* $10\ \mathrm{Hz}$ *(orange),* $20\ \mathrm{Hz}$ *(green), and* $100\ \mathrm{Hz}$ *(red) are shown. The two vertical dashed lines indicate the beginning and end of the electric field region. The vertical gray bars indicate the position of the spin-flip coils.*

vacuum beam pipes were evacuated to a pressure of roughly $6 \times 10^{-5}\ \mathrm{mbar}$. The pressure was monitored with multiple vacuum pressure gauges.

2.5 Spin Analyzer and Neutron Detector

For the analysis of the neutron spin we make use of Fe/Si polarizing supermirrors with an m-value of $m = 5$. These are silicon wafers with many alternating layers of iron and silicon that are placed in a magnetic field of a few mT. In such a setup, they have the property to have a spin-dependent neutron reflectivity. With a properly chosen angle of incidence, they reflect one spin state and transmit the other. Therefore, the neutrons of each spin state are spatially separated and can be counted with a 2D detector. We optimized the alignment of the analyzer mirrors for highest separation power and lowest cross-talk between the two spin states and two beams. A qualitative 2D-image of the detector that shows the four beamspots is shown in Fig. 11. The inner and outer two spots correspond to the transmitted and reflected spin states, respectively. The presented data are the sum of two measurements

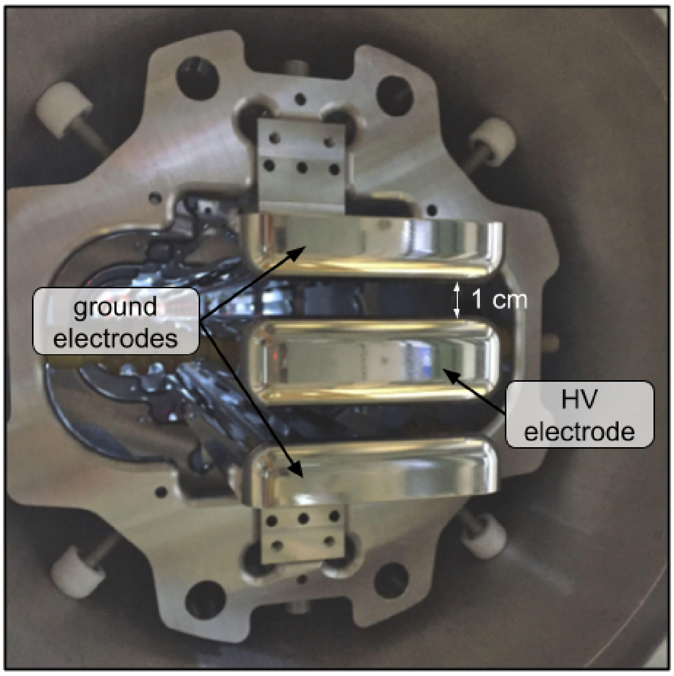

Figure 10: *Photo with the view into to vacuum beam pipe. The electrodes are held by a holding-ring structure. The high-voltage electrode is in the center and the ground electrodes are on top and bottom. The electrode separation is* $1\ \mathrm{cm}$.

with 2000 neutron pulses for each spin polarization state of the neutron beam.

For each beam the property of interest is the neutron asymmetry, defined as

$$\mathcal{A} = \frac{N_\uparrow - N_\downarrow}{N_\uparrow + N_\downarrow}\ , \tag{6}$$

where $N_\uparrow$ and $N_\downarrow$ are the neutron counts in the spin up and down state, respectively. To be most sensitive to changes in the asymmetry, the frequency and relative phase of the RF spin-flip signals are adjusted such that for each beam $\mathcal{A} \approx 0$, i.e., $N_\uparrow \approx N_\downarrow$. This corresponds to the point of steepest slope in a Ramsey resonance pattern.

We use a custom made CASCADE detector by CDT GmbH for the neutron detection [74]. The detector is based on the gas electron multiplier (GEM) technology and has a detection efficiency of roughly 35% at a neutron wavelength of 5 Å. It has a 2D-pixel array of size $10 \times 10\ \mathrm{cm}^2$ with $16 \times 16 = 256$ pixels and allows to measure with various time bin sizes in steps of $100\ \mathrm{ns}$. It has an internal memory of $32\ \mathrm{MB}$ which allows to save 2^{22} data points. This includes the spatial position of the neutron hits and the time bin. When the memory is full it has to be read out before new data can be stored. For the purpose of the ALP search

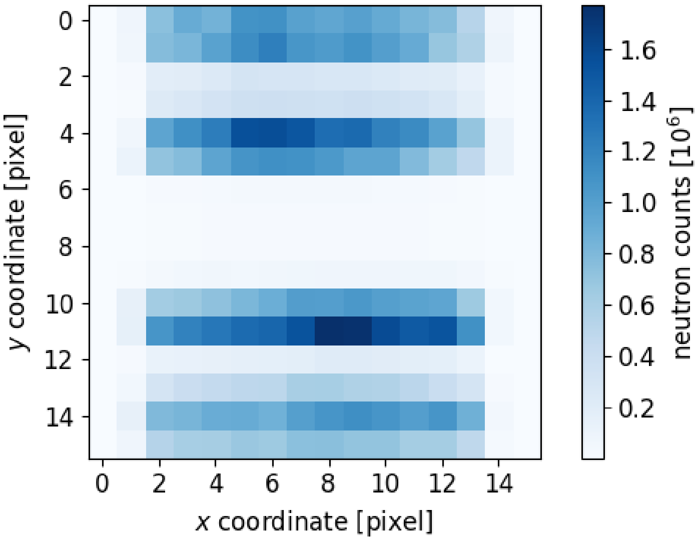

Figure 11: *Qualitative 2D image of the four beamspots. The inner two spots correspond to the transmitted spin states whereas the outer two spots correspond to the reflected spin states.*

we reduced the transversal resolution from 16 pixels to 1 pixel to be able to save more time bins and use it only as a stripe detector.

For the ALP measurement we set a time bin size of $250\ \mu\mathrm{s}$ which corresponds to a sampling rate of $4\ \mathrm{kHz}$. We used a Keysight waveform generator [70] to trigger the start and the stop of a measurement precisely. The waveform generator was synchronized with a GPS atomic clock [71]. The start pulse was triggered at a rate of $16\ \mathrm{mHz}$ that corresponds to $62.5\ \mathrm{s}$ and the stop pulse was triggered $57.5\ \mathrm{s}$ after. This allowed the DAQ to read out the detector and save the data in the $5\ \mathrm{s}$ between the stop pulse and the next start pulse.

According to the datasheet of the detector it can handle an overall neutron rate of up to $2 \times 10^7\ \mathrm{s}^{-1}$ and up to $10^7\ \mathrm{s}^{-1}$ for a single pixel. This is defined by the shortest time bin size of $100\ \mathrm{ns}$. In reality, a neutron hit creates a shower length of roughly $300\ \mathrm{ns}$ which can create signal pile-up at high neutron rates. This results in a deviation of the count error from the statistically expected Poisson error.

We investigated this behaviour in a dedicated beamtime at the BOA beamline at the PSI in July 2021. The detector was placed close to the neutron guide exit of the beamline such that the neutron beam covered the full pixel array. Paper was used to attenuate the beam to characterize the detector at different neutron rates. For each rate we counted the neutrons for various settings of the time bin size and at least 5000 time bins. We then calculated the relative difference between the theoretical Poisson error and the measured error of the total counts over all pixels with

$$\frac{\sqrt{N} - \sigma_N}{\sqrt{N}} \, , \tag{7}$$

where $\sqrt{N}$ is the mean Poisson error and σ_N the standard deviation of all time bins.

With 50 sheets of paper the neutron rate was attenuated to roughly $8.8 \times 10^6 \text{ s}^{-1}$. Figure 12 shows the theoretical Poisson and measured error of the neutron counts as a function of the time bin size. For time bin sizes below 500 ns, the data should not be considered for an analysis since this is on the same order as the neutron shower length. For time bin sizes between $1 \ \mu\text{s}$ and $20 \ \mu\text{s}$, the Poisson error is overestimating the neutron count error due to the above described signal pile-up. At even higher time bin sizes the measured neutron count error increases due to beam fluctuations. This is a characteristic of the spallation neutron source at the PSI and may be different at the fission source at the ILL.

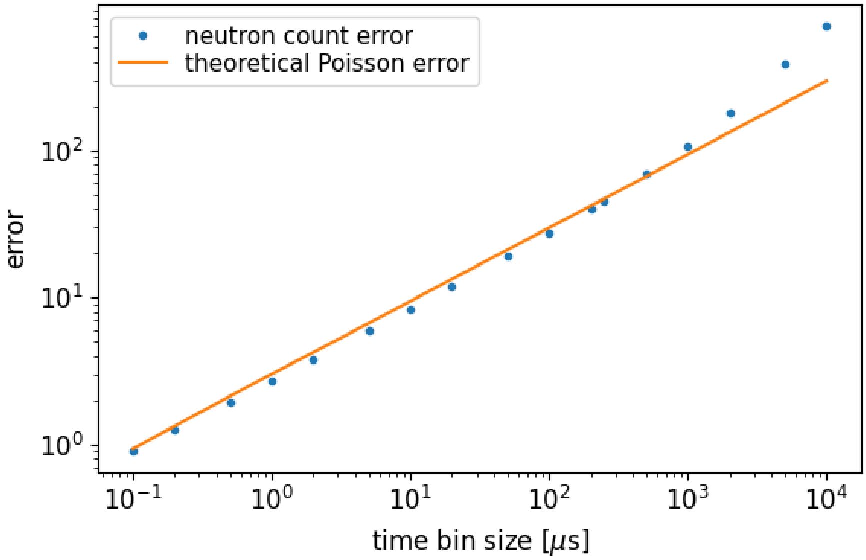

Figure 12: *Theoretical Poisson error (orange) and measured error (blue) of the neutron counts as a function of the time bin size.*

For each neutron rate we calculated the average deviation for time bin sizes between $1 \ \mu\text{s}$ and $20 \ \mu\text{s}$. In this range the relative deviation is constant and no other effects than the event pile-up are present. Figure 13 shows the relative difference between the Poisson and measured neutron count error for various neutron rates over the sensitive area of the detector. The difference follows an exponential function with a time constant of $(64 \pm 10) \text{ ns}$.

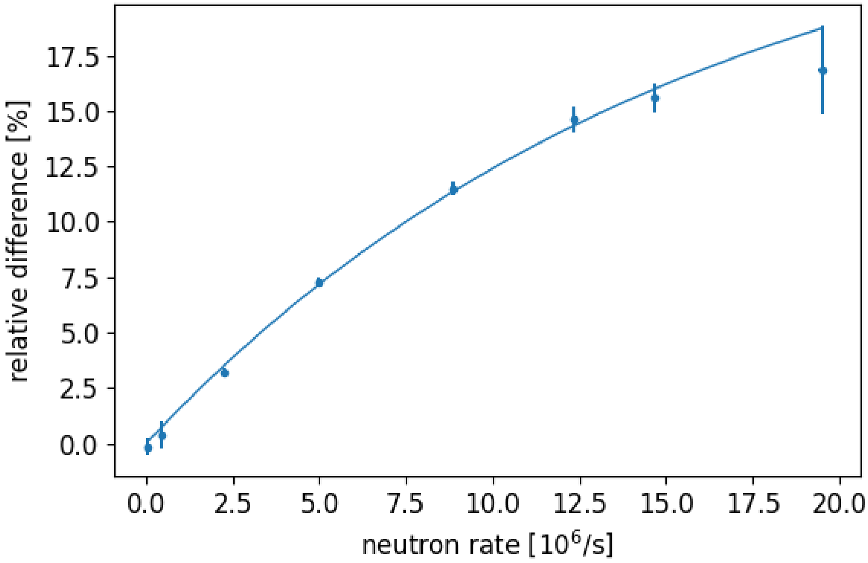

Figure 13: *Relative difference between the Poisson and measured error of the neutron counts as a function of the neutron rate. The Poisson error is overestimating the neutron count error by this percentage. The data are fitted with an exponential function that revealed a time constant of* (64 ± 10) ns.

In reality, the deviation from the Poisson error is dependent on the rate per pixel rather than the total rate. For the measurement with a neutron rate of $12.5 \times 10^6\ \mathrm{s}^{-1}$ and a time bin size of $5\ \mu\mathrm{s}$, we performed a single pixel analysis. The data are presented in Fig. 14 and show a linear behaviour in the analyzed range. The least-squares fit revealed a slope of $(3.66 \pm 0.05) \times 10^{-7}\ \mathrm{s}$. In other words, the deviation from a Poisson error is less than 1% if the rate per pixel is below $27.3 \times 10^3\ \mathrm{s}^{-1}$.

Additionally, we created a simple Monte-Carlo event pile-up simulation for comparison. The simulation creates random events at a defined rate. It then merges neutron showers of consecutive events if the hit from the second neutron is within the shower time of the neutron before. If this merged shower length exceeds a threshold, the event is labeled invalid, otherwise it is labeled valid. For the simulation we used the shower length of $300\ \mathrm{ns}$ and a threshold of $500\ \mathrm{ns}$ as it was the setting of the detector. The relative number of the invalid events of the simulation is shown in Fig. 14. It is on the same order as the relative deviation of the detector count error which is an indication that the error deviation does indeed come from event pile-up.

The deviation from the Poisson error should be characterized for each setting of the experiment. The neutron rate integrated over the entire sensitive area of the detector during

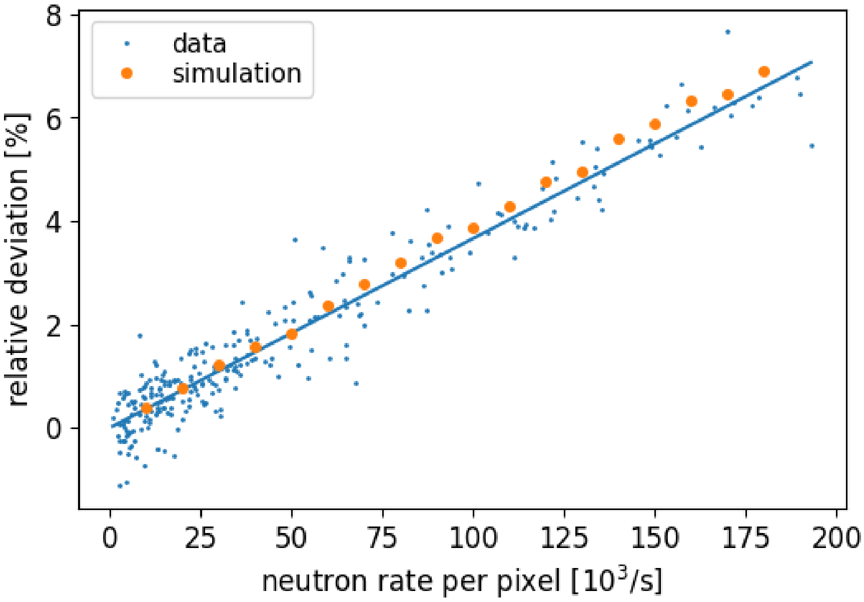

Figure 14: *Relative difference between the Poisson and measured count error for the* 256 *individual pixels as a function of the neutron rate. The data are shown in blue and a linear fit (solid line) revealed a slope of* $(3.66 \pm 0.05) \times 10^{-7}$ s. *The results of a simple event pile-up simulation is shown in orange.*

the ALP search was roughly 10^7 s^{-1} and constant over the coarse of the data taking. We characterized the relative difference of the error for each beamspot using the data of the measurement itself. An example of such an analysis is presented in the histogram of Fig. 15. For each run of in the measurement sequence we calculated the relative difference using Eq. (7) as explained before. For the full measurement sequence we calculated the mean relative deviation for each beamspot. These values are then used to correct the Poisson error of the individual measured neutron count value (for each beamspot and time bin).

2.6 MIDAS Data Acquisition System

We use the MIDAS data acquisition system for our experiment [75]. MIDAS is very flexible, can be controlled via command line or a web interface, and is accessible and controllable via SSH. The system was chosen because it has the capabilities to

- control equipment
- read-out devices
- automate sequences of measurements

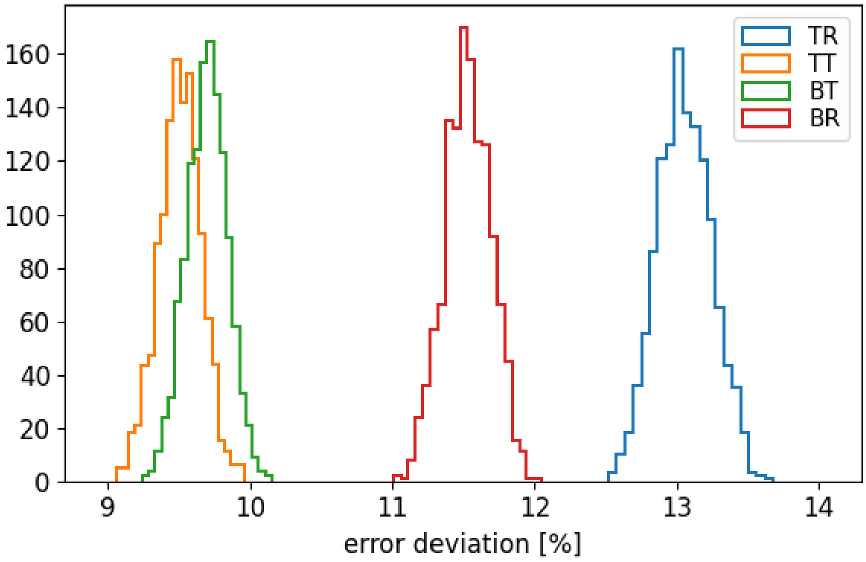

Figure 15: *Histogram of the relative deviation of the neutron count error from the Poisson error for the setup of the ALP measurement. Each entry corresponds to the mean deviation of a run of* 57.5 *seconds. The total number of runs or entries is* 1275. *The deviations for the top beam are* $(13.1 \pm 0.2)\%$ *and* $(9.5 \pm 0.1)\%$ *for the reflected (label TR, blue) and transmitted (label TT, orange) beamspot, respectively. The deviations for the bottom beam are* $(11.5 \pm 0.2)\%$ *and* $(9.7 \pm 0.1)\%$ *for the reflected (label BR, red) and transmitted (label BT, green) beamspot, respectively.*

- trigger warnings and alarms
- process data
- integrate the ROOT framework for data analysis [76]
- display data in real time

The measurements are organized in runs. Before each run, every device is initialized with the new settings from the database if they have changed. For example, the new frequency, amplitude, and phase of the spin-flip signal is sent to the waveform generator. When all devices are ready, the measurement is started. The measurement time is usually defined by the neutron detector settings. If the data acquisition of the detector is finished, it sends a signal to MIDAS that stops the measurement of all devices. The data of interest is then stored in a binary MIDAS data file. At the same time, MIDAS triggers the analyzer software that runs as a back-end program. The analyzer can pre-process the data and convert them into the ROOT format.

Most sensors like magnetic fluxgates, vacuum pressure gauges, and temperature sensors are read out continuously every second, independently on the MIDAS runs. This is the slow-control system. The measured values are displayed live in the web interface. Most sensors have a defined threshold for triggering a warning or an alarm. They can help to make the user aware that something is not working as expected.

An important part of the MIDAS system is the sequencer. It allows to automate measurement sequences instead of changing settings manually between each run. We used the sequencer for all type of measurement, e.g., when performing a Rabi frequency scan it automatically changes the frequency of the spin-flip signal. This makes the measurements less prone to user errors and allows to let an elaborate measurement running over night.

We programmed all the drivers for the individual devices, the front-ends programs to integrate the drivers into the structure of MIDAS, the analyzer software, and the scripts for the sequencer. The slow-control system was made multi-threaded to minimize the dead time between measurements.

3 Characterization Measurements

To characterize the experimental setup regarding the search for ALPs, we performed several auxiliary measurements. In Sec. 3.1, we explain the measurements where we created artificial ALP signals via oscillating magnetic fields. Since these artificial signals showed an unexpected behaviour, we performed additional measurements and simulations to investigate the origin. One of the reasons is an effect we call resonant cancellation. It was investigated in a dedicated beamtime at the Narziss beamline at the PSI and is explained in detail in Sec. 3.2. We further explain the $\vec{v} \times \vec{E}$-measurement and the analysis that we performed to deduce the electric field in Sec. 3.3.

3.1 Artificial ALP Measurement

To connect the signal amplitude of the neutron asymmetry of Eq. (6) to the ALP-gluon coupling in Eq. (4) multiple calibration measurements were conducted. In these measurements, we created artificial signals by applying homogeneous sinusoidally oscillating magnetic fields of various frequencies and amplitudes B_a in the vertical direction parallel to B_0 through the entire setup. The oscillating current was applied via a $1\ \mathrm{k\Omega}$ resistor to the magnetic field stabilization coil. We did not apply any other fields than B_a during these measurements. Note, such a field can be interpreted as a corresponding false EDM signal using Eq. (5)

$$d_n = \frac{\hbar \gamma_n B_a}{2E} \ . \tag{8}$$

3.1.1 Magnetic Field Coefficient

We conducted a calibration measurement in the laboratory in Bern where we correlated the magnetic field amplitude B_a to the applied oscillating electric current in the auxiliary coil. As in the measurement of the magnetic field B_0 and the shielding factor of the mu-metal described in Sec. 2.2, the field was determined at 47 positions over a distance of $5.3\ \mathrm{m}$ along the neutron beam path with five fluxgates mounted in a cross-shaped arrangement on a magnetic field mapper.

The magnetic field was recorded with a sampling rate of $10\ \mathrm{kHz}$ for two seconds at each position and for each axis of the five fluxgates. A sinusoidal function was fitted to the data. The results of such a scan is shown in Fig. 16. Each point corresponds to an amplitude of the sinusoidal fit. In this measurement, the applied signal was oscillating at $250\ \mathrm{mHz}$ and had an oscillating current amplitude of $2.5\ \mathrm{mA}$.

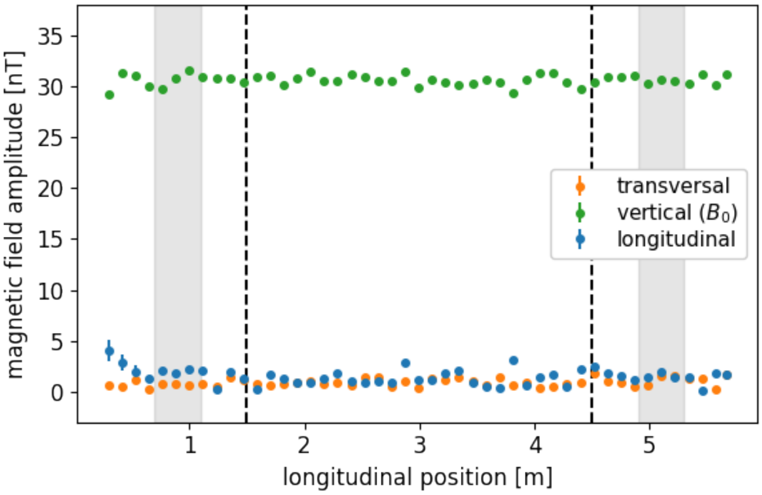

Figure 16: *Magnetic field data of the central fluxgate sensor with an artificial signal at a frequency of* $250\ \mathrm{mHz}$ *and an oscillating current amplitude of* $2.5\ \mathrm{mA}$*. The signal was applied in the vertical direction which is parallel to* B_0 *(green). The signals amplitudes of the transversal direction (orange) and longitudinal direction (blue) are also shown. Their values are slightly above zero due to a misalignment of the fluxgate. The two vertical dashed lines indicate the beginning and end of the interaction region and the vertical gray bars indicate the position of the spin-flip coils.*

We repeated this measurement for various combinations of frequency and amplitude settings of the oscillating current. The amplitude of the oscillating magnetic field was averaged over the interaction region and all five fluxgates. We did additional measurements where we applied DC currents of both polarities and same amplitudes as for the AC case. The measurements of the two polarities were subtracted to be comparable with the oscillating current measurements. The results of all those measurements is shown in Fig. 17.

For each set of amplitudes corresponding to the same frequency we performed a linear fit to get the magnetic field coefficient. Three examples at DC, $40\ \mathrm{Hz}$, and $100\ \mathrm{Hz}$ are shown in Fig. 18. This coefficients (fitted slope as shown in Fig. 18) for each frequency are shown in Fig. 19.

The magnetic field coefficient is constant for frequencies up to $5\ \mathrm{Hz}$. At higher frequencies the coefficient decreases due to the shielding of the aluminum parts from the construction frame that is visible in Fig. 7. Since this effect does not apply in the case of ALPs, we do not take these values into account and calculate the calibration parameter from the measured data up to $5\ \mathrm{Hz}$ as to $S_B = (12.13 \pm 0.02)\ \mu\mathrm{T\,A}^{-1}$.

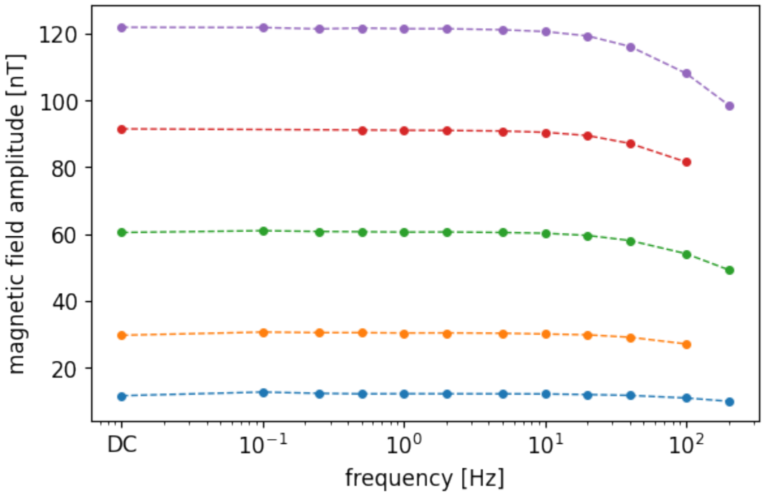

Figure 17: *Measurement of the magnetic field with artificial signals at various frequencies and amplitudes. The signal was only applied and analyzed in the vertical direction. The magnetic field amplitude for the applied oscillating current amplitudes of* $1\ \mathrm{mA}$ *(blue),* $2.5\ \mathrm{mA}$ *(orange),* $5\ \mathrm{mA}$ *(green),* $7.5\ \mathrm{mA}$ *(red), and* $10\ \mathrm{mA}$ *(purple) are shown. The dashed lines serve only as a guide for the eyes.*

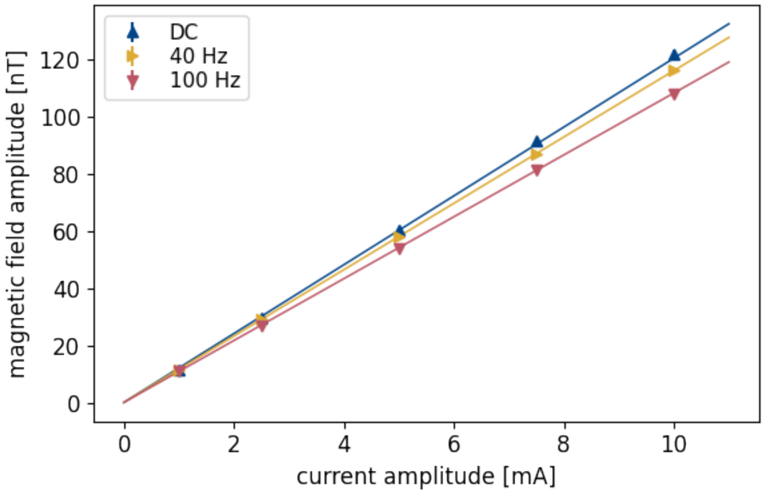

Figure 18: *Examples of the magnetic field amplitude as a function of the oscillating current amplitude for DC (blue ▲),* $40\ \mathrm{Hz}$ *(yellow, ▶), and* $100\ \mathrm{Hz}$ *(red ▼). The data are fitted with the linear functions without an offset (solid lines).*

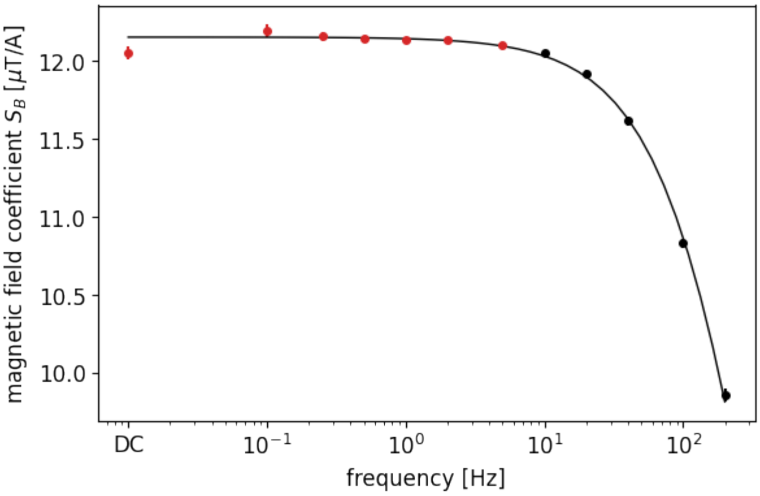

Figure 19: *Magnetic field coefficient for various frequencies between DC and* $200\ \mathrm{Hz}$*. The full data set is shown in black where the solid line corresponds to a least-squares fit of Eq. (9). The red points were taken into account to determine the calibration parameter* $S_B = (12.13 \pm 0.02)\ \mu\mathrm{T\,A^{-1}}$.

The data are fitted with a Butterworth filter [77] that is defined as a function of the frequency f:

$$\frac{A_{\mathrm{dc}}}{\sqrt{1+(f/f_c)^{2n}}}\ , \tag{9}$$

where A_{dc} is the DC amplitude, f_c the cut-off frequency (approximately the $-3\ \mathrm{dB}$ frequency), and n the filter order. The fit of the data presented in Fig. 19 revealed $A_{\mathrm{dc}} = (12.153 \pm 0.008)\ \mu\mathrm{T\,A^{-1}}$ which is in agreement with the calibration parameter S_B, $f_c = (356 \pm 11)\ \mathrm{Hz}$, and $n = (0.55 \pm 0.01)$.

3.1.2 Neutron Asymmetry Coefficient

A second calibration measurement was performed with neutrons to correlate the amplitude of the oscillating neutron asymmetry in Eq. (6) to the same coil currents applied in the first calibration measurement of Sec. 3.1.1. The main magnetic field was set to $B_0 = 220\ \mu\mathrm{T}$. All other fields were set to zero and the magnetic field stabilization was turned off. We acquired the neutron asymmetry for 60 seconds at a sampling rate of $4\ \mathrm{kHz}$ and performed again a sinusoidal fit to the data. Four examples of such signals for the upper beam are shown in Fig. 20.

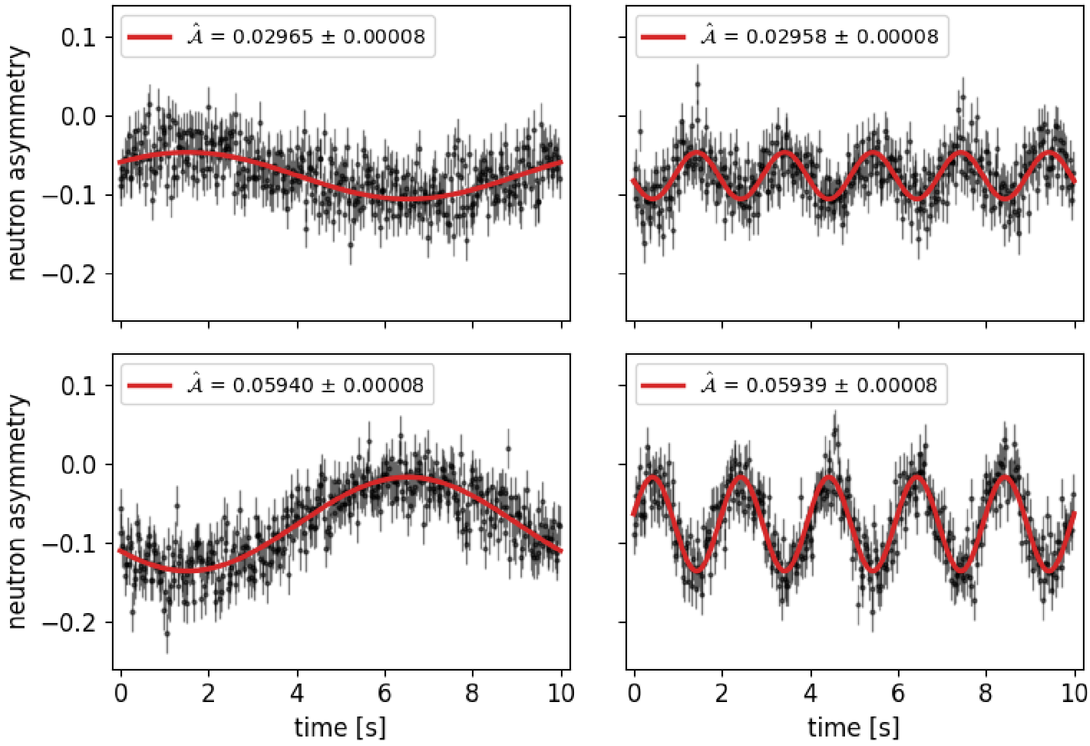

Figure 20: *Measurements of the neutron asymmetry of the upper beam for artificial signals at* $100\ \mathrm{mHz}$ *(left) and* $500\ \mathrm{mHz}$ *(right) with oscillating electric current amplitudes of* $5\ \mathrm{mA}$ *(top) and* $10\ \mathrm{mA}$ *(bottom). The sampling rate was* $4\ \mathrm{kHz}$ *but only subsets of* $10\ \mathrm{s}$ *with every 100th data point (sampling rate of* $40\ \mathrm{Hz}$*) are shown in black. The solid red lines are least-squares fits of a sinusoidal function. The fit parameter of interest is the amplitude which is given in the legend of each subplot.*

As in Sec. 3.1.1, these measurements were performed at various frequencies and amplitudes. The sinusoidal signals of the neutron asymmetry of the two beam have the same phase, whereas in the case of a real ALP signal they were phase shifted by π. As all further analysis of the ALPs is done for the difference of the two beams, we added the fitted amplitudes of the artificial signals of the two beams. This gives the same result as in the case of the difference of the two beams with a signal that is phase shifted by π. For each set of amplitudes corresponding to one frequency we again performed a linear fit to get the neutron asymmetry coefficient. Those coefficients are presented in Fig. 21.

The neutron asymmetry coefficient is also constant up to about $5\ \mathrm{Hz}$ as the magnetic field coefficient. The fit of the data with Eq. (9) revealed $A_{\mathrm{dc}} = (11.664 \pm 0.002)\ \mathrm{A}^{-1}$ which is in agreement with the mean calibration parameter $S_A = (11.5 \pm 0.5)\ \mathrm{A}^{-1}$ for frequencies

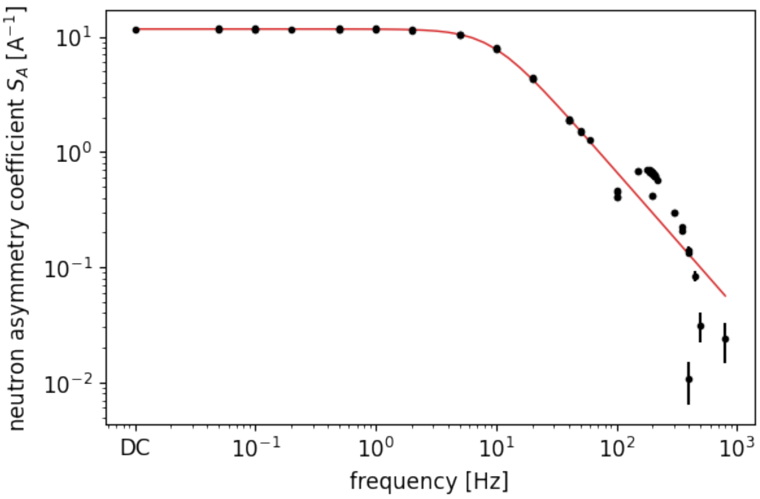

Figure 21: *Measurement of the neutron asymmetry coefficient for various frequencies between DC and* $800\ \mathrm{Hz}$*. The full data set is shown in black where the solid red line corresponds to a least-squares fit of Eq. (9). The mean calibration parameter of* $S_A = (11.5 \pm 0.5)\ \mathrm{A}^{-1}$ *was determined for frequencies below* $5\ \mathrm{Hz}$*.*

below $5\ \mathrm{Hz}$, $f_c = (9.143 \pm 0.006)\ \mathrm{Hz}$, and $n = (1.1922 \pm 0.0008)$. The primary reason for its subsequent decrease is the frequency-dependent RF shielding of the aluminum parts of the setup, i.e., the construction frame, vacuum beam pipe, and electrodes. A measurement of the aluminum shielding is presented in Sec. 3.1.3.

Another reason is an effect that depends on the neutron velocity: as shown in Eq. (5), the acquired neutron spin phase has to be integrated over the interaction time. In the case of an oscillating field, this integral becomes zero if the period of the oscillation matches the interaction time. This effect is suppressed for a beam with a broad velocity distribution but still results in a decrease in sensitivity at higher frequencies. We call this effect resonant cancellation. A simulation is presented in Sec. 3.1.4 and a dedicated measurement at the monochromatic Narziss beamline to investigate this behaviour is presented in Sec. 3.2.

Besides calculating the neutron asymmetry coefficient, the fitted amplitudes $\hat{\mathcal{A}}$ of the signals from the top beam (subscript t), the bottom beam (subscript b), and the difference of the signals of the two beams signals (subscript d), can be used to calculate a suppression factor of the two beam method using

$$\frac{\hat{\mathcal{A}}_t + \hat{\mathcal{A}}_b}{2\hat{\mathcal{A}}_d}\ . \tag{10}$$

The results for two applied current amplitudes in the frequency range between $50\ \mathrm{mHz}$ and $100\ \mathrm{Hz}$ is shown in Fig. 22. The average suppression factor in this range is 23.6 ± 0.3. This means that a signal which is present in both beams with the same amplitude and phase can be suppressed by a factor of 23.6. This applies, for example, to global drifts of the magnetic field or the eminent $50\ \mathrm{Hz}$ signal coming from the power line frequency.

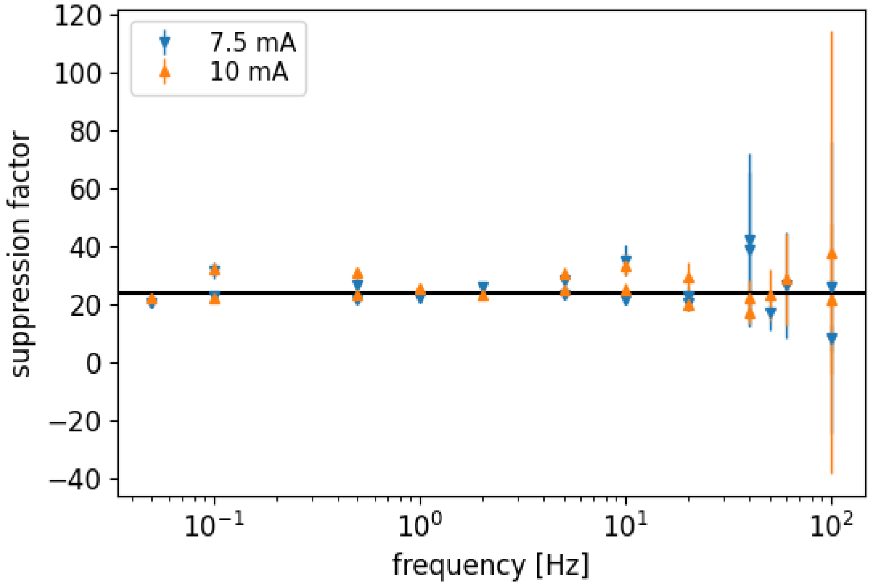

Figure 22: *Suppression factor of the two beam method as a function of the frequency in the range from* $50\ \mathrm{mHz}$ *to* $100\ \mathrm{Hz}$. *The suppression factor was calculated using Eq. (10) for the oscillating currents with amplitudes of* $7.5\ \mathrm{mA}$ *(blue) and* $10\ \mathrm{mA}$ *(orange). The average suppression factor of* 23.6 ± 0.3 *is indicated by the black line.*

3.1.3 Aluminum Shielding

To investigate the RF-shielding effect of the aluminum parts we performed a measurement in a simplified setup. The setup consisted of a FLC3-70 fluxgate sensor [66], placed in the center of the *Beam EDM* apparatus. Additionally, we placed two electrode dummies above and below the sensor, as well as a $1\ \mathrm{m}$-long section of the vacuum beam pipe centered around. A schematic of the setup is shown in Fig. 23.

We applied an oscillating current via a Helmholtz-type coil at the same position as the magnetic field stabilization coil of the other calibration measurements but with only one winding. For various frequencies we measured the magnetic field amplitude once with only the fluxgate and then with the electrodes, the vacuum pipe, or both. Taking the ratio of the

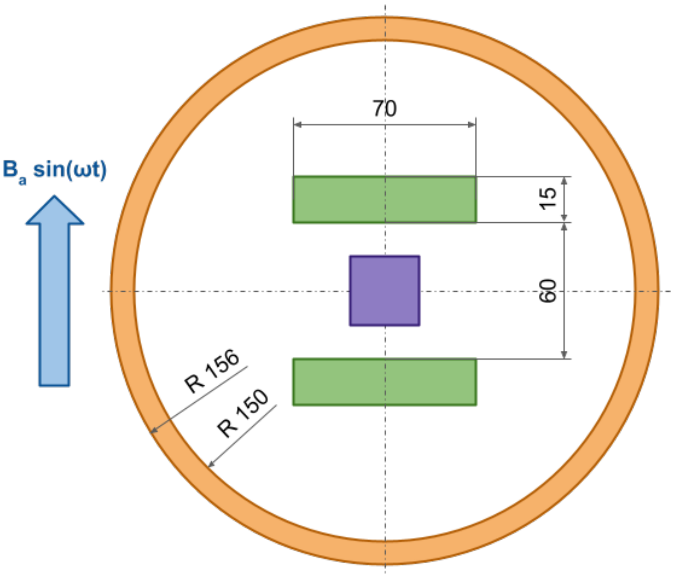

Figure 23: *Schematic of the setup that we used to measure the RF shielding of the aluminum parts. A fluxgate (purple) was placed in the center of a Helmholtz-type coil (not drawn) that was used to create the oscillating magnetic field (blue). To measure a shielding factor the vacuum beam pipe (orange), the electrode dummies (green), or both were added. All the labels are dimensions in millimeter.*

former with the rest gives the shielding presented in Fig. 24.

The data are fitted with Eq. (9) and the results are summarized in Tab. 1. The fitted parameters of the setup with the vacuum beam pipe and the one with the vacuum beam pipe + electrodes are used in the simulation of the resonant cancellation effect in Sec. 3.1.4.

	A_{dc}	f_c	n
electrodes	1.07 ± 0.03	(44 ± 7) Hz	0.54 ± 0.05
vacuum pipe	1.000 ± 0.001	(10.95 ± 0.03) Hz	1.012 ± 0.001
vacuum pipe + electrodes	0.96 ± 0.01	(11.4 ± 0.3) Hz	1.24 ± 0.02

Table 1: *Fitted parameters of Eq. (9) into the aluminum shielding data presented in Fig. 24.*

3.1.4 Resonant Cancellation Simulation

We tried to reproduce the behaviour presented in Fig. 21 with a simulation using the matrix formalism presented in [78, 79]. In this formalism, a spin vector can be manipulated by the

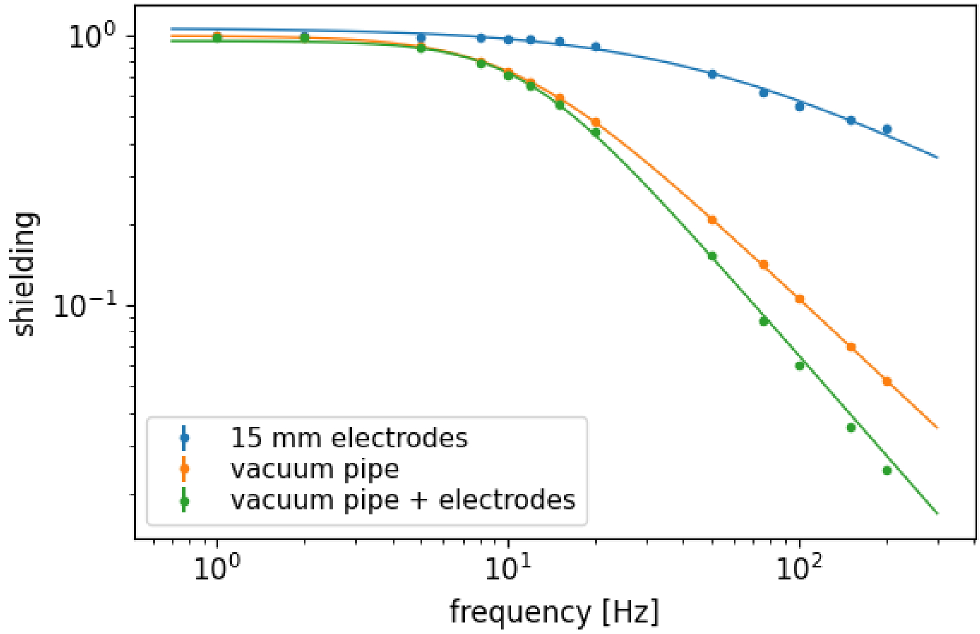

Figure 24: *Measurement of the RF shielding of* $15\ \mathrm{mm}$ *thick aluminum electrodes and the vacuum beam pipe. The shielding for various frequencies is shown for the setup with two* $15\ \mathrm{mm}$ *electrode dummies above and below the fluxgate (blue), with the fluxgate inside the vacuum beam pipe (orange), and both together (green). The data are fitted with Butterworth-filter functions (solid lines) [77].*

application of time-evolution matrices. The spin-flip probability can then be calculated by

$$\mathcal{P}_{\text{sim}} = \left| \begin{pmatrix} 0 \\ 1 \end{pmatrix} \mathcal{M}_N \cdot \mathcal{M}_{N-1} \cdot \ldots \cdot \mathcal{M}_1 \cdot \begin{pmatrix} 1 \\ 0 \end{pmatrix} \right|^2 , \tag{11}$$

where the $\mathcal{M}_i$ are the time-evolution matrices which are dependent on the position/section of the apparatus.

The simulation was divided into seven sections as schematically shown in Fig. 25. In each of the sections, various magnetic fields and aluminum shielding are present. The main magnetic field B_0 is present and constant in all sections. The artificial ALP field B_a is also present in all sections but is shielded in section III by the vacuum beam pipe (orange line in Fig. 24) and in section IV by the vacuum beam pipe + electrodes (green line in Fig. 24). At the position of the spin-flip coil in section I is the additional oscillating spin-flip field B_{rf}. The result of the simulation, together with the data from the measurement of Sec. 3.1.2 are presented in Fig. 26.

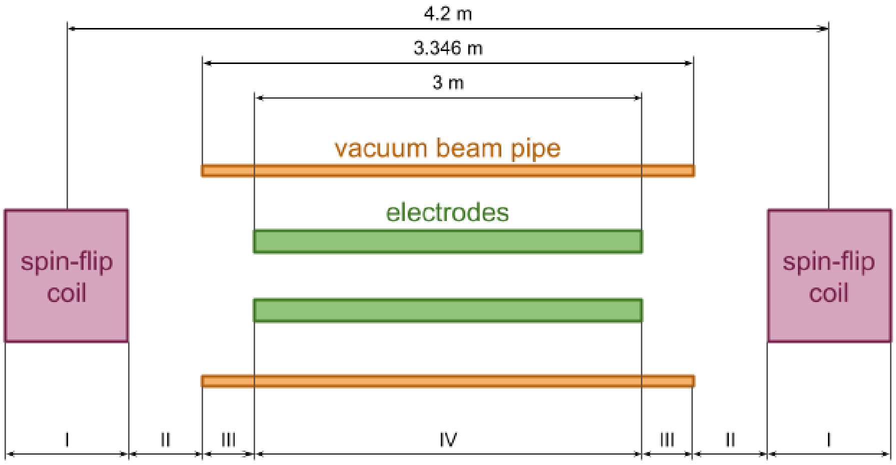

Figure 25: *Schematic of the sections that were used for the simulation of the resonant cancellation effect.*

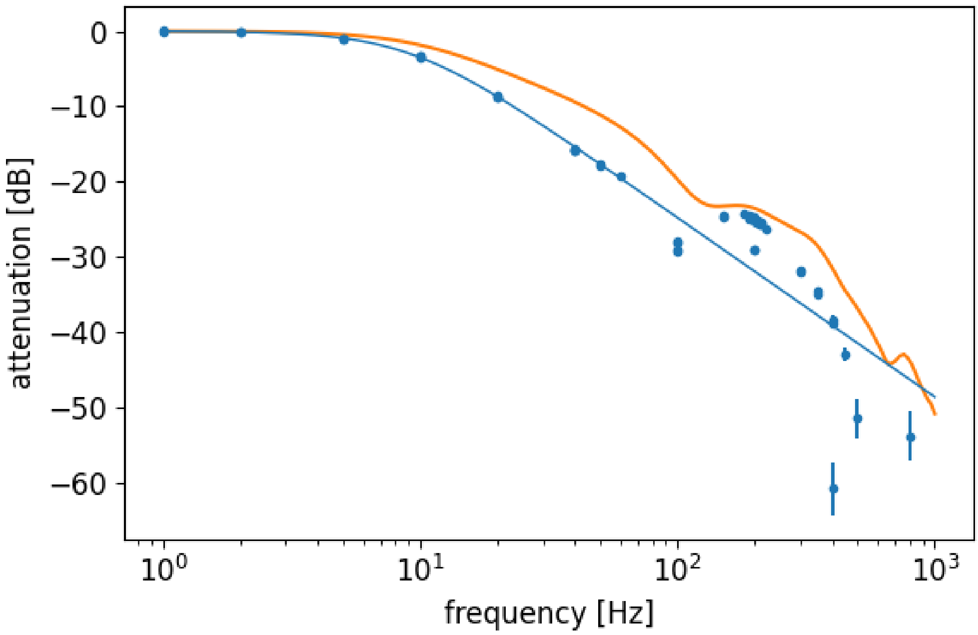

Figure 26: *Simulation of the attenuation of the neutron asymmetry amplitude due to the resonant cancellation effect and the RF shielding as a function of the frequency of the artificial signal (orange). The data from Sec. 3.1.2 with their fit are shown for comparison (blue).*

Besides dividing the setup into sections of various damping of the artificial ALP field, we also averaged over the absolute phase of the spin-flip signals and the neutron spectrum of

Fig. 5. The latter was weighted by the neutron counts for each wavelength.

The simulation is reproducing the general behaviour of the attenuation due to the aluminum shielding and the resonant cancellation effect. For low frequencies below roughly $5\ \mathrm{Hz}$ it is constant. For higher frequencies, the attenuation becomes stronger and even shows a bumpy shape. Nevertheless, the attenuation of the simulation cannot fully reproduce the behaviour of the data. The reason is most certainly that the simulation is not detailed enough. The aluminum shielding was only measured in the center between two dummy electrodes and with no central electrode. On the other hand, the neutron beam has a width that is only slightly narrower than the electrode width. At the edges of the electrodes, the aluminum shielding is less and thus also the attenuation of the artificial signal. Additionally, there are various other aluminum pieces like the frame of the setup or vacuum and high-voltage feed-throughs. The effect of the mu-metal shield around the artificial ALP coil was also not taken into account.

3.1.5 Calibration

Together, the two calibration measurements of Sec. 3.1.1 and Sec. 3.1.2 are used to translate the amplitude of an oscillating neutron asymmetry into a corresponding (pseudo-)magnetic field amplitude via

$$B_a = \frac{4.2}{3}\frac{S_B}{S_A}\mathcal{A}\ . \tag{12}$$

The factor of $4.2/3$ comes from the fact that the magnetic and the electric interaction length are different as shown in Fig. 3. The resulting calibration curve as a function of frequency is presented in Fig. 27.

The simulation described in Sec. 3.1.4 could not reproduce the behaviour of the data presented in Fig. 21 but suggest that the actual decrease in sensitivity would be smaller for real ALP signals. However, since these effects cannot be simply decorrelated, we use the curve shown as the red line in Fig. 27. This results in a conservative upper limit at high frequencies if no ALP-signal was found.

3.2 Resonant Cancellation Measurement at Narziss

The measurement of the neutron asymmetry coefficient S_A described in Sec. 3.1.2 shows a decrease at frequencies above $5\ \mathrm{Hz}$. This was expected from the frequency-dependent RF shielding of the aluminum parts of the setup. At a frequency of roughly $200\ \mathrm{Hz}$ there is an additional bump that was not expected. A thorough investigation with calculations and simulations revealed the effect we call resonant cancellation. For a monochromatic beam

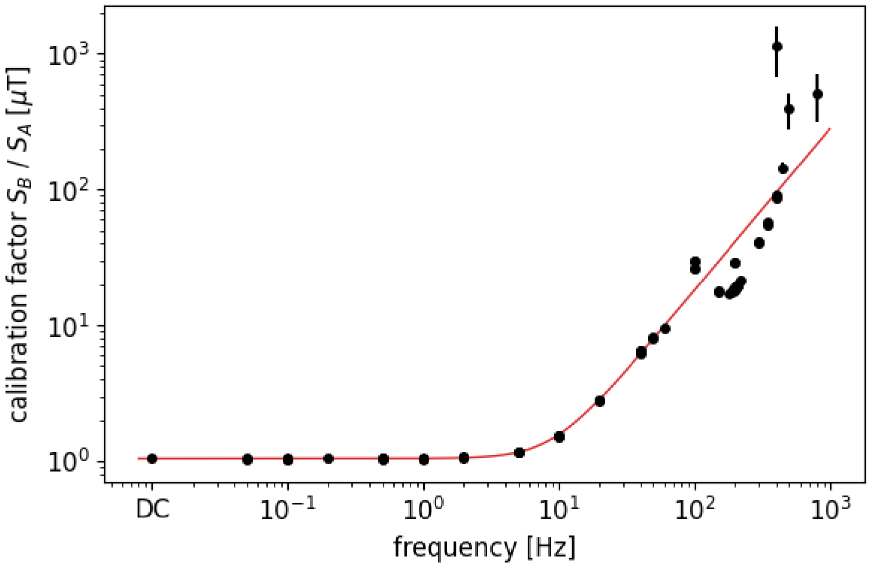

Figure 27: *Calibration factor S_B/S_A as a function of frequency. The measured data is shown as dots, whereas the red line corresponds ratio of the fitted functions of S_B and S_A which is used for the data analysis. For instance, typical neutron asymmetry signals of the order 10^{-5} correspond to a pseudo-magnetic field of $14\ \mathrm{pT}$ for frequencies smaller than $5\ \mathrm{Hz}$ using Eq. (12).*

with only one wavelength it can be simply explained.

The additional phase that the neutron spins acquire when interacting with an oscillating magnetic field $B_a(t)$ parallel to the main magnetic field B_0 is

$$\Delta\varphi = \gamma_n \int B_a \cos\left(2\pi\nu_a t\right) \mathrm{d}t \ , \tag{13}$$

where ν_a is the frequency of the oscillating field. This becomes maximal when the integral is evaluated symmetrically around zero which leads to a maximum value of the phase

$$\Delta\varphi_{\text{max}} = \gamma_n B_a \int_{-L/(2v)}^{L/(2v)} \cos\left(2\pi\nu_a t\right) \mathrm{d}t = \frac{\gamma_n B_a}{\pi\nu_a} \sin\left(\pi\nu_a \frac{L}{v}\right) \ , \tag{14}$$

where L is the interaction length and v is the neutron velocity. Eq. (14) has the form of a sinc-function with roots at $\nu_a = v/L$. The interpretation is, that when the interaction time of a neutron with the oscillating field is exactly the period of an oscillation, the integral becomes zero and so does the additional phase or the effect of an oscillating ALP field.

To test this effect we conducted at a dedicated beamtime at the Narziss beamline at the PSI. This measurement was performed together with the master's student I. Calic [80]. The Narziss beamline is usually used for neutron reflectivity measurements. It provides neutrons with a de Broglie wavelength of 4.94 Å and a spread of 1.5% full width at half maximum (FWHM). It can therefore be regarded as monochromatic for the purpose of our measurement. A photo of the beam line with our experimental setup is presented in Fig. 28.

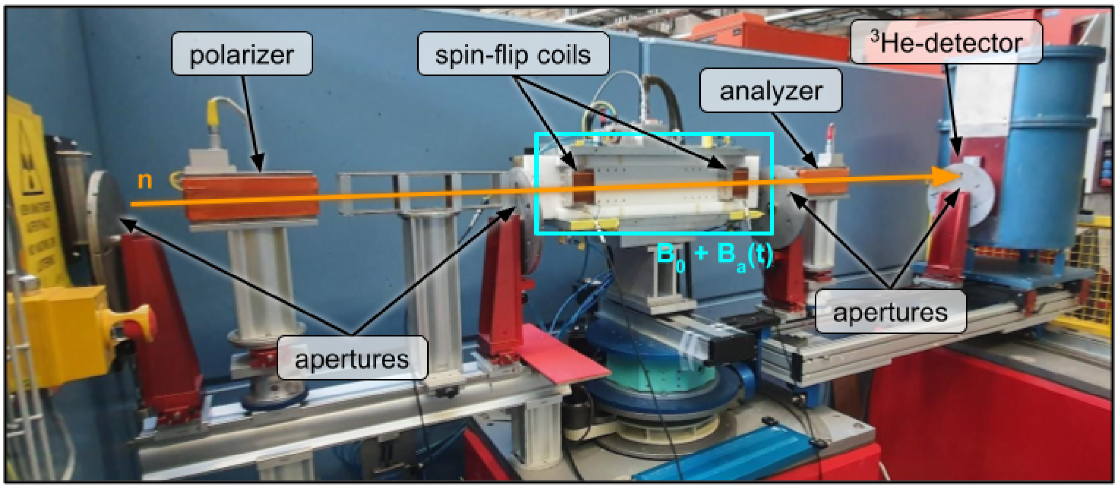

Figure 28: *Photo of the experimental setup used to measure the resonant cancellation effect at the Narziss beamline at the PSI. Neutrons enter the setup from the left (orange arrow). They first pass the polarizer that transmits only one spin state. The neutrons then enter the magnetic interaction zone where a constant magnetic field* B_0 *and an oscillating magnetic field* $B_a(t)$ *can be applied in the vertical direction. Two* 4 cm*-long spin-flip coils with a center-to-center separation of* 50 cm *allow to flip the spins. After the second spin-flip coil is the analyzer that again transmits only one spin state. The neutrons are counted with a* ^{3}*He detector. Additionally, there are four apertures on the red pillars to define the beam size.*

The neutrons from the beam exit in the wall are polarized with a Fe/Si-polarizing supermirror that transmits only one spin state. The other spin state is stopped in apertures. To maintain polarization there is a magnetic guiding field between the polarizer and the first spin-flip coil. The interaction zone, where the neutrons interact with the magnetic fields, is in the center of the experiment. The main magnetic field $B_0 \approx 3\ \mathrm{mT}$ in the vertical direction is created by an electro-magnet surrounding the back of a c-shaped iron yoke. The yoke guides the field lines and creates a homogeneous field between its flanks. The magnetic field $B_a(t)$ is created by a Keysight waveform generator [70] that is connected to an additional coil between the yoke and the white holding plate of the spin-flip coils via a Kepco bipolar power amplifier [81]. The two rectangular solenoid-type spin-flip coils have a length of 4 cm and a center-to-center separation of 50 cm. Their axis is aligned with the neutron beam and their cross-section is much bigger than the size of the beam. The spins are analyzed with another Fe/Si-polarizing supermirror as in the polarizer that let only one spin state pass. The transmitted neutrons are then counted using a ^{3}He detector. Each neutron hit in the detector creates an electronic pulse that is processed by a custom-made DAQ using an Arduino. It saves the neutron counts as a function of the time by increments the number of counts in the corresponding time bin that was defined before the measurement. There are four apertures with an opening of $30 \times 2 \text{ mm}^2$ that define the beam cross-section and divergence. The first is at the beam exit in the wall, the second before the first spin-flip coil, the third after the second spin-flip coil, and the fourth just before the detector.

The spin-flip signals were optimized for a Ramsey measurement. We measured a resonance frequency of $(91.86 \pm 0.04) \text{ kHz}$ and $(91.42 \pm 0.05) \text{ kHz}$ for the first and the second spin-flip coil, respectively. For further measurements we applied a signal at a frequency of 91.7 kHz. The amplitudes of both spin-flip signals were optimized for the highest signal visibility in a Ramsey measurement, corresponding to a $\pi/2$-flip.

To test the functionality of the setup we performed various frequency and phase scans. Two such measurements are presented in Fig. 29 for illustration. The measurement time for each data point was roughly 10 seconds.

The Ramsey frequency scan shows the behaviour as expected where the overall envelope comes from the single spin-flip resonance and the fringes are the interference pattern of the two spin-flip coils [56, 57]. Figure 29a shows nicely that the neutron beam is monochromatic. Compared to the Ramsey frequency scan shown in Fig. 66 where there is a quadratic velocity distribution, all fringes in Fig. 29a reach almost the maximum possible neutron counts of about 28×10^3. This is only the case if there are not multiple neutron velocities that mix on the way to the detector. The Ramsey phase scan in Fig. 29b shows a sinusoidal behaviour whose phase is shifted if an additional offset current is applied. A linear least-squares fit through all phases revealed $(-257.1 \pm 0.5)\ ^\circ/\text{A}$ which corresponds to roughly $40\ \mu\text{T}/\text{A}$. The measurements presented in Fig. 29 show that the apparatus works as expected and that an offset current through the additional coil indeed changes the precession frequency of the neutrons.

To measure the resonant cancellation effect we were interested in the amplitude of the oscillating neutron signal. Therefore, we had to measure the neutron counts continuously. Because of limitations from the DAQ, we phased/mapped the data into two periods. This mapping was triggered by the waveform generator that created the signal for the oscillating magnetic field $B_a(t)$. We chose the time bin size of $20\ \mu\text{s}$ such that for the highest frequency of 3500 Hz there are still at least ten time bins per oscillation. The relative phase between

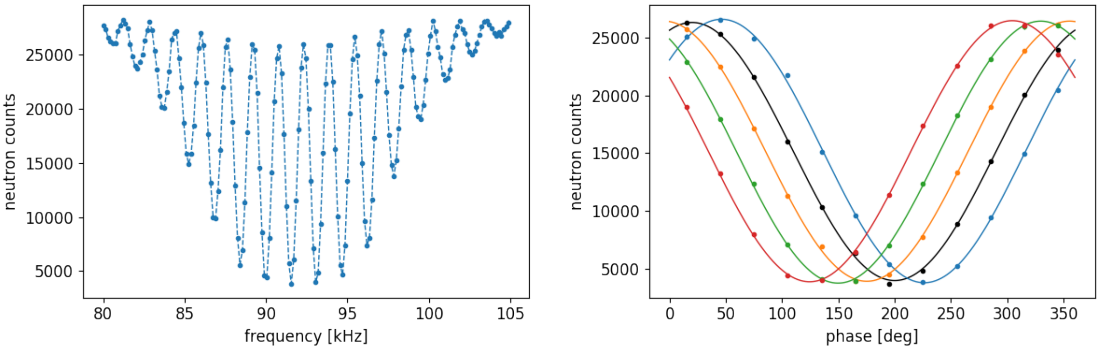

(a) (b)

Figure 29: *Measurements for testing the functionality of the setup. (a) Ramsey frequency scan over the full resonance. The data show the neutron counts as a function of the spin-flip signal frequency. The dashed lines serve only as a guide for the eyes. (b) Ramsey phase scan were the neutron counts are shown as a function of the relative phase between the two spin-flip signals. The frequency was fixed on resonance at* $91.7\ \mathrm{kHz}$. *Besides the* B_0 *field that serves as a reference (black), we applied an additional constant offset current via the ALP coil of* $-100\ \mathrm{mA}$ *(blue),* $+100\ \mathrm{mA}$ *(orange),* $+200\ \mathrm{mA}$ *(green), and* $+300\ \mathrm{mA}$ *(red). The solid lines correspond to least-squares fits of a sinusoidal function.*

the spin-flip signals was set to $105°$ which corresponds to the point of steepest slope in the reference measurement of the Ramsey phase scan shown in Fig. 29b. At this point, the measurement is most sensitive to magnetic field changes. Two examples of neutron signals are shown in Fig. 30 and the results of their sinusoidal fits are presented in Tab. 2.

	$90\ \mathrm{Hz}$	$252\ \mathrm{Hz}$
amplitude	13.9 ± 0.5	37 ± 1
offset	132.1 ± 0.3	368 ± 1
amplitude / offset	0.106 ± 0.004	0.100 ± 0.004

Table 2: *Results of the sinusoidal fit of the data presented in Fig. 30a* $(90\ \mathrm{Hz})$ *and Fig. 30b* $(252\ \mathrm{Hz})$. *The ratio of the amplitude and the offset is the property of the different measurements that has to be compared. The phase of the signal is not relevant for the analysis of the resonant cancellation effect.*

We measured the oscillating neutron amplitude three times for 100 frequencies between $60\ \mathrm{Hz}$ and $3500\ \mathrm{Hz}$ and averaged over the three iterations. The measurement time for each data point was roughly 100 seconds. Since the data acquisition was done with the same time bin size and the same total number of neutrons (measured with an additional monitor

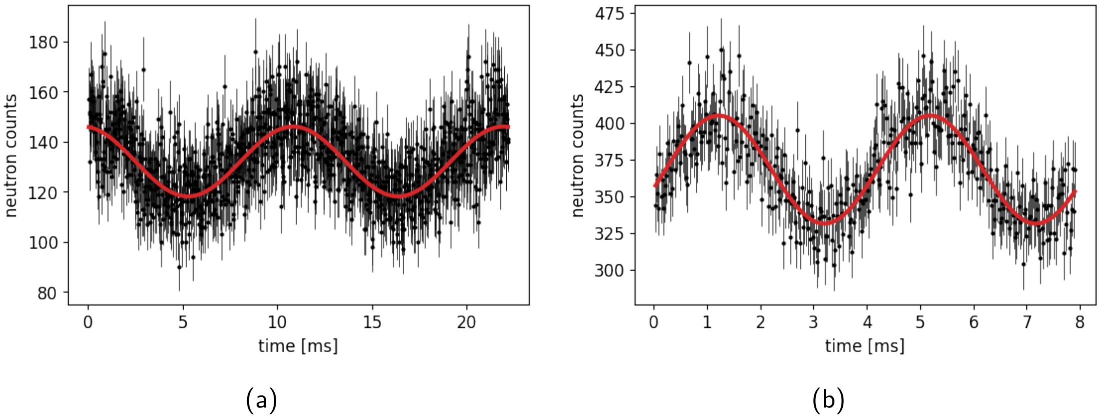

Figure 30: *Neutron signal for an oscillating magnetic field at* $90\ \mathrm{Hz}$ *(a) and* $252\ \mathrm{Hz}$ *(b). It shows the neutron counts as a function of the time. The counts are phased/mapped into two periods of the signal. The data (black) are fitted with a sinusoidal function with a fixed frequency (red). The fit results are presented in Tab. 2. The measurement time was roughly* 100 *seconds for each setting.*

counter), the number of bins was different for all measured frequencies. The amplitude and offset of the sinusoidal neutron signal scales with the number of time bins. Therefore, it had to take the ratio between the amplitude and the offset to make the measurements comparable. The result of these frequency scans is shown in Fig. 31. We compensated the frequency dependence of the magnetic field amplitude and normalized the amplitude to one at DC. The fit of Eq. (14) provided the values of the roots at $(1529 \pm 7)\ \mathrm{Hz}$ and $(3057 \pm 14)\ \mathrm{Hz}$.

Figure 31 shows that the effect of the resonant cancellation behaves as expected for a monochromatic neutron beam. Assuming a neutron wavelength (velocity) of 4.94 Å ($800\ \mathrm{m/s}$), the fit values of the root leads to an interaction length of $52.4 \pm 0.2\ \mathrm{cm}$ which is close to the effective interaction length of $51.1\ \mathrm{cm}$ [78].[e] The measurement confirmed the expected behaviour of the resonant cancellation effect. In this simple setup with a monochromatic neutron beam and no shielding of any aluminum parts, the neutron oscillation amplitude follows Eq. (14). Even though we were not able to fully decorrelate this effect from the aluminum shielding in the ALP measurement with the *Beam EDM* apparatus, it helped in our understanding of the calibration presented in Sec. 3.1.5.

---

[e] The effective interaction length is slightly longer than the center-to-center separation of the spin-flip coils. The reason is, that the spins start already to precess within the spin-flip coil when partially flipped.

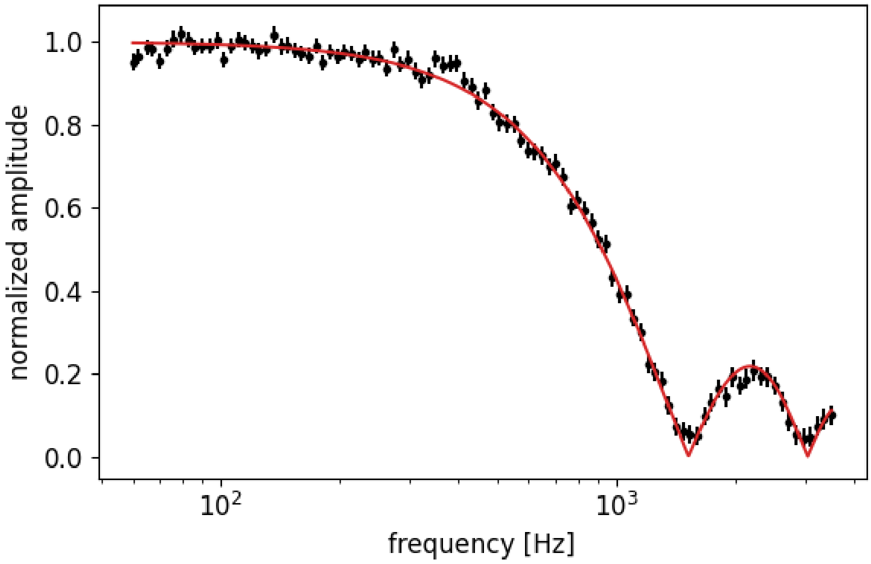

Figure 31: *Measurement of the resonant cancellation effect at the Narziss beamline at the PSI. The normalized amplitude as a function of the frequency of the oscillating signal is shown. The data (black) are fitted with Eq. (14) (red).*

3.3 $\vec{v} \times \vec{E}$ Measurement

Measuring an electric field is in general difficult. Most experiments that apply a high-voltage potential rely on the power supply to provide the stated set voltage and calculate the field from the geometry of the electrodes.

We make use of the relativistic $\vec{v} \times \vec{E}$-effect to measure the electric field in our setup. A particle with velocity $\vec{v}$ in an electric field $\vec{E}$ sees a pseudo-magnetic field according to

$$\vec{B}_{v \times E} \approx -\frac{\vec{v} \times \vec{E}}{c^2} \ .^{\text{f}} \tag{15}$$

In a Ramsey-type setup, this is another contribution to the neutron spin phase according to Eq. (5). Therefore, the phase shift that the neutrons acquire is a direct measure of the high-voltage potential

$$\Delta U = \Delta\varphi \frac{c^2 d}{\gamma_n L \sin(\alpha)} \ , \tag{16}$$

---

[f] In principle there is an additional Lorentz factor $\gamma = 1/\sqrt{1 - v^2/c^2}$ that was omitted to not confuse with the γ-symbol of the gyromagnetic ratio. Since the mean neutron velocity is roughly $1000\ \mathrm{m/s}$, the Lorentz factor is about one.

where d is the electrode separation, L the interaction length with the electric field, and α the angle between the electric and magnetic field direction.

In the configuration that we usually measure, the electric and magnetic fields are parallel with respect to each other and orthogonal to the velocity vector of the neutrons. Since the electric field direction is fixed by the geometry and orientation of the electrodes in the vacuum beam pipe we changed the magnetic field direction. This was done by adding a horizontal magnetic field component B_h using the 3D-coil system of the *Beam EDM* apparatus. The resulting magnetic field amplitude becomes $B_0 = \sqrt{B_h^2 + B_v^2}$ and the tilting angle $\alpha = \arctan(B_h/B_v)$. For this measurement we reduced the vertical magnetic field to $B_v = (214 \pm 1)\ \mu\mathrm{T}$ and added a horizontal field of $B_h = \pm(53 \pm 2)\ \mu\mathrm{T}$.[g] This gives $B_0 \approx 220\ \mu\mathrm{T}$ as for the standard measurements but tilted by $\alpha = \pm(13.9 \pm 0.5)°$.

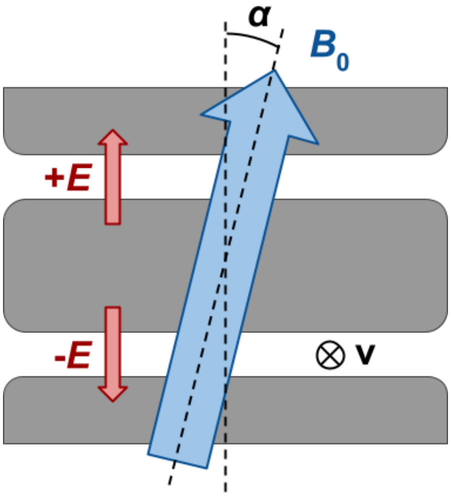

Figure 32: *Schematic of the electric and magnetic field arrangement in the $\vec{v} \times \vec{E}$ measurement. The electric field direction (red arrows) is defined by the geometry and orientation of the electrodes (gray). The magnetic field direction (blue arrow) can be tilted by angle α using the 3D-coil system of the Beam EDM apparatus.*

The electrode separation d is slightly different for both beams. The reason for this deviation is the vertical displacement of the central high-voltage electrode due to gravity. After the beamtime we measured a separation of $(10.4 \pm 0.2)\ \mathrm{mm}$ and $(9.6 \pm 0.2)\ \mathrm{mm}$ for the top and the bottom beam, respectively.

---

[g] The actual set and measured field in this measurement was $B_h = \pm 50\ \mu\mathrm{T}$. The reason for this difference lies in the fact that the fluxgate sensors measure the field outside of the vacuum beam pipe and not the location of the neutron beams.

To measure the electric field we performed a sequence of Ramsey phase scans where we changed the high-voltage like: $0\ \mathrm{kV}$ / $+35\ \mathrm{kV}$ / $0\ \mathrm{kV}$ / $-35\ \mathrm{kV}$ / .... The measured neutron phase of this sequence for the top beam and $B_h = -53\ \mu\mathrm{T}$ is shown in Fig. 33. The $0\ \mathrm{kV}$ measurements serve as a reference and can be used to correct for drifts of the neutron phase over time. We did this by fitting a cubic polynomial through them and shifting the phase of the $\pm 35\ \mathrm{kV}$ measurements accordingly.

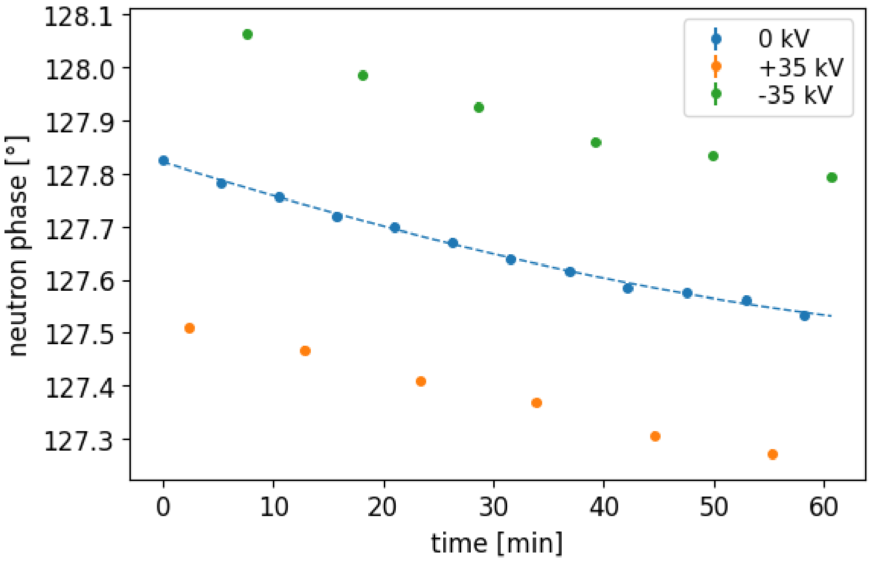

Figure 33: *Measurement of the neutron phase for the top beam and* $B_h = -53\ \mu\mathrm{T}$*. The applied high-voltage potentials were* $0\ \mathrm{kV}$ *(blue),* $+35\ \mathrm{kV}$ *(orange), and* $-35\ \mathrm{kV}$ *(green). The blue dashed line is a least-squares fit of a cubic polynomial through the* $0\ \mathrm{kV}$ *measurements that serves as a drift correction.*

Besides the angle α that is defined by the amplitudes of the vertical and horizontal magnetic field amplitudes, there can be a misalignment β between the electric field direction and the vertical magnetic field direction. To find β, we compared the measurements of the two directions of B_h. If there was no misalignment, the value of ΔU from Eq. (16) is the same for both directions. This was not the case and we optimized β such that the value of ΔU becomes the same as shown in Fig. 34. This led to a misalignment angle of $\beta = 0.87° \pm 0.09°$.

In total we have four measurements of the electric field. They were measured in two sequences, one for each direction of B_h. For each sequence the electric field can be deduced for the top and the bottom beam separately. For each consecutive pair of the high-voltage potential as shown in Fig. 33 we calculated the phase difference. With the weighted mean

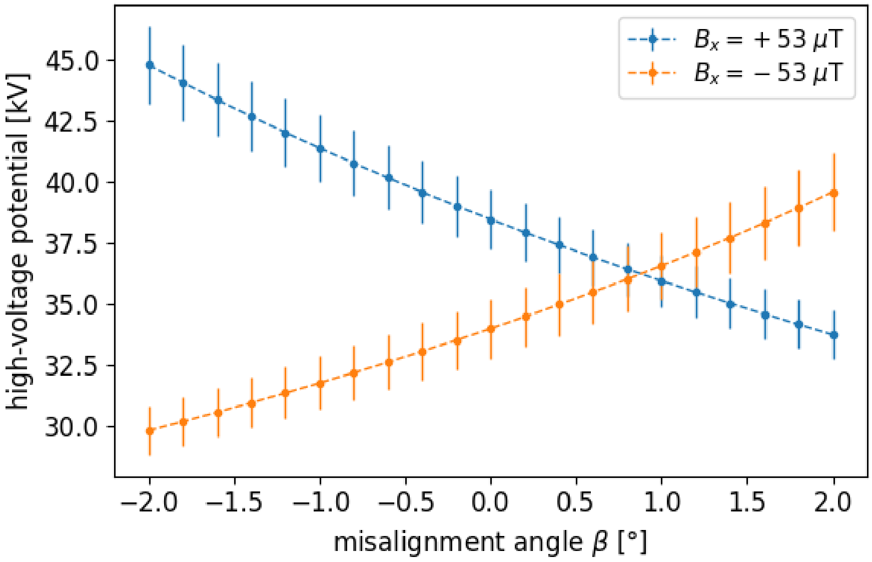

Figure 34: *Optimization of the misalignment angle β. The high-voltage potential was calculated using Eq. (16) for the two polarities $B_h = +53\ \mu\mathrm{T}$ (blue) and $B_h = -53\ \mu\mathrm{T}$ (orange). The misalignment angle was optimized to $\beta = 0.87° \pm 0.09°$ such that the two measurements led to the same value of the potential.*

of those phase values we calculated the electric field. The resulting values are presented in Fig. 35.

The four measurements are in good agreement with each other and can be combined to get the value of $U = (36.2 \pm 0.9)\ \mathrm{kV}$. This value is only 3% higher and 1.3 standard deviations away from the nominal value of $35\ \mathrm{kV}$. A reasons for this could be that the angle α or the misalignment β was slightly bigger than calculated.

We performed a second analysis where we compared the measurements of the top and the bottom beam of each run. This has the advantage that no drift correction is required since the measurement that are compared were taken at the same time. This analysis provided a value of $U = (36.2 \pm 0.5)\ \mathrm{kV}$ with the same corrections applied. It is in good agreement with the first method.

It is unlikely that the power supply provides a high-voltage potential that is above the range and 3% off the set value as the data sheet of the FUG HCP states a relative precision and accuracy of $\pm 1 \times 10^{-4}$ [73]. Since we do not have another method to measure the potential, we decided to use to conservative value of $U = 35\ \mathrm{kV}$ for the further ALP analysis.

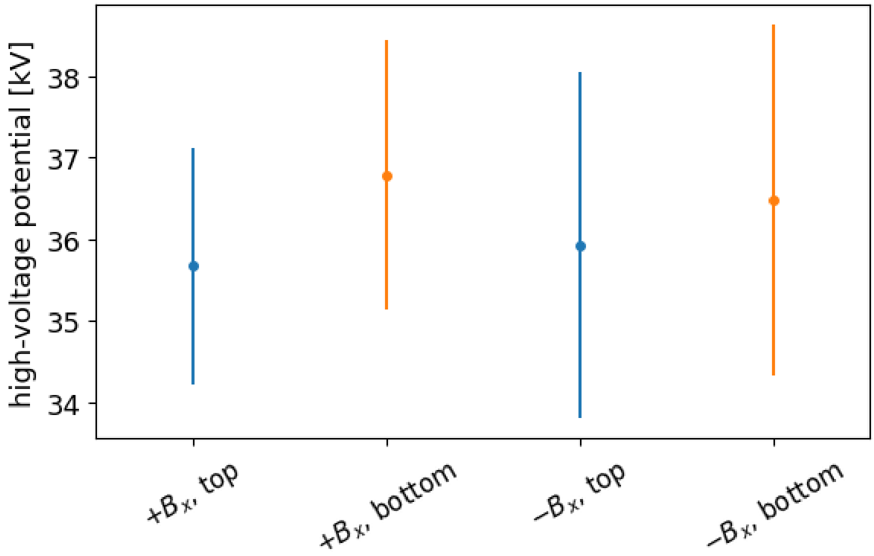

Figure 35: *Calculated high-voltage potential values using Eq. (16) for the top beam (blue) and the bottom beam (orange) for both directions of* B_h*. The four measurements can be combined and lead to a value of* $U = (36.2 \pm 0.9)\ \mathrm{kV}$*.*

4 Axion-Like Dark Matter Analysis

In this section, we describe the analysis of the ALP search. We first describe the chosen analysis algorithm and the spectral analysis in Sec. 4.1. We then give a short introduction into the stochastic and deterministic dark-matter model in Sec. 4.2. Finally in Sec. 4.3, we describe the analysis of the ALP search that led to the published result.

4.1 Spectral Analysis

As described by Eq. (4), the coupling of the ALP field to the neutron results in an oscillating EDM. To find such a tiny oscillating signal, a spectral analysis of the EDM data has to be performed.

The presented analysis uses a total of 24 hours of data, taken with a sampling rate of $4\ \mathrm{kHz}$, i.e., we obtained a value for the neutron asymmetry and, hence, the neutron EDM every $0.25\ \mathrm{ms}$. This corresponds to more than 10^8 data points. The number of frequencies that have to be analyzed for the range with five times the spectral resolution is almost 10^9. There exist a variety of algorithms to perform a spectral analysis based on different analysis principles. A comparison of the performance of various period finding algorithms can be found in [82].

We performed the spectral analysis on the neutron data using an adapted version of the generalized Lomb-Scargle algorithm [83–86]. We chose this algorithm because it can handle non-uniform or gaped data, is based on the fast Fourier transform (FFT) with a calculation time scaling of $\mathcal{O}(n \log n)$, and returns the amplitude of the best-fit sinusoidal signal and its uncertainty. The python code for the original algorithm is part of the *Astropy* package [87–89].

The basic concept is to perform a χ^2 minimization of the fit function

$$f(t) = a \sin(\omega t) + b \cos(\omega t) + c \ , \tag{17}$$

where a, b, and c are the parameters to be minimized for each frequency ω. Instead of minimizing directly, the problem is solved analytically for the three parameters. The resulting sums are Fourier series that can be calculated using fast algorithms. The source code of the algorithm can be found in the Appendix A.1. The neutron asymmetry amplitude $\hat{\mathcal{A}} = \sqrt{a^2 + b^2}$ is Rayleigh distributed assuming only white noise.

The distribution has the probability density function

$$p(\hat{\mathcal{A}}) = \frac{\hat{\mathcal{A}}}{s^2} e^{-\hat{\mathcal{A}}^2/(2s^2)} \ , \tag{18}$$

where s is a scale parameter.

To check the algorithm we measured the calculation time on various data set sizes and compared it to a simple analytic version of the algorithm that does not make use of the FFT and to the `curve_fit` routine, that is an implementation of a least-squares algorithm in the python-scipy package. The spectra were calculated on a single Intel® Core™ i7-8650U CPU and the time scaling is presented in Fig. 36. The extrapolation of the fitted lines to 10^8 data points led to calculation times of 18 minutes (FFT-based), 6 years (simple analytic), and 25 years (least-squares). It is evident that only the FFT-based algorithm is a reasonable option to calculate the spectrum of the neutron data, even if calculated on a high-performance computing cluster.

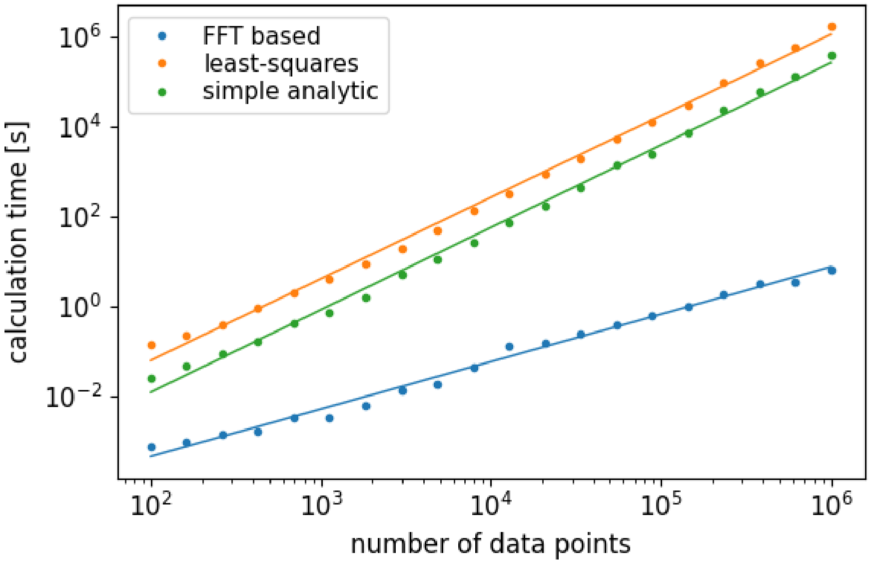

Figure 36: *Time to calculate the spectrum as a function of the size of the data set. The used algorithm that makes use of the fast Fourier transform (blue) is compared to the least-squares `curve_fit` routine of python (orange) and a simple analytic algorithm that calculates the amplitude without using the fast Fourier transform (green). The solid lines correspond to linear least-squares fits in the log-log-plot.*

Since we adapted an existing routine to calculate the spectrum, we tested the algorithm on toy data as well as neutron data from the artificial ALP measurement. We compared the results of the spectral analysis of the three algorithms with each other and the relative differences were below 10^{-3} over the full frequency range.

Data were taken on September 13 and 14, 2020 and are publicly available [90]. A 5 second-long subset of the data is presented in Fig. 37a. The entire data is split into two halves of 12 hours each. Limits are based on the first half of the data, but an oscillating signal would only be considered significant if it appears in the spectral analysis of both sets with a pull or significance $\hat{\mathcal{A}}\,/\,\sigma_{\hat{\mathcal{A}}}$ of more than five.[h]

We subtracted the asymmetry amplitudes of both neutron beams, i.e., opposite electric field directions, from each other. Figure 37b shows how this eliminates the eminent 50 Hz signal coming from the power line frequency. The peak is visible in the spectra of both beams separately but not in the spectrum of the difference.

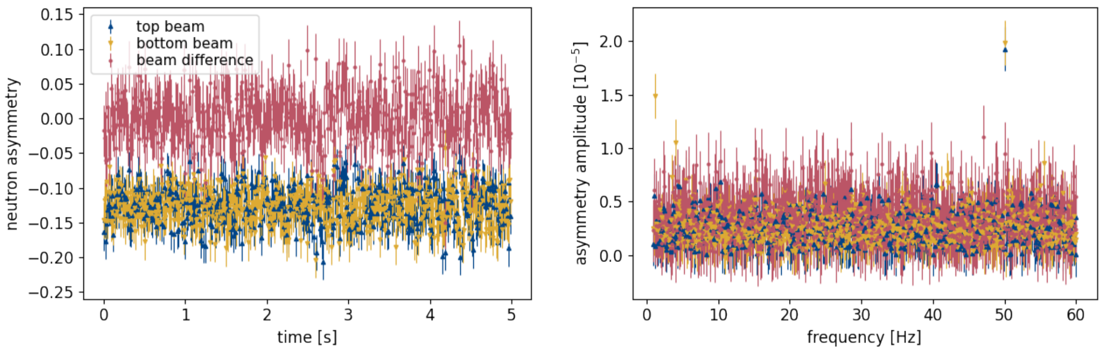

(a) (b)

Figure 37: *The data for the top beam (blue ▲), the bottom beam (yellow ▼), and the difference between the two beams (red ●). Note that only a fraction of the data points is shown for legibility in both subfigures. (a) Measured neutron asymmetry for a time window of* 5 *seconds. (b) Frequency spectrum between* 1 Hz *and* 60 Hz *based on the whole* 12 *hour data set. The highly significant signal at* 50 Hz *from the power line frequency is canceled out by analyzing the beam difference.*

The overall spectrum shows three groups of significant signals of different origins that are not ALPs.The first group appears for frequencies below 10 mHz. They can be explained by long-term magnetic gradient field drifts due to temperature changes. They happen on

---

[h] If the signal amplitude was Normal distributed, this would be called the 5-sigma level and corresponds to a probability of $1/1'744'278$ that the signal origins from a statistical fluctuation only. It can be calculated by integrating a Normal distribution with a mean of zero and standard deviation of one in a 5-sigma range. To have the same probability for a Rayleigh distributed amplitude, a significance of 5.36 would be required. Since the signal follows a Rayleigh distribution, using the term "5-sigma level" may be misleading.

the time scale of hours and result in a rise in signal amplitude.

The second group is located in the frequency range between $10\ \mathrm{mHz}$ and $2\ \mathrm{Hz}$. They are caused by the data structure itself and a sub-range is presented in Fig. 38. Our sequence of data taking is divided into runs of $62.5\ \mathrm{s}$ duration. Each run consists of $57.5\ \mathrm{s}$ of measurement time and $5\ \mathrm{s}$ of downtime to save the data. This time structure leads to peaks at the inverse run time of $16\ \mathrm{mHz}$ and higher orders. Additionally, the $5\ \mathrm{s}$ gap leads to an envelop hump structure with a period of $200\ \mathrm{mHz}$. For frequencies higher than $2\ \mathrm{Hz}$, these peaks are too small to emerge over the background noise level.

To confirm that the peaks actually originate in the data structure, we performed the spectral analysis on a dummy data set as suggested by [86]. It had the same time structure but consisted only of ones when data was taken and zeros when not. The resulting spectrum showed the same peak structure after the normalization of the spectral amplitudes.

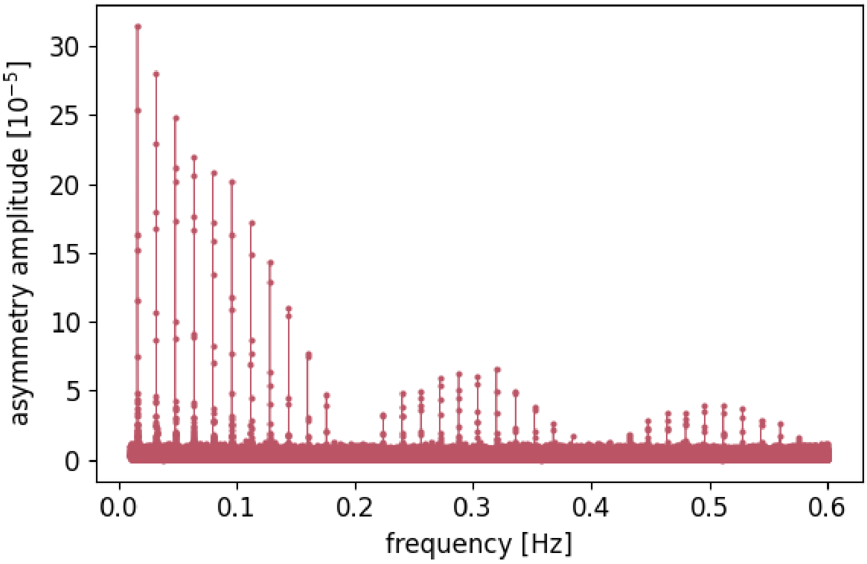

Figure 38: *Spectrum of the frequency range between* $10\ \mathrm{mHz}$ *and* $0.6\ \mathrm{Hz}$ *from the data of the difference between the two beams. Discrete peaks appear in the spectrum due to the data structure. Note that the plot is based on the whole* 12 *hour data set and that only a fraction of the data points is shown for legibility.*

The third group of significant signals has a statistical origin. Since the asymmetry amplitudes follow a Rayleigh distribution, the pull/significance is also distributed accordingly. We found $113 \pm 11_{\mathrm{stat}} \pm 9_{\mathrm{sys}}$ and $132 \pm 11_{\mathrm{stat}} \pm 13_{\mathrm{sys}}$ events above the significance threshold of five in the first and second half of the data, respectively. The frequencies of the events of both sets do not coincide. The systematic error originates from the uncertainty of the detector count-error calibration. These values are slightly below the 162 statistically expected events for a data set with 43.6 million analyzed frequencies. Nevertheless, they agree with the number of significant events of $118 \pm 11_{\mathrm{stat}} \pm 11_{\mathrm{sys}}$ in a data set with no electric field present. These data serve as a reference since no ALPs signal can be present as the ALP field couples to the electric field. Overall, no significant oscillating signal was found at the same frequency in both partial data sets.

With the use of Eq. (12), the neutron asymmetry amplitude shown in Fig. 37b and Fig. 38 can be translated into the pseudo-magnetic field amplitude. The full spectrum with a reduced spectral resolution is shown in Fig. 39. The most sensitive region of a few pT is in the central flat region.

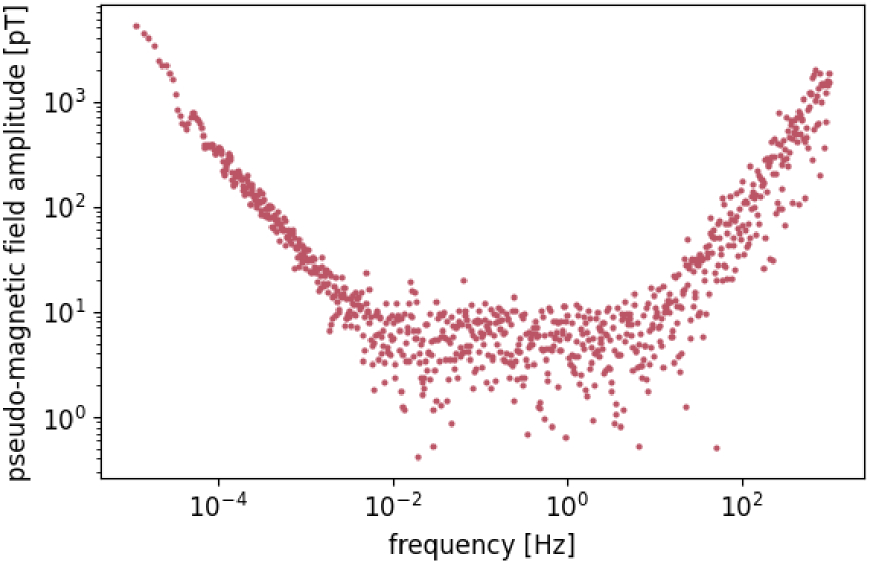

Figure 39: *The neutron asymmetry spectrum translates into a pseudo-magnetic field spectrum after applying the calibration as shown in Fig. 27. The error bars were omitted for reasons of readability but are of order* $3\ \mathrm{pT}$ *in the most sensitive central range. Note that the plot is based on the whole* 12 *hour data set and that only a fraction of the data points is shown for legibility.*

4.2 Dark-Matter Model

The oscillation amplitude of the dark matter field relates to its density via $a_0 = \sqrt{2\rho_{\mathrm{DM}}}/m_a$, assuming all dark matter consists of ALPs. Recently, J. W. Foster et al. published the possible effects of the dark-matter substructure to the upper limits set by axion and ALP experiments [91]. Depending on the ratio of the measurement time over the coherence time of the dark-matter field T/τ_c, it behaves either deterministic or stochastic. The coherence time of the dark-matter field is 10^6 periods of the oscillating signal and our measurement time 12 hours.[i] Figure 40 shows a simulation of the dark matter amplitude from [92] that illustrates the differences.

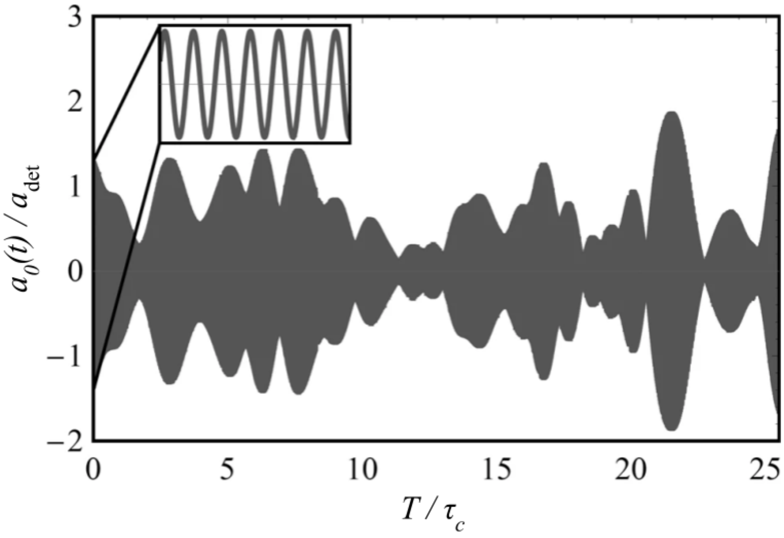

Figure 40: *Simulation of the dark-matter amplitude of a virialized ultralight field as a function of the time, normalized by the coherence time τ_c. The amplitude is normalized by the deterministic dark matter amplitude a_{det}. Picture courtesy of [92].*

For $T \gg \tau_c$, the field is deterministic and the local dark-matter density averages to $\rho_{\rm DM} = 0.2 - 0.7\ {\rm GeV/cm^3}$ [93]. To be consistent with the measurement of the nEDM collaboration [43], we chose a value of $\rho_{\rm DM} = 0.4\,{\rm GeV/cm^3}$ [94].[j] In Fig. 40, this corresponds to taking the time average of the dark-matter amplitude that then becomes $a_{\rm det} = a_0$. Additionally, since the measurement time is bigger than the coherence time, the measured line shape of the dark-matter field gets broadened.

On the other hand, if $T \ll \tau_c$, the field is stochastic and a measurement samples only a small subset of the dark-matter amplitude shown in Fig. 40. This amplitude follows a

---

[i] The coherence time of the field can be calculated in the framework of the standard halo model of dark matter [49]. The viralized velocity of the local dark matter is $v_{\text{vir}} = 10^{-3}\,c$. The coherence time, defined as $\tau_c \equiv \frac{c^2}{f_c v_{\text{vir}}^2}$ with the Compton frequency $f_c = \frac{mc^2}{h}$, leads to a coherence time of 10^6 periods of the oscillating signal [92].

[j] This corresponds to a value of $\rho_{\rm DM} = 3.1 \times 10^{-42}\ {\rm GeV^4}$ in natural units.

Rayleigh distribution with scale parameter $a_{\mathrm{det}}/\sqrt{2}$

$$p(a_0) = \frac{2a_0}{a_{\mathrm{det}}^2} e^{-a_0^2/a_{\mathrm{det}}^2} \ , \tag{19}$$

which implies that about 63% of the time of the measurement, the amplitude will be smaller than a_{det}. This has to be taken into account when placing a constraint from a measurement where no signal has been found. If a signal was measured, it is coherent over the course of the measurement as indicated by the inset in Fig. 40 which results in a narrow line shape. This means that if a signal was found, the line shape of the signal provides information about the local dark-matter substructure.

The above described scenarios cover only the extreme cases but not the case where $T \approx \tau_c$. Since our measurement time and frequency range also covers this case we simulated the dark matter signal, following the approach of [91]. This approach includes models of the dark-matter amplitude distribution, the dark-matter speed distribution, and the local axion distribution. Together they define the line shape of a possible dark-matter signal in our measurement. Figure 41 shows three cases of $T/\tau_c = 0.5$, $T/\tau_c = 1$, and $T/\tau_c = 2$.

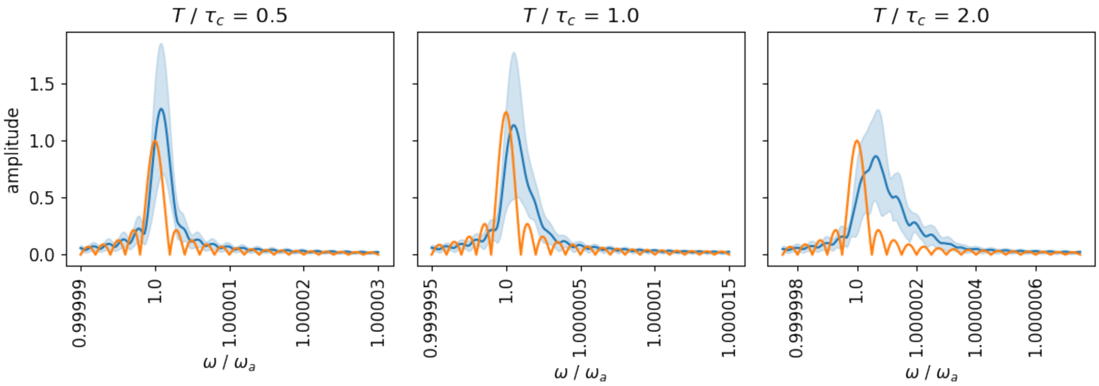

Figure 41: *Simulation of the dark matter line shape. It shows the spectrum for the three cases $T/\tau_c = 0.5$ (left), $T/\tau_c = 1$ (center), and $T/\tau_c = 2$ (right). The orange spectrum corresponds to the optimal case where the field oscillates coherently and is a simple sinusoidal signal. The blue spectrum corresponds to the case where the dark-matter distribution is taken into account. The shaded area indicated the uncertainty of the simulation. The x-axis is normalized to the signal frequency and the y-axis has arbitrary units.*

For a measurement where the measurement time is shorter than the coherence time, the dark-matter signal is similar to the optimal case of a pure sinusoidal signal. As the measurement time increases, the field becomes incoherent and the dark-matter line shape gets broadened and the line shifts to higher values. This is only a qualitative simulation and a more sophisticated one would be required to explain the transition from deterministic to stochastic dark matter. Since this was out of the range of this analysis, we calculate and display both limits in Sec. 4.3.

4.3 ALP-Gluon Coupling

In Sec. 4.1 we described the search for an oscillating signal in the neutron EDM data. Besides having a significant amplitude over the background noise level, an actual oscillating EDM signal must disappear if no electric field is applied. This way, noise signals or signals from external sources can be further excluded. For this, we performed an additional measurement with no electric field applied. Moreover, the amplitude of a real signal must be identical for both electric field directions but must exhibit a phase-shift of π.

We did not explicitly have to apply these additional conditions. Nevertheless, some signals as the eminent signal at $50\ \mathrm{Hz}$ from the power line frequency, could be removed by taking the difference in the signals of the two beams with opposite electric field directions as visible in Fig. 37b. They cancel because they have the same phase and amplitude in both beams. Also, the peaks of the data structure have the same phase for any electric field direction and can be excluded with the same argument.

Since no significant signal was found, an upper limit on the ALP-gluon coupling can be derived. Using Eqs. (4) and (8) as well as the calibration shown in Fig. 27, the coupling can be calculated with

$$\frac{C_G}{f_a} = \frac{\gamma_n \hbar B_a}{a_0 E \times 4.8 \times 10^{-16}\, e\,\mathrm{cm}}. \tag{20}$$

The potential of the central high-voltage electrode was set to $+35\ \mathrm{kV}$. Hence, the electric field used for the evaluation is $E = 2 \times 35\ \mathrm{kV/cm}$ as all the analysis is done for the difference of the two beams.

The upper limit at a given frequency is calculated by integrating the normalized distribution of C_G/f_a up to the C.L. of 95%. Hence, the upper integration constant corresponds to the upper limit of the ALP-gluon coupling. Figure 42 shows a histogram of the distribution for the deterministic and stochastic dark matter together with calculated upper integration constant for the signal at $1\ \mathrm{Hz}$.

In the case of deterministic dark matter, C_G/f_a follows solely a Rayleigh distribution since B_a is Rayleigh distributed. However, in the case of stochastic dark matter, it corresponds to the ratio of two Rayleigh distributions since $a_0 = a_{\mathrm{stoch}}$ is also Rayleigh distributed. In this case, the overall distribution has a much longer tail, resulting in a higher upper limit. The upper limit is frequency dependent and has to be calculated for the full spectrum. We did

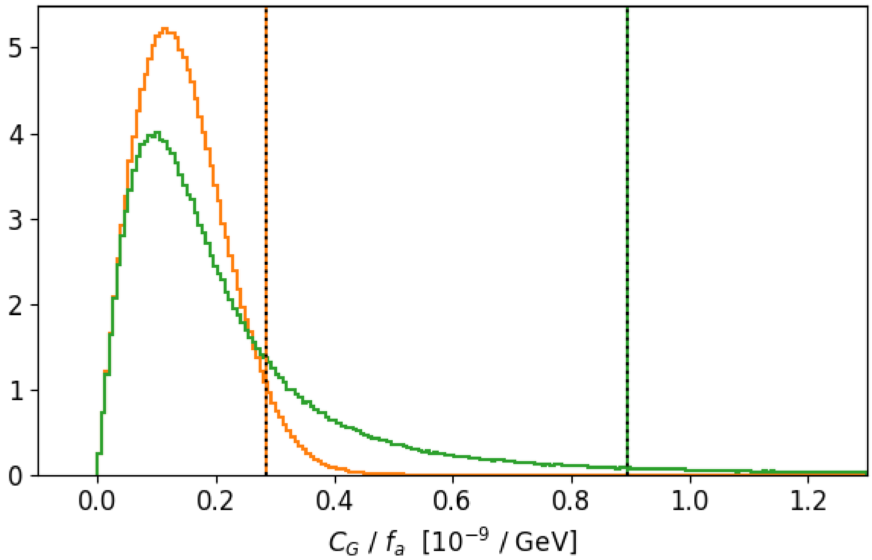

Figure 42: *Histogram of the normalized distribution from a Monte-Carlo sampling of* C_G/f_a *at* 1 Hz *for the deterministic dark matter (orange) and the stochastic dark matter (green). The vertical dashed lines show the upper integration constant when the integral value is* 0.95 *and thus the upper limit for each distribution at* 95% *C.L..*

this for a reduced number of frequencies, i.e., 7263, with a logarithmic spacing. The results for both dark matter cases are shown in Fig. 43, were we divided the limit by the mass m_a to determine the scaling factor of the stochastic limit.

Figure 43 shows the must stringent constraint of $C_G/f_a m_a = 2.7 \times 10^{13}\ \mathrm{GeV}^{-2}$ and $C_G/f_a m_a = 8.7 \times 10^{13}\ \mathrm{GeV}^{-2}$ at 95% C.L. for deterministic and stochastic dark matter in the frequency range between 5 mHz and 5 Hz, respectively. This leads to a scaling factor of the stochastic limit of 3.2 ± 0.3 compared to the deterministic limit, in agreement with similar calculations by the CASPEr collaboration [95].

Figure 44 shows our exclusion region of the ALP-gluon coupling as a function of mass or frequency. For frequencies below 5 mHz, the upper limit increases due to magnetic gradient field drifts. For frequencies above 5 Hz, the upper limit increases due to a decrease in sensitivity of the apparatus, as shown in Fig. 39. For reasons of legibility, we smoothed the limits in Fig. 44 with a Savitzky-Golay filter [97]. Therefore, the fine structure, visible in Fig. 38 and Fig. 39, disappears. The second y-axis on the right side uses the relation [31, 32]

$$g_a = (3.7 \pm 1.5) \times 10^{-3} \left(\frac{C_G}{f_a}\right) \frac{1}{\mathrm{GeV}} . \tag{21}$$

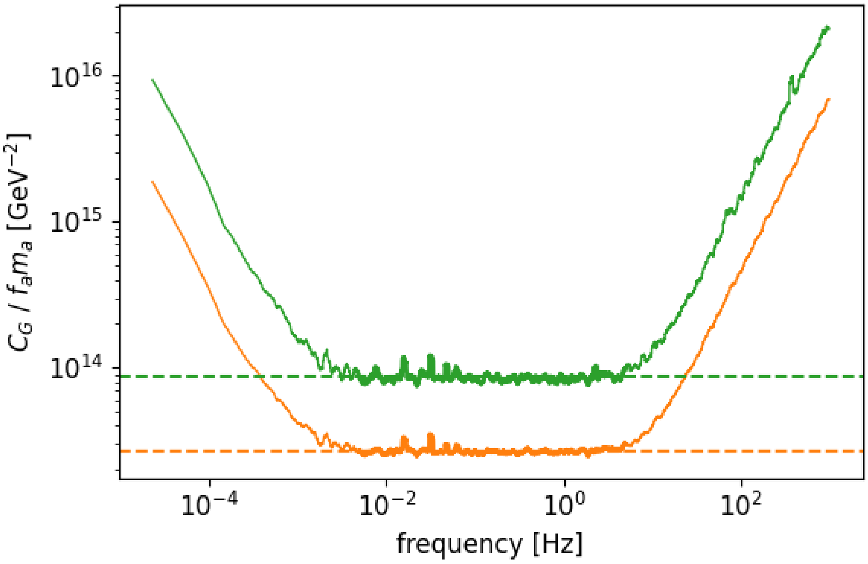

Figure 43: *Calculated upper limit of C_G/f_a divided by the mass m_a over the full spectrum for deterministic dark matter (orange) and stochastic dark matter (green). In the central flat region between $5\ \mathrm{mHz}$ and $5\ \mathrm{Hz}$, the mean was calculated and is indicated by the dashed lines.*

As a calculation example: an oscillating magnetic field amplitude of $B_a = 10\ \mathrm{pT}$ which is typical for the central frequency range (see Fig. 39) translates with Eq. (8) and $E = 2 \times 35\ \mathrm{kV/cm}$ into a neutron EDM amplitude of $d_n = 8.6 \times 10^{-24}\, e\,\mathrm{cm}$. With the use of Eq. (20) this can be translated into an ALP-gluon coupling of $C_G/f_a = 1.4 \times 10^{-11}\ \mathrm{GeV}^{-1}$ for an ALP mass of $m_a = 10^{-15}\ \mathrm{eV}$. It follows $C_G/f_a m_a = 1.4 \times 10^{13}\ \mathrm{GeV}^{-2}$.

To provide context, the constraints on 95% C.L. from the other laboratory experiments are also presented. In addition, astrophysical and cosmological constraints explained in Sec. 1.3 arise from galaxy luminosity functions at high red-shifts, BBN models, and the SN1978A cooling. The QCD-axion line shows the region where an axion would simultaneously solve the strong *CP* problem and explain all dark matter.

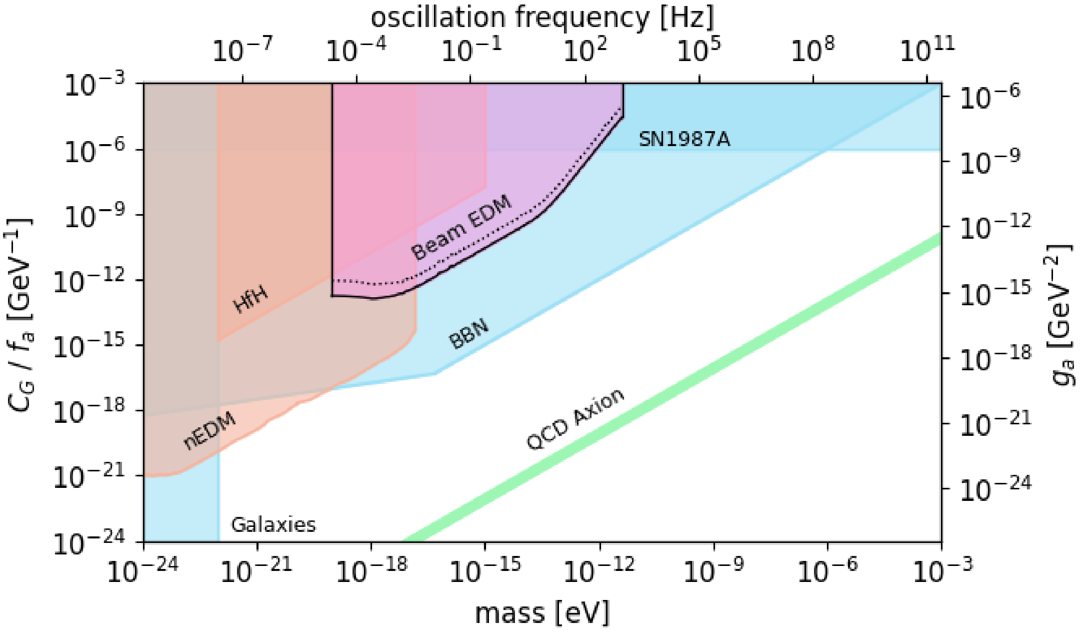

Figure 44: *Limits on the ALP-gluon coupling are shown as a function of the mass or frequency. The shaded areas are exclusion regions from cosmology and astrophysical observations (blue: Galaxies [48], BBN [50, 51], SN1987A [54, 96]) and laboratory experiments (orange: nEDM [43], HfH [44]). The black outlines with the pink area mark the exclusion region of this publication (labeled Beam EDM). The solid and dotted lines correspond to the deterministic and stochastic dark-matter models, respectively. The green line shows the canonical QCD-axion. The second y-axis on the right side uses the relation of Eq. (21).*

5 Summary

In summary, we gave an overview of the strong *CP* problem and how a solution of it led to axions and ALPs. We provided a theoretical background to understand how they couple to the neutron EDM and what laboratory experiments and astrophysical/cosmological observations constrain their existence. We further summarized the experimental *Beam EDM* apparatus that we used to search for an oscillating signal. We explained in detail the calibration of the count error of our CASCADE neutron detector. We showed how we characterized the sensitivity of the apparatus with respect to oscillating (pseudo-)magnetic fields and how we got aware of the effect we call resonant cancellation. We investigated this effect with simulations and a dedicated beamtime. We performed a search for ALPs but did not find a significant oscillating signal. With only 24 hours of data, we could constrain an ALP-gluon coupling in a mass region covering almost eight orders of magnitude. Together with the results of two other laboratory experiments, a large region of the ALP-dark-matter parameter space could be excluded. To increase the sensitivity of the experiment, more neutrons and higher electric fields are required. Additionally, the interaction length of the experiment should be increased. This is all possible when the proof-of-principle *Beam EDM* apparatus is built full-scale at the European Spallation Source (ESS). To cover a lower mass range, the total time of data taking has to be increased. However, this range is already covered by the other laboratory experiments. To cover higher masses, a faster sampling of the detector is required. This is only helpful if the effect of the resonant cancellation can be minimized or overcome by working with neutron pulses in a time-of-flight measurement, or by making the interaction length shorter on the cost of sensitivity. Simulations would be required to optimize the setup for the higher mass range.

Part II

Exotic Yukawa-Like Interaction

6 Introduction

Ramsey's technique of separated oscillatory fields, described in more detail in Sec. 2, can be applied to precisely measure magnetic and pseudo-magnetic field changes. It was also used in the measurement of the neutron magnetic moment [98]. In this experiment, the technique was applied to compare resonance frequencies of free neutrons and the hydrogen protons in water using the same geometry. The application of the resonance technique of separated oscillatory fields on flowing water had been previously demonstrated by Sherman [99].

Here we present the experimental apparatus with a similar concept as the one used for the neutron magnetic moment measurement. The goal of this *Proton NMR* setup is to search for a new exotic Yukawa-like interaction in the millimeter range. Such a long-range interaction between two fermions could be part of an extension to the Standard Model of particle physics (SM) [100]. To date, only a few experiments have been conducted that constrain the existence of such an interaction and none of them used protons as a probe particle.

This part of the thesis is organized as follows. We first describe the experimental apparatus in detail in Sec. 7. During the course of my Ph.D., the experimental apparatus was designed and built, then further developed and optimized. In Sec. 8 and Sec. 9 we describe the characterization measurements performed in Rabi and Ramsey configurations, respectively. Those well-understood measurements can be used to show that the setup works as expected and to characterize its sensitivity and stability. In Sec. 10 and Sec. 11 we show the investigation of the two radio-frequency (RF) effects called Bloch-Siegert shift and dressed spin states, respectively. We then conclude with the theory and the search for the new Yukawa-like interaction between two fermions in the millimeter range in Sec. 12.

7 Proton NMR Setup

In this section, the setup of the experimental *Proton NMR* apparatus is explained. The setup was developed in collaboration with the master's student J. Smits [101]. Figure 45 shows a schematic of the experimental setup and Fig. 46 a photo of the full tabletop experiment. The total length is about 3 meters.

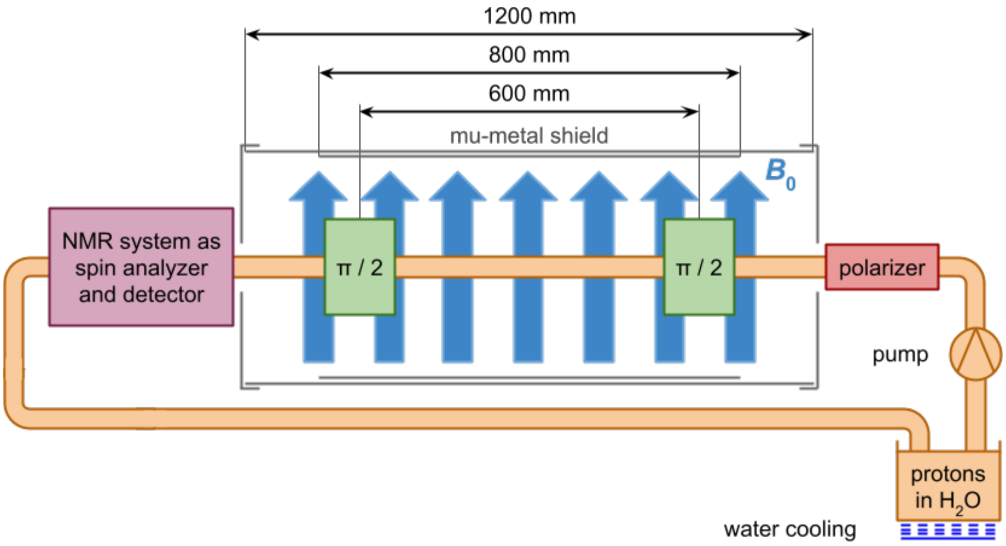

Figure 45: *Schematic of the experimental setup where the H_2O is pumped from the water reservoir of the chiller. They are first polarized in a polarizer (red) and then enter the interaction region that is surrounded by a double layer mu-metal shield. Two spin-flip coils are shown in green and the magnetic field direction is indicated in blue. The spin polarization is analyzed using a nuclear magnetic resonance (NMR) system (purple). The schematic is not to scale.*

The water is pumped through the system using a small gear pump as described in Sec. 7.1. First, the water passes a polarizer, described in Sec. 7.2, to create a sizable spin polarization of the protons. It then flows through the interaction zone, explained in Sec. 7.3, that is magnetically shielded by mu-metal. In that zone, the spins interact with the magnetic field B_0 and can be manipulated with spin-flip coils. There are additional temperature and magnetic field sensors. Finally, the spin polarization is measured and analyzed by means of NMR techniques as explained in Sec. 7.4.

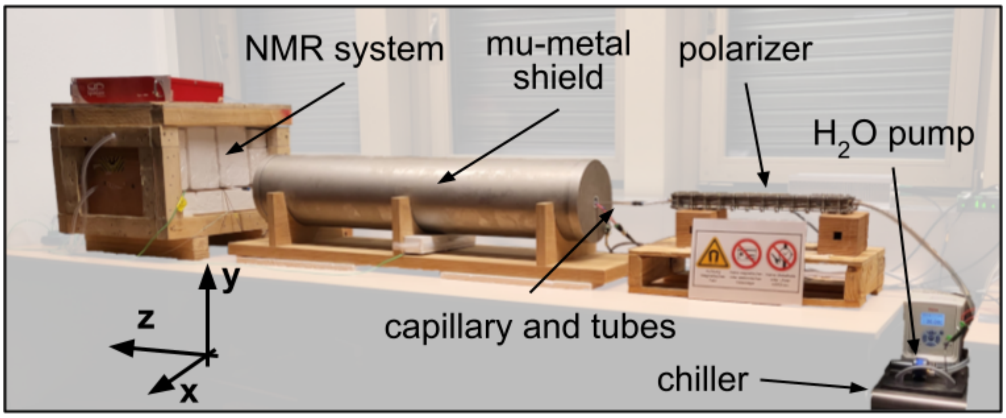

Figure 46: *Photo of the experimental setup where the water flows through the shield in a glass capillary from right to left. The gear pump is mounted on the water chiller. The first element the water passes is the polarizer. It then enters the interaction region surrounded by the magnetic mu-metal shield. Finally, it is measured with an NMR system. The NMR magnet is temperature stabilized and insulated.*

7.1 Water Circuit

To manipulate the proton spins of the hydrogen in the water molecules, a water circuit is required. We use plastic tubes (PU, PVC, and PTFE) of various diameters and a rigid glass capillary with an inner diameter of $d = 4$ mm and a length of 1500 mm in the interaction zone to guide the water through the setup.

The pump has to provide a constant and high enough flow and pressure. We use a gear pump MGD2000F [102] with flow and pressure ratings of 2.3 l/min and 6 bar, respectively. This is suitable to transport the water through the setup within a few seconds to maintain enough polarization and overcome all pressure losses of the system. The speed of the pump can be controlled with a voltage from $0 - 5$ V. The measured flow rate of the pump versus the applied voltage is shown in Fig. 47. It also shows the average velocity through the glass capillary in the interaction zone since this is an interesting property for many resonance measurements. The flow rate (velocity) is linear in the measured range and a linear fit led to the values of $(0.53 \pm 0.02)\ \mathrm{l/min \cdot V^{-1}}$ ($(0.71 \pm 0.02)\ \mathrm{m/s \cdot V^{-1}}$).

The flow velocity was set to $v = 2.35$ m/s in all measurements if not stated otherwise. This velocity was optimized for highest signal visibility while operating the pump and water tubing within the safety margins of the pressure ratings. This velocity is the mean or group velocity. In reality, the flow follows a profile in the tube with the highest velocity in the center and decreasing velocity towards the tube walls due to the viscous resistance. It depends on

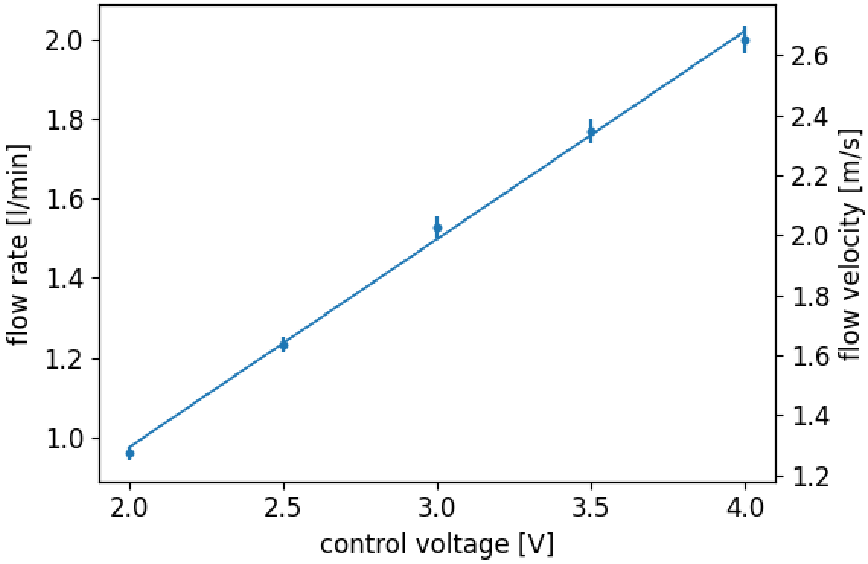

Figure 47: *Flow rate of the water through the pump as a function of the applied control voltage. The vertical axis on the right side shows the average velocity of the water through the glass capillary in the interaction zone with the inner diameter of* $4\ \mathrm{mm}$. *The solid line is a linear fit through the data.*

the type of flow that is defined by the Reynolds number Re [103] which in a tube is

$$Re = \frac{\rho v d}{\mu} \ , \tag{22}$$

where $\rho = 998.2071\ \mathrm{kg/m^3}$ is the density and $\mu = 1.0016\ \mathrm{mPa \cdot s}$ the dynamic viscosity of water at $20\ °\mathrm{C}$ [104]. This leads to a Reynolds number of roughly 9400. The transition from laminar to turbulent flow is dependent on many parameters but usually it occurs at Reynolds numbers between 2300 and 2600 [105]. For lower numbers the flow is laminar and for higher numbers the flow is turbulent. The flow through the capillary is, therefore, in the turbulent regime. The velocity in the tube as a function of the radial position then follows approximately a power-law velocity profile [106]

$$\frac{v(r)}{v_m} = \left(1 - \frac{r}{R}\right)^{1/7} \tag{23}$$

where v_m is the maximum flow velocity in the center of the tube, R the tube radius, and the factor of $1/7$ is an empirical value that depends on the Reynolds number. Overall, this velocity profile is flatter than the quadratic profile of the laminar flow, which has the advantage of better signals in the resonance measurements.[k] However, turbulent flow results in a much higher pressure in the system due to higher friction [108] which had to be taken into account when selecting the pump and the water components.

The pump is mounted on a chiller, that is a temperature stabilized bath circulator Thermo Scientific ARCTIC A10-SC150 [109]. The pump uses the water from the chiller's reservoir that is kept at a temperature of $20\ ^\circ\mathrm{C}$ to minimize systematic effects.

7.2 Polarizer

To perform a spin precession experiment, the particles have to be polarized first. The polarization of the proton spins in an external magnetic field as a function of the time follows an exponential law [110]

$$P(t) = P_0 \times (1 - e^{-t/T_1}) \ , \tag{24}$$

where P_0 is the maximum value of the relative polarization for protons in water at $20\ ^\circ\mathrm{C}$ that depends only on the magnetic field strength of the polarizer. $T_1 = (2.35 \pm 0.02)\ \mathrm{s}$ is the longitudinal or spin-lattice relaxation time constant which was measured using an inversion recovery pulse sequence [111]. The details of the measurement and the results are presented in Sec. 7.4.4. To achieve a polarization of $P(t) > 0.99\, P_0$ the water has to spend $5 \cdot T_1 \approx 12\ \mathrm{s}$ within the polarizer.

The polarizer we built makes use of strong neodymium permanent magnets. For small volumes, this approach is much simpler and cheaper than an electromagnet as it does not require high currents or rely on water cooling. The magnets we used are Q-40-10-05-N with grade N42 from supermagnete [112]. They have a size of $40 \times 10 \times 5\ \mathrm{mm}^3$ and are staked on both sides of an aluminum body where the water flows through. To create a homogeneous magnetic field over the full polarizer volume, steel plates with a thickness of $5\ \mathrm{mm}$ cover the body on both sides. The cover plates are also used to hold the body and all the magnets in place. With this design, the magnetic field in the interior is roughly $190\ \mathrm{mT}$. This was simulated using the *Finite Element Method Magnetics* software [113] and measured using a Hall-probe [114]. The result of the simulation is shown in Fig. 48. Applying Maxwell–Boltzmann statistics with the given temperature and magnetic field leads to a relative polarization of the proton spins of $P_0 \approx 10^{-6}$.

The water flows through the aluminum body in a meandering groove. The outer cross-

---

[k] For laminar flow, the velocity profile is $v(r)/v_m = 1 - (r/R)^2$ according to the Hagen–Poiseuille equation [107].

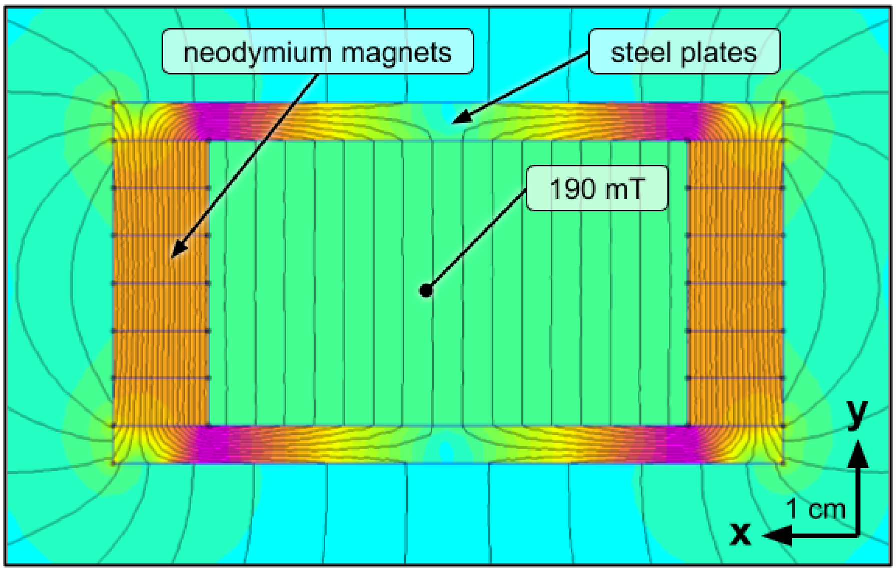

Figure 48: *Result of the simulation of a simplified polarizer model. The model shows the contour lines of the magnetic field and the colors represent the field strength. Blue corresponds to a low and pink to a high field strength. The field strength in the interior area where the water flows is roughly* $190\ \mathrm{mT}$ *in the vertical direction.*

section of the body is $30 \times 50\ \mathrm{mm}^2$ and it has a length of $480\ \mathrm{mm}$. The total water volume is $420\ \mathrm{ml}$. With this volume, the water spends more than five time constants T_1 in the polarizer, even for the highest flow rates. On both ends of the body are tube connections for the water inlet and outlet. A CAD model of the polarizer's interior and a photo of the actual polarizer are shown in Fig. 49a and Fig. 49b, respectively.

7.3 Interaction Zone

The interaction zone is where the proton spins interact with constant and oscillating magnetic fields. It is surrounded by a double layer passive magnetic mu-metal shield as shown in Fig. 50a. The outer layer has an inner diameter of $235\ \mathrm{mm}$ and a length of $1200\ \mathrm{mm}$. The inner layer is centered within the outer layer, has an inner diameter of $195\ \mathrm{mm}$, and a length of $800\ \mathrm{mm}$. Both layers have a thickness of $2\ \mathrm{mm}$. End caps for the outer layer are available but usually not used to allow easy access from the outside.[1]

The main magnetic field B_0 is aligned along the vertical y-direction. It can be created

---

[1] The shielding factor of the mu-metal shield was not measured during this project and is unknown.

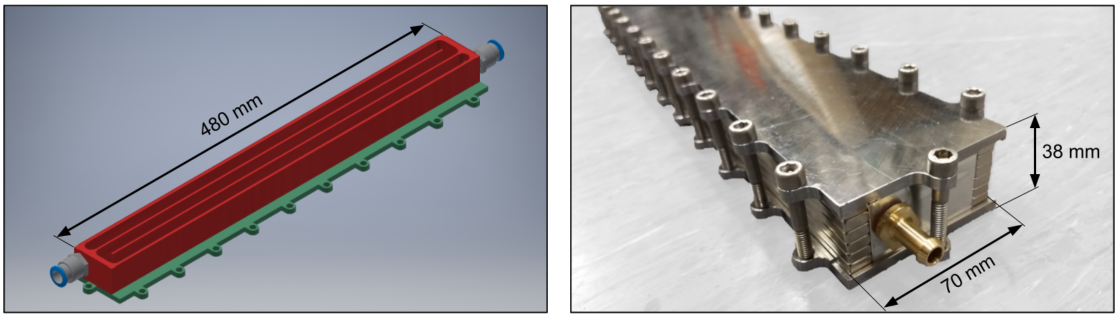

(a) (b)

Figure 49: *(a) CAD model of the polarizer that shows the meandering groove on the inside of the aluminum body (red). The steel base plate (green) below the body is also shown. The permanent magnets on the two sides of the body are not shown. (b) Photo of the polarizer with the water inlet in front. The two steel plates are mounted together with screws to hold the magnets left and right of the aluminum body in place.*

using a square-shaped Helmholtz-type coil with 20 windings that is visible in Fig. 50a. The coil has a width and separation of $128\ \mathrm{mm}$ and a length of $1200\ \mathrm{mm}$. It is centered with respect to the mu-metal shield and connected to a Keysight B2962A Low Noise Power Source [115]. We measured a field constant of the coil of $232\ \mu\mathrm{T/A}$.

Since the interior of the mu-metal shield is hardly accessible, an aluminum U-profile with a grid of threads is mounted to non-magnetic telescopic-rails that are fixed to the mu-metal tube. It can be slid out of the mu-metal to change the arrangement of spin-flip coils, fluxgates, and temperature sensors.

The standard arrangement we use as shown in Fig. 50b is a Ramsey setup that consists of two spin-flip coils with a center-to-center separation of $600\ \mathrm{mm}$. The spin-flip coils are solenoids with 16 windings and their axis is aligned with the water pipe. The coil has a copper wire diameter of $0.8\ \mathrm{mm}$, an inner diameter of $10\ \mathrm{mm}$, and a length of $15\ \mathrm{mm}$. The coils are being held by a holder block that allows to mount a trimming coil to adjust the local magnetic field around each spin-flip coil individually. Photos of a spin-flip coil in the holder block are presented in Fig. 51. A third spin-flip coil can be mounted in the center to perform spin-echo measurements [116].

To manipulate the proton spins, the spin-flip coils have to be driven with an oscillating current close to the Larmor resonance frequency. A connection diagram is shown in Fig. 52. The oscillating currents are provided by Keysight waveform generators 33622A [70]. For each spin-flip coil an output channel is connected to a Mini-Circuits power combiner ZFRSC-2050+ [117]. The second input of the combiner can be used to induce higher frequency

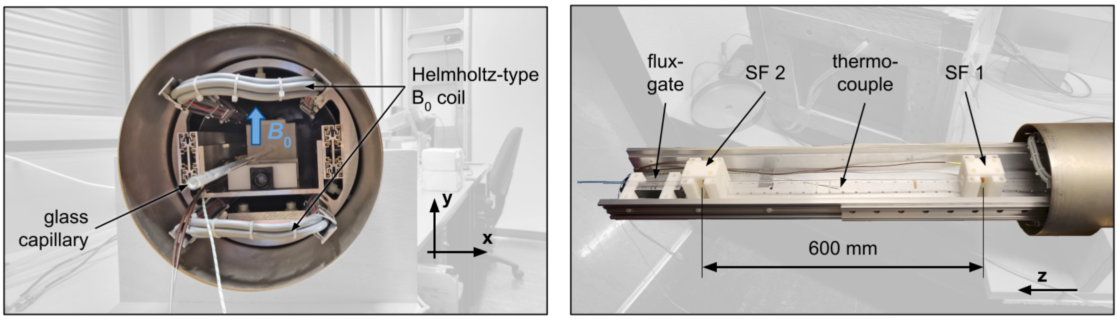

(a) (b)

Figure 50: *(a) Photo of the view into the mu-metal. The inner mu-metal layer is hidden behind an aluminum ring that holds the telescopic-rails. The water flows through the glass capillary in the center. The ends of the square-shaped Helmholtz coil are also visible. (b) Photo of the interaction zone slid out of the mu-metal. Water flows along the z-axis from right to left. The proton spins can be manipulated with the spin-flip coils SF 1 and SF 2. A third spin-flip coil can be mounted in the center. A non-magnetic thermocouple type-E measures the temperature inside and a fluxgate after SF 2 tracks the magnetic field in all three spatial directions.*

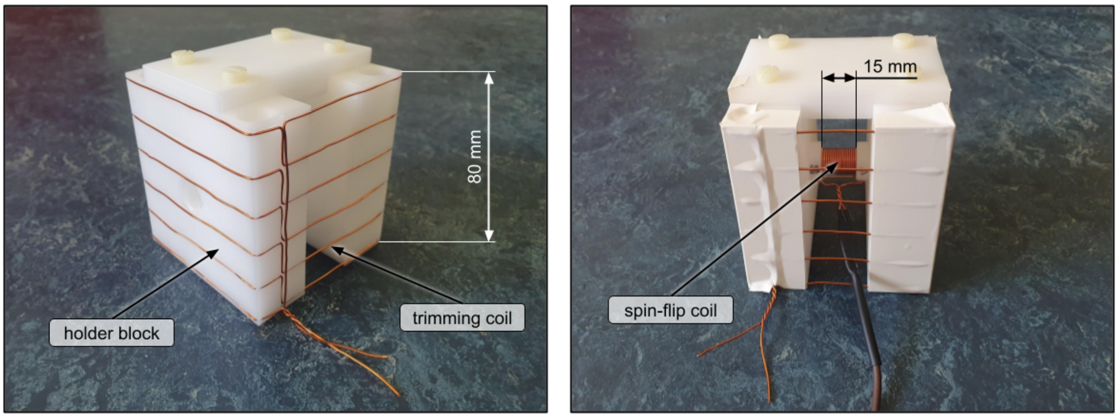

(a) (b)

Figure 51: *Photos of the spin-flip coil and the holder block. (a) The trimming coil around the block can be used to locally change the magnetic field around the spin-flip coil to change the protons' resonance frequency. (b) The mounted spin-flip coil in the shape of a solenoid. The block and its parts are also used to keep the glass capillary where the water flows in place (not shown).*

signals to test effects like the Bloch-Siegert shift and dressed spin states presented in Sec. 10 and Sec. 11, respectively. This second input is terminated with $50\ \Omega$ if it is not used. The output of the combiner is connected to the spin-flip coil via a $20\ \Omega$ resistor to reduce the frequency dependence of the impedance.

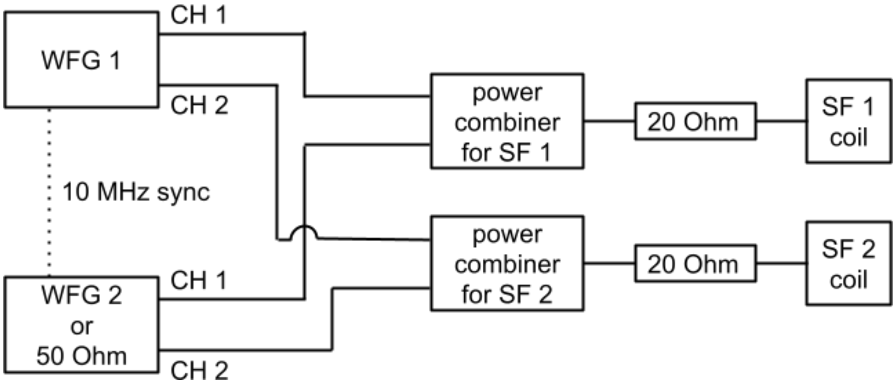

Figure 52: *Connection diagram of the spin-flip coils. The waveform generator (WFG 1) generate the oscillating current. These signals can be combined with the oscillating signal of a second waveform generator (WFG 2) or terminated with a* $50\ \Omega$ *resistor if not used. The output of the combiner is connected to the spin-flip coil (SF 1 and SF 2) via a* $20\ \Omega$ *resistor.*

A non-magnetic thermocouple type-E measures the temperature in the center of the interaction zone close to the glass capillary. Two other thermocouples of type-K measure the temperature of the room below the mu-metal and of the NMR magnet. They are read out with a rate of $2\ \mathrm{Hz}$ and a precision better then $0.025\ ^\circ\mathrm{C}$ using at Picotech data logger TC-08 [118].

The magnetic field is measured using a SENSYS FGM3D/125 fluxgate sensor [65]. It can measure magnetic fields up to $\pm 125\ \mu\mathrm{T}$ with a precision better than $150\ \mathrm{pT}$ in all three spatial directions. It is read out at a rate of $10\ \mathrm{kHz}$ using a NI PXI-6289 analog-digital converter [119]. The data is averaged over 1000 samples and stored at a rate of $10\ \mathrm{Hz}$. The fluxgate is located below the water tube just after the interaction zone as shown in Fig. 50. It cannot be placed between the spin-flip coils since it is slightly magnetic itself and would destroy the spin coherence. The fluxgate data can be used to track and compensate external magnetic field changes.

7.4 NMR System

7.4.1 Setup

We use a commercially available NMR system iSpin-NMR of SpinCore Technologies, Inc. [120] to measure the spin polarization after the interaction. The system contains a pulse generator, a pulse amplifier, frequency filters, a preamplifier, and an analog-digital converter. The system can be programmed to send arbitrary pulse sequences and measure the signal response of the NMR sample. It is able to detect voltages on the $\mu\mathrm{V}$-level. A permanent magnet with a field strength of $0.5\ \mathrm{T}$ comes with the system.

The NMR setup uses the same coil to apply the pulse and to measure the precession signal of the protons. A duplexer is required to route the signal from the transmitter to the probe and from the probe to the receiver but protect the receiver from the high-power transmitter signal. This is done by a passive transmit/receive switch using diodes and a quarter-wave impedance cable. A schematic of the connection diagram is shown in Fig. 53.

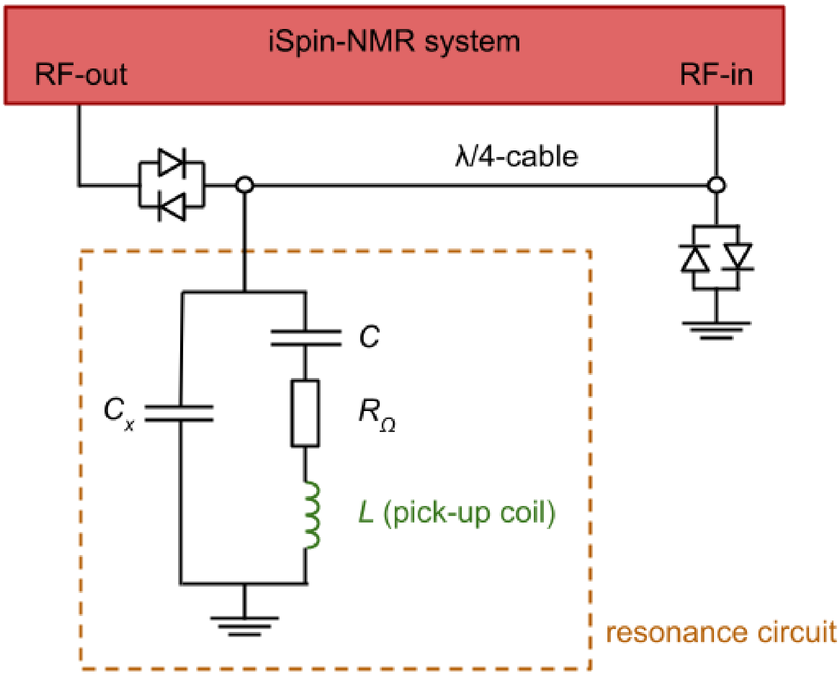

Figure 53: *Connection diagram of the NMR system. The resonance circuit of the NMR detection system has to be matched to* $50\ \Omega$ *and tuned to the proton resonance frequency with the two capacitors* C *and* C_x*. The* $\lambda/4$*-cable and the crossed diodes act as a passive switch that allows signals going from the RF-out to the resonance circuit and from there to the RF-in, but not from the RF-out to the RF-in directly.*

To be able to transmit the power into the water sample and to measure the small precession signal, a RLC resonance circuit is required. The resonance frequency of the circuit has to be tuned to the proton resonance frequency and the impedance has to match $50\ \Omega$. This can be achieved by an additional shunt-capacitor C_x.

The inductance L is given by the pick-up coil. It is made of a copper wire with a diameter of $0.25\ \mathrm{mm}$ that is insulated by a PTFE tube. The coil has 10 windings over $8\ \mathrm{mm}$ and a coil diameter of $4\ \mathrm{mm}$. It has an inner diameter for the water of $3\ \mathrm{mm}$. The ohmic resistance R_Ω comes from the circuit cables and connections. The capacitance of the two capacitors can be calculated analytically but a final adjustment has to be done in-situ. We optimized the capacitors to $C_x = 678\ \mathrm{pF}$ and $C = 251\ \mathrm{pF}$. All parts close to the NMR sample have to be made of a material that does not contain any hydrogen atoms in their molecules as for example most plastics do. The proton signal of those hydrogen atoms would falsify the signal of the protons in the water. We used PTFE/Teflon for all parts close to the sample. A photo of the NMR pick-up coil and the resonance circuit is presented in Fig. 54.

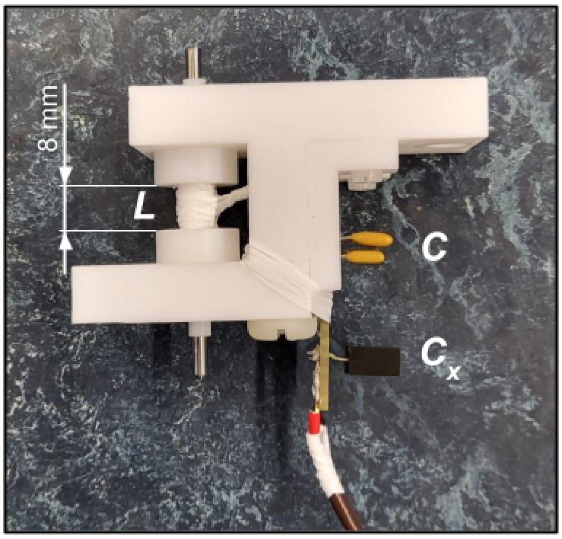

Figure 54: *Photo of the resonance circuit with the NMR pick-up coil. The coil is mechanically stabilized with a small stainless steel rod when it is not inside the NMR magnet since the wall thickness is only* $0.5\ \mathrm{mm}$. *The copper wire of the coil is fixed with PTFE tape to hold it in position. All parts close to the coil are made of PTFE. The capacitors of the resonance circuit are visible in yellow and black.*

The resonance circuit is mounted between the poles of a neodymium permanent magnet visible in Fig. 55. The NMR magnet has a field strength of about $0.5\ \mathrm{T}$ with a relative uniformity of 10^{-4} for a $10\ \mathrm{mm}$ sample according to the manufacturer [121]. The poles have a separation of $30\ \mathrm{mm}$ and a diameter of $140\ \mathrm{mm}$. With a gyromagnetic ratio of the proton of $\gamma_p \approx 2\pi \times 42.58\ \mathrm{MHz/T}$ [122] this leads to a proton resonance frequency of $21.68\ \mathrm{MHz}$.[m]

Daily fluctuations of the room temperature of more than $1\ {}^{\circ}\mathrm{C}$ lead to a change in the magnetic flux density of the magnet. Values from manufacturers suggest a change in the magnetic field, that would lead to a change in resonance frequency of $> 19\ \mathrm{kHz}$ [123, 124]. Since the linewidth of the proton resonance is only a few kHz, a temperature stabilization of the magnet is required. This is done via the water cooling of two aluminum plates on top and below the NMR magnet. The same chiller and water bath described in Sec. 7.1 are used. With this water cooling, a stability of the resonance frequency better than $1\ \mathrm{kHz}$ is achieved. A photo of the NMR magnet with the cooling plates is presented in Fig. 55.

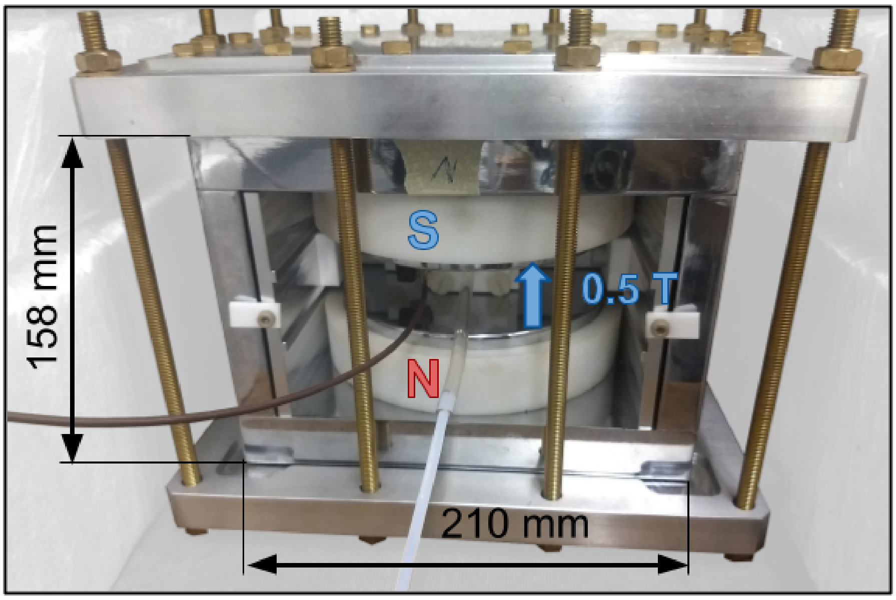

Figure 55: *Photo of the NMR magnet. The two neodymium poles create a magnetic field of roughly* $0.5\ \mathrm{T}$ *in the vertical direction indicated by the blue arrow. The plates for the water cooling are pressed on the magnet with brass thread rods. The holding structure for the resonance circuit and the pick-up coil made of PTFE/Teflon is visible in the center.*

We measured the temperature coefficient of the magnetic flux density for the NMR magnet. For this, we scanned the temperature of the chiller and therefore the NMR magnet. Between each temperature change the magnet was thermalized for about 90 minutes.

---

[m] The gyromagnetic ratio of the free proton is $42.577\,478\,518(18)\ \mathrm{MHz/T}$. For the proton in H_2O it shifts to $42.576\,384\,74(46)\ \mathrm{MHz/T}$ due to the chemical environment.

We measured a temperature coefficient of (-19.07 ± 0.06) kHz/°C at room temperature. This corresponds to a relative coefficient of -8.8×10^{-4} /°C which is in agreement with literature values [123, 124]. Figure 56 shows the measured data with a linear least-squares fit.

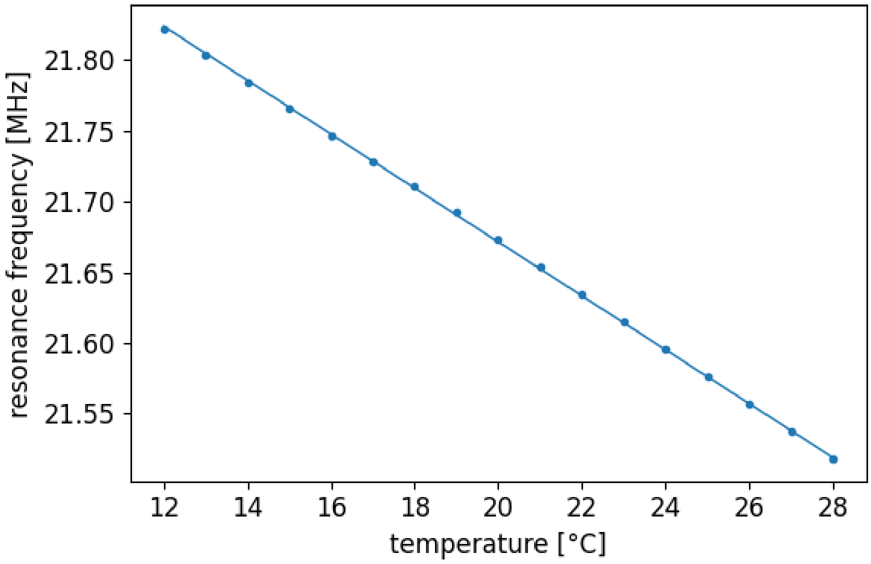

Figure 56: *NMR resonance frequency as a function of the temperature of the* 0.5 T *NMR magnet. The solid line is a linear least-squares fit that resulted in a temperature coefficient of* (-19.07 ± 0.06) kHz/°C.

A detailed treatment on NMR techniques can be found in [125].

7.4.2 Single Pulse Sequence

Many pulse sequences exist for NMR measurements. The most basic one is a single pulse to apply a $\pi/2$-flip. Additional pulses can be applied to refocus spins (e.g. a Hahn Echo [116], briefly described in Sec. 7.4.3) or to correct for other dephasing effects. Since we have a continuous flow of water through the NMR pick-up coil, only a single-pulse sequence as shown in Fig. 57 can be applied in practice. The water in this coil gets fully replaced within 2.4 ms at a flow velocity of 2.35 m/s. Therefore, there is no time to apply any further pulse to the same sample and measure the spin precession signal.

The pulse amplifier is only turned on when the deblanking signal has a logical high. The deblanking delay of 3 ms before the excitation pulse allows the amplifier to warm up. A pulse of 2.1 μs duration is then fired. The pulse time was optimized for a $\pi/2$-flip of the

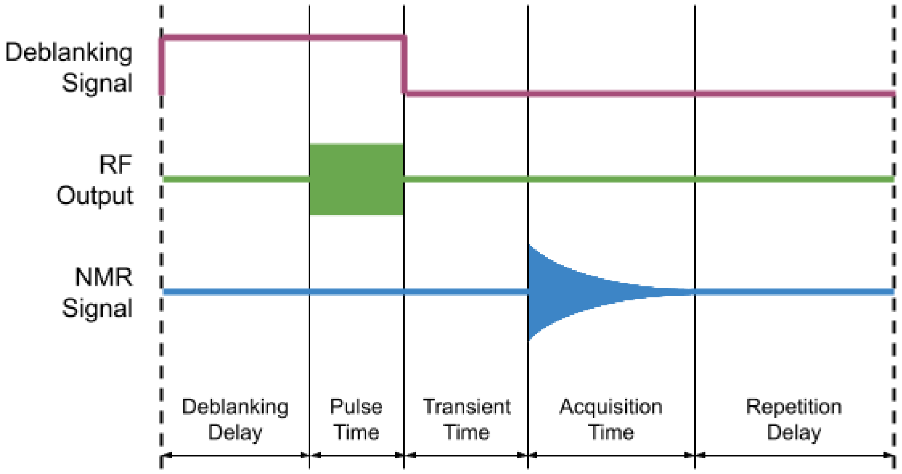

Figure 57: *Diagram of the NMR data acquisition for the single-pulse sequence. Detailed description in the text. The timeline is not to scale.*

proton spins as this leads to the highest signal amplitude. The amplifier is then blanked (turned off) and after a short transient delay of $40\ \mu\mathrm{s}$ that allows the system to subside from any remnant pulse signal, the receiver stage starts measuring the spin-precession signal, also called the free induction decay (FID), for $1\ \mathrm{ms}$. After the data acquisition, the system waits for the sample to be polarized again until the sequence is repeated. In a static sample, this repetition delay is about $5 \cdot T_1 \approx 12\ \mathrm{s}$, i.e., five time constants. In our case of a continuous water flow, the repetition delay of $2.5\ \mathrm{ms}$ was chosen such that all water that received the NMR pulse is flushed out of the pick-up coil. The total cycle length is approximately $6.5\ \mathrm{ms}$.

To improve the signal-to-noise ratio, the FID signals are averaged over many acquisitions, usually 1000 signals, before the spectral analysis is performed. Additionally, the phase of the pulse and the receiver are rotated by $90°$ for each acquisition. This way, imperfections of the two-phase detectors of the NMR system cancel out. This measurement sequence is called *CYCLOPS* phase cycling [125].

Figure 58 shows a high-statistic FID signal with a typical spectral width of $128\ \mathrm{kHz}$, resulting in a sampling interval of $7.8125\ \mu\mathrm{s}$. The signal is oscillating at $12.5\ \mathrm{kHz}$ which represents the difference between the pulse frequency of $21.68\ \mathrm{MHz}$ and the precession frequency of the protons. The reason for this is that the signal from the spin precession is digitally mixed with the reference signal from the oscillator that generates the pulse. The mixer produces an output that is the sum and the difference of the two signals. After a low-pass filter, only the signal of the difference remains. To get the real and imaginary part of the signal, the NMR system has actually two digital mixers. The precessing signal is fed into both but the reference signal is phase-shifted by $\pi/2$ in one of them. This allows quadrature

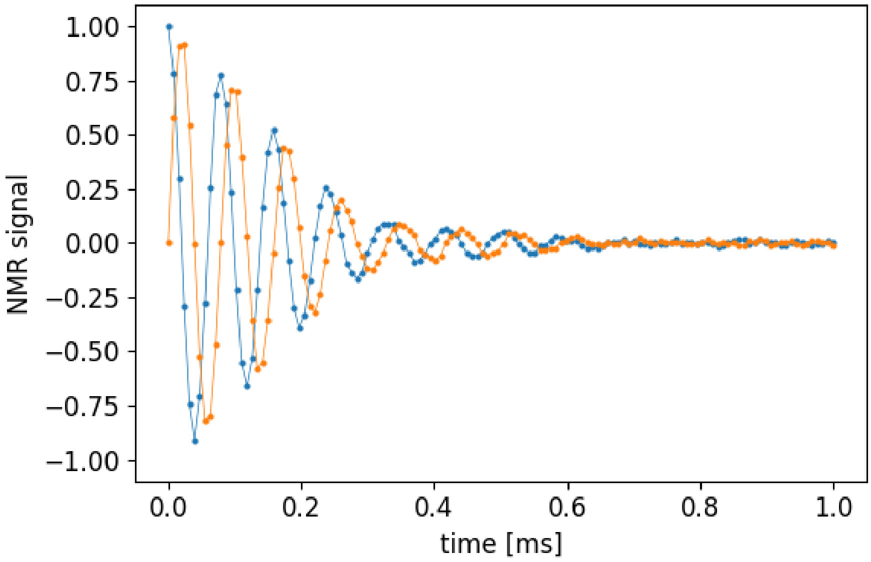

Figure 58: *High-statistic NMR signal, averaged over* 10000 *FID signals with a total measurement time of roughly* 65 *seconds. Shown is the real (blue) and the imaginary part (orange) of the signal amplitude as a function of time. The amplitude is normalized to one at* $t = 0$ s. *The exponential decay time of the signal is roughly* 179 μs. *The solid lines serve only as a guide for the eyes.*

detection to distinguish positive and negative frequencies without actually having two coils. A schematic of the electronics for the quadrature detection is shown in Fig. 59.

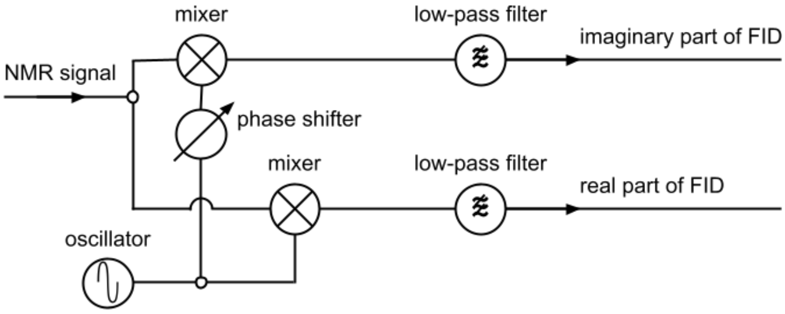

Figure 59: *Schematic of the electronics for the quadrature detection. The NMR signal is digitally mixed with the signal of the oscillator. This creates a signal that is the sum and the difference of the two. After a low-pass filter only the signal of the difference remains. To have a quadrature detection without actually having two pick-up coils, the NMR signal is additionally mixed with a second reference signal that is phase-shifted by* $\pi/2$.

The precession signal of the FID is usually analyzed in the frequency domain after performing a fast Fourier transform (FFT) [126]. Standard tools in signal processing are zero-padding and application of window functions. The former adds zeros at the end of the signal in the time domain. This results in a higher spectral resolution. It does not add information but rather interpolates between points that are already there and makes the spectrum look smoother. The latter damps parts of the signal with a lower signal amplitude. In the case of an FID, usually an exponential window is applied. We do not use either of them in our signal processing but fit the spectrum with a Lorentzian function

$$Sw \times \left(\frac{1}{1+(f-f_0)^2 \ w^2} - i \frac{(f-f_0) \ w}{1+(f-f_0)^2 \ w^2} \right) \times e^{-i\phi} + o \ , \tag{25}$$

where S is the signal amplitude, f_0 the resonance frequency, o the offset, and w the scale parameter that is connected to the observed transversal relaxation time constant $T_2^* = w/2\pi$. The real and imaginary part correspond to the absorption mode and the dispersion mode, respectively. The two can be mixed with the phase ϕ. Ideally, the phase ϕ is zero and the absorption and dispersion modes of the Lorentzian are not mixed. Drifts in the NMR electronics can lead to a change of ϕ. This changes the apparent spectral amplitude if only the absorption mode is considered, which leads to a systematic error. There are various methods to detect and correct this phase [127–129]. We bypass the problem of the signal phase correction by including it as a fit parameter. This makes the amplitude independent of the phase.

The NMR spectrum of the signal of Fig. 58 with a fitted Lorentzian of Eq. (25) is shown in Fig. 60. The fit revealed $S = (24.81 \pm 0.07)$ kHz, $f_0 = (12501 \pm 4)$ Hz, $w = (962 \pm 4)$ μs, $\phi = (-4.9 \pm 0.2)^\circ$, and $o = (0.115 \pm 0.006)$. The apparent amplitude in Fig. 60 is $Sw = 23.9 \pm 0.1$.

Depending on the measurement performed in the interaction zone, the spin polarization and therefore the signal amplitude may be low. To improve the fit of the spectrum we take a reference measurement before each measurement sequence. This measurement has the same parameters for the NMR pulse sequence, but all spin-flip signals in the interaction zone are turned off. This leads to a reference signal with the highest possible amplitude. The Lorentzian Eq. (25) is then fitted to the reference spectrum and the parameters f_0 and ϕ are fixed for the subsequent measurements. Additionally, the amplitude of the reference is used for normalization resulting in the *normalized spin polarization*.

The uncertainty of the data in the spectrum can be estimated by using the data points

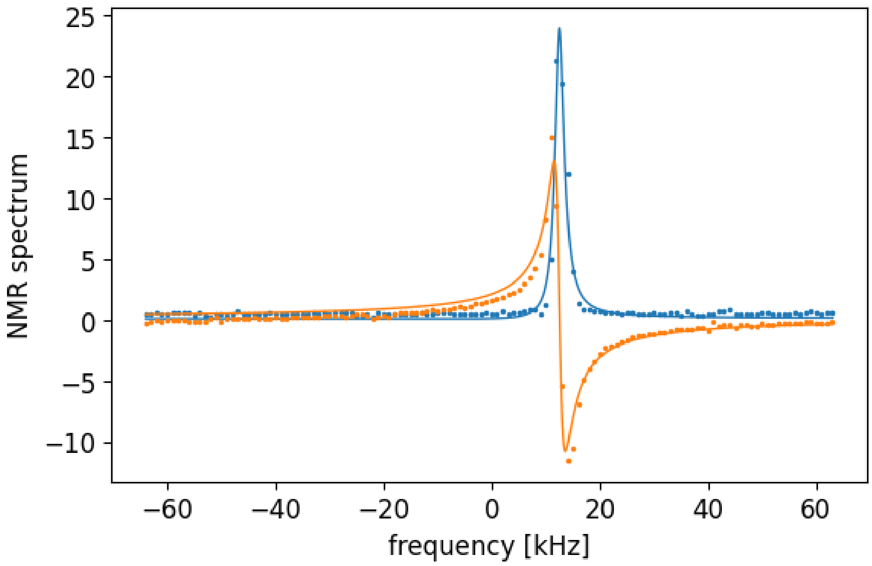

Figure 60: *Spectrum of the NMR signal of Fig. 58 that was calculated using an FFT algorithm. The spectral peak has the shape of a Lorentzian where real part (blue) is the absorption mode and the imaginary part (orange) the dispersion mode. The solid lines are a least-squares fit of Eq. (25). The absorption peak has a full width at half maximum (FWHM) of roughly* $2.2\ \mathrm{kHz}$.

in the baseline and calculating their standard deviation around the mean.[n] This uncertainty can then be provided to the fitting routine which includes it in the calculation of the errors of the fit parameters. Another possibility is to scale the fit parameters such that the reduced chi-squared $\chi_r^2 = 1$. In Fig. 60 it becomes evident, that Eq. (25) does not take into account all the characteristics of the NMR signal. This means that the model does not represent the data perfectly and $\chi_r^2 > 1$ by definition. The second option should therefore be avoided as this leads to a wrong estimate of the uncertainty of the fit parameters, so we use the first option.

7.4.3 Hahn Echo Pulse Sequence

For completeness we show the NMR signal of a Hahn echo sequence in Fig. 61. The scan parameters for the first pulse were the same as in the single pulse measurement presented in

---

[n] The baseline is the part of the spectrum where no signal is present, e.g., for all negative frequencies in the real part of the spectrum shown in Fig. 60.

Fig. 58. The $\pi/2$-pulse is followed by a second pulse to flip the spins by π after a time of $2\ \mathrm{ms}$. This leads to a refocusing of the spin polarization and the echo signal appears after another $2\ \mathrm{ms}$. Since the Hahn echo can only be applied on a static sample, we performed only 100 scans with a repetition delay of 12 seconds between each scan.

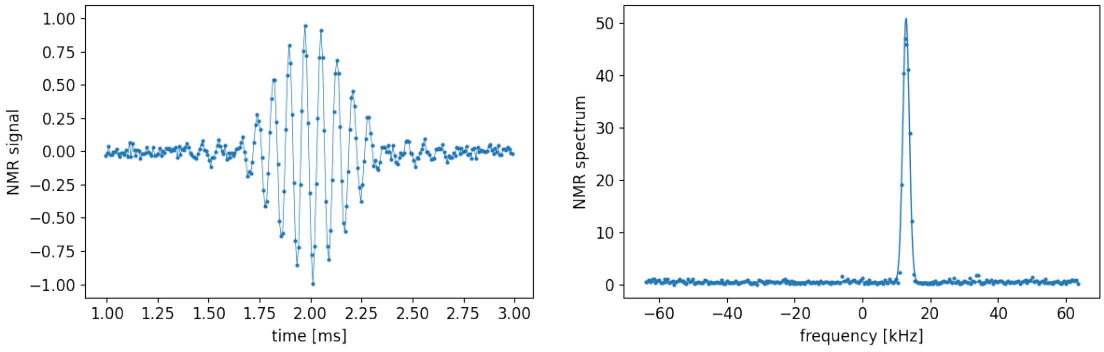

(a) (b)

Figure 61: *Measurement of a static water sample with the Hahn Echo pulse sequence. The signal was averaged over* 100 *echo signals with a total measurement time of roughly* 20 *minutes. (a) Real part of the normalized NMR signal. The imaginary part is phase shifted by* $\pi/2$ *but not shown. The solid lines serve only as a guide for the eyes. (b) Modulus of the spectrum fitted with a Gaussian of Eq. (26) (solid line). The resonance has a FWHM of roughly* $2.3\ \mathrm{kHz}$.

Since the real and imaginary part of the spectrum do not follow a simple shape as Eq. (25), it is reasonable to look at the modulus of the spectrum and fit a Gaussian

$$S \times e^{\frac{-(f-f_0)^2}{2\sigma^2}} + o \tag{26}$$

to the data, where S is the spectral amplitude, f_0 the resonance frequency, σ the width, and o the offset. The fit of the spectrum in Fig. 61b revealed $S = 50.4 \pm 0.2$, $f_0 = (12852 \pm 4)\ \mathrm{Hz}$, $\sigma = (961 \pm 4)\ \mathrm{Hz}$, and $o = 0.50 \pm 0.02$.

7.4.4 Longitudinal Spin Relaxation

An important property for the experiment is the longitudinal relaxation of the proton spins with time constant T_1, also called spin-lattice relaxation. It is the time that the spins need to (re-)align with the external magnetic field and the same as discussed in Sec. 7.2. For a static NMR sample it defines the time between two consecutive measurements as they require the spins to be fully polarized, i.e., the repetition delay. For our experiment with a continuous water flow it defines the maximum time between the polarization of the spins and the measurement of them. Together with the velocity of the water flow one can calculate the maximum possible length of the experiment.

T_1 can be measured by applying an *inversion recovery* pulse sequence on a static sample [111]. First the polarization is inverted by applying a π-pulse. Then the polarization can recover for a certain time. After this, an analyzing pulse sequence, e.g. single pulse or Hahn echo, is applied to measure the recovered polarization. The recovery time is scanned and a recovery function

$$P = P_0 \times \left(1 - 2e^{-t/T_1}\right) \tag{27}$$

fitted, where P_0 is the initial polarization.° The data with the least-squares fit of Eq. (27) of such a measurement is shown in Fig. 62. The fit revealed a time constant of $T_1 = (2.35 \pm 0.02)\ \mathrm{s}$ which is in agreement with the value of $T_1 = (2.33 \pm 0.07)\ \mathrm{s}$ that was measured by E. L. Hahn [111].

The maximum possible length of the experiment can be estimated for the usual water flow velocity of $2.35\ \mathrm{m/s}$ using $v \cdot T_1 \approx 5.5\ \mathrm{m}$. This is only an order of magnitude estimation and depends on other parameters such as the initial polarization or the sensitivity of the NMR detection system. Since T_1 is given by the water, the velocity could be increased to extend the maximum length of the experiment.

7.4.5 Transversal Spin Relaxation

The second important relaxation is the transversal relaxation or spin-spin relaxation with time constant T_2. It originates from the interaction between the spins in the NMR sample. Usually, the observed decay of the transversal polarization with time T_2^* is much faster because of inhomogeneities of the magnetic field. Nevertheless, with the proper pulse sequence, the natural T_2 can be measured [130]. Those sequences apply a pulse echo which is able to refocus the spins that are depolarized due to inhomogeneities but not due to the spin-spin interaction.

The mostly used sequence for the measurement of the spin-spin relaxation time is the *Carr-Purcell-Meiboom-Gill (CPMG)* pulse sequence [131, 132]. The spins of a static sample are first flipped into the transverse plane by a $\pi/2$-pulse. Then an equitemporal series of refocusing π-pulses is applied. The time between these pulses has to be short to minimize diffusion effects. Each of those pulses creates an echo with decreasing amplitude due to the

---

°The only difference to Eq. (24) is the factor of two, since here the polarization is fist inversed whereas in Eq. (24) the polarization was zero in the beginning.

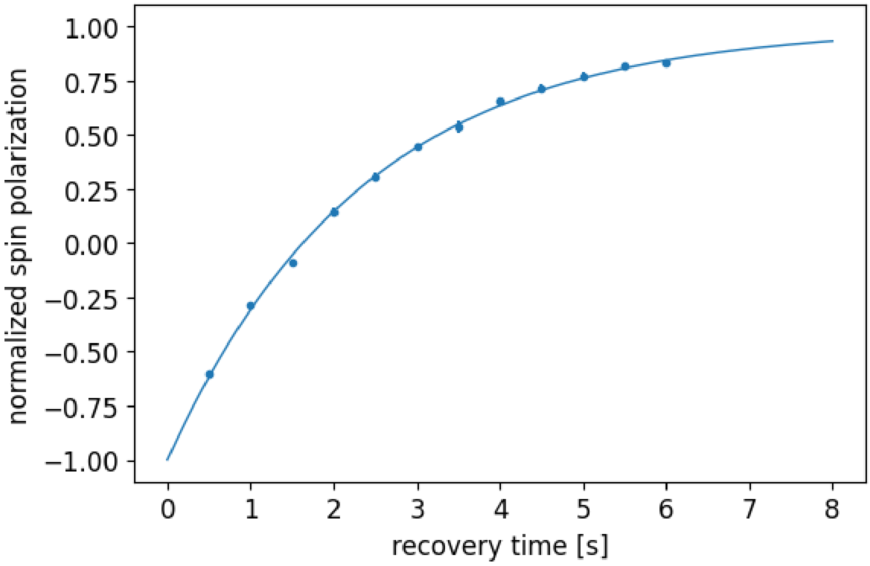

Figure 62: *Measurement of the longitudinal spin-lattice relaxation time* T_1*. Shown is the normalized spin polarization as a function of the recovery time. The solid line is a least-squares fit of Eq. (27) that revealed a time constant of* $T_1 = (2.35 \pm 0.02)$ s.

spin-spin relaxation. The echo amplitude as a function of the echo time can be fitted with an exponential function

$$P = P_0 \times 2e^{-t/T_2} + A \tag{28}$$

that gives the time constant T_2. The constant offset A is usually needed if the measurement is not perfectly on resonance [133]. The normalized measured data of a CPMG sequence with a fit of Eq. (28) that revealed $T_2 = (1.67 \pm 0.02)$ s and $A = 0.028 \pm 0.002$ is shown in Fig. 63.

The transversal relaxation that is observed in a FID signal as in Fig. 58 includes the contribution from the inhomogeneities of the magnetic field. In the spectrum it defines the linewidth of the resonance peak. Its time constant is called T_2^* and can be determined by fitting and an exponential function as Eq. (28) into the modulus of the FID. In our case, this led to an observed relaxation time constant of $T_2^* = (146 \pm 1)\ \mu$s.

The following formula holds for T_2^*, T_2, and the magnetic field inhomogeneities ΔB_{NMR} [130]:

$$\frac{1}{T_2^*} = \frac{\gamma_p \Delta B_{\text{NMR}}}{2} + \frac{1}{T_2} \tag{29}$$

$$\Longrightarrow \Delta B_{\text{NMR}} = \frac{2}{\gamma_p}\left(\frac{1}{T_2^*} - \frac{1}{T_2}\right) \approx \frac{2}{\gamma_p T_2^*}\ , \tag{30}$$

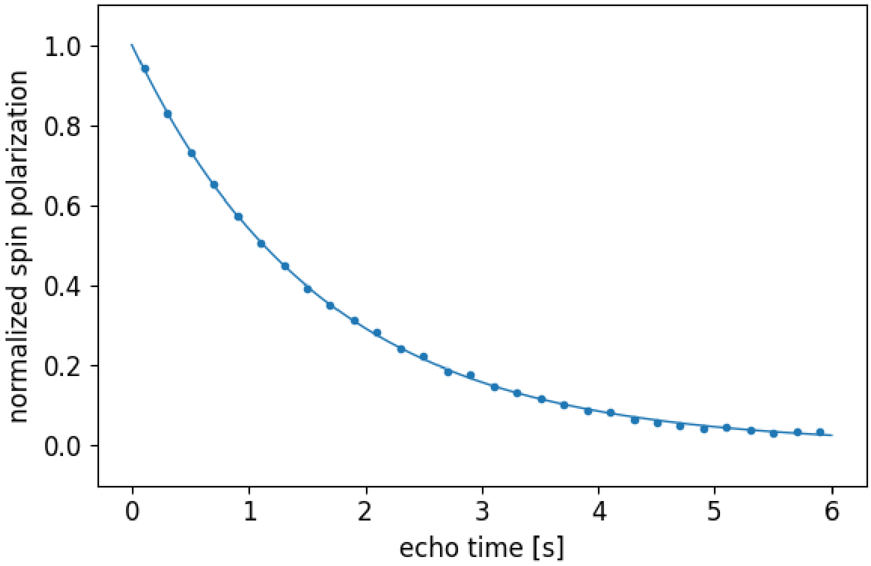

Figure 63: *Measurement of the transversal spin-spin relaxation time* T_2. *Shown is the normalized spin polarization as a function of the echo time. The solid line is a least-squares fit of Eq. (28) that resulted in a time constant of* $T_2 = (1.67 \pm 0.02)$ s.

where γ_p is the gyromagnetic ratio of the proton. We used Eq. (30) to calculate $\Delta B_{\mathrm{NMR}} = (51.2 \pm 0.5)\ \mu\mathrm{T}$ that corresponds to a relative uniformity of 10^{-4} for a field of $0.5\ \mathrm{T}$ as stated by the manufacturer for a $10\ \mathrm{mm}$ sample.

8 Rabi Measurements

The Rabi measurements are performed with a single spin-flip coil in the interaction zone. An oscillating current is applied to create the B_1 field that flips the spins if the frequency is close to the Larmor resonance frequency of the B_0 field. The B_1 field is linearly oscillating and orthogonal to B_0, in our case it is aligned with the direction of the water flow along the z-axis. If on resonance, the effective field that the protons see in their reference frame is along the B_1 axis which lets them precess around it. A more detailed explanation and a schematic can be found in Sec. 10.2 and Fig. 76, respectively. The amplitude of the signal is usually optimized such that it creates a π-flip, resulting in the highest resonance amplitude. We searched for the resonance at various B_0 fields and flow velocities. The current through the B_0-coil for the measurements shown in Fig. 64a was set to $50\ \mathrm{mA}$. This created a magnetic field of approximately $12\ \mu\mathrm{T}$ that corresponds to a resonance frequency of $500\ \mathrm{Hz}$. As the resonance width is proportional to the flow velocity, the resonance becomes broader for faster water flow velocities. Additionally, the amplitude of the resonance increases since the time for relaxation is shorter. The amplitude of the spin-flip field B_1 used for these

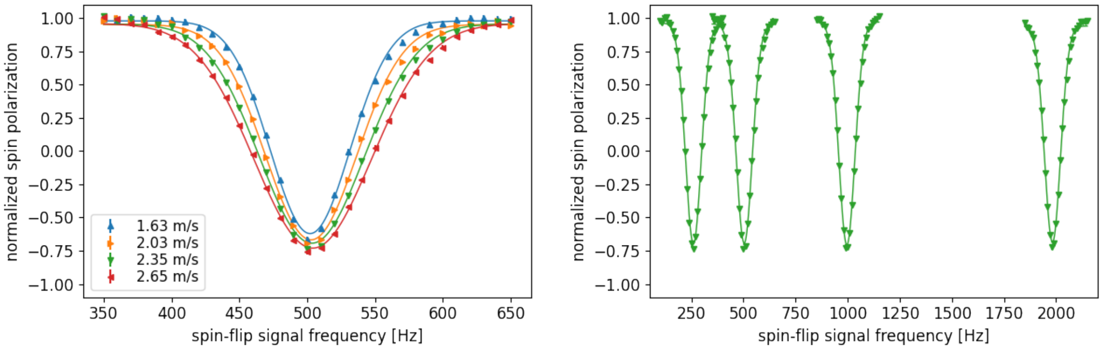

(a) (b)

Figure 64: *(a) Rabi resonances at* $B_0 \approx 12\ \mu\mathrm{T}$ *(*$500\ \mathrm{Hz}$*) for water flow velocities of* $1.63\ \mathrm{m/s}$ *(blue ▲),* $2.03\ \mathrm{m/s}$ *(orange ►),* $2.35\ \mathrm{m/s}$ *(green ▼), and* $2.65\ \mathrm{m/s}$ *(red ◄). The Gaussian fit of the data (solid lines) lead to a FWHM of* $(69.3\pm0.5)\ \mathrm{Hz}$, $(79.4\pm0.5)\ \mathrm{Hz}$, $(91.0\pm0.6)\ \mathrm{Hz}$, *and* $(101.6\pm0.6)\ \mathrm{Hz}$*, respectively. The width scales proportional to the velocity as expected. (b) Rabi resonances at a water flow velocity of* $2.35\ \mathrm{m/s}$ *for various* B_0 *fields, resulting in resonance frequencies at* $250\ \mathrm{Hz}$, $500\ \mathrm{Hz}$, $1000\ \mathrm{Hz}$, *and* $2000\ \mathrm{Hz}$*. More values of* B_0 *up to a resonance frequency of* $10\ \mathrm{kHz}$ *were tested but not shown here for reasons of legibility.*

measurements was optimized for each velocity for the highest resonance amplitude.

For the measurements shown in Fig. 64b, the water flow velocity was fixed at $2.35\ \mathrm{m/s}$. We measured the Rabi resonance for various values of the B_0 field resulting in resonance frequencies between $250\ \mathrm{Hz}$ and $10\ \mathrm{kHz}$. Only four of them are shown. The FWHM of $(90.8 \pm 0.4)\ \mathrm{Hz}$ is the same for all resonances within the uncertainty. The measured width deviates from the theoretical value of $125\ \mathrm{Hz}$ when calculating the FWHM using the Rabi formula [79]. This can be explained by the fringe field of the spin-flip coil and leads to an effective length of the coil of $20\ \mathrm{mm}$, compared to the geometric length of $15\ \mathrm{mm}$.

To optimize the amplitude of the spin-flip signal for a π-flip, we scanned the amplitude B_1 on resonance. A π-flip is achieved when the polarization is at the first minimum in Fig. 65 at a value of the spin-flip signal amplitude between $300\ \mathrm{mV_{pp}}$ and $500\ \mathrm{mV_{pp}}$. Figure 65 also shows that a higher field amplitude is needed to achieve the same flipping angle if the water flows faster.

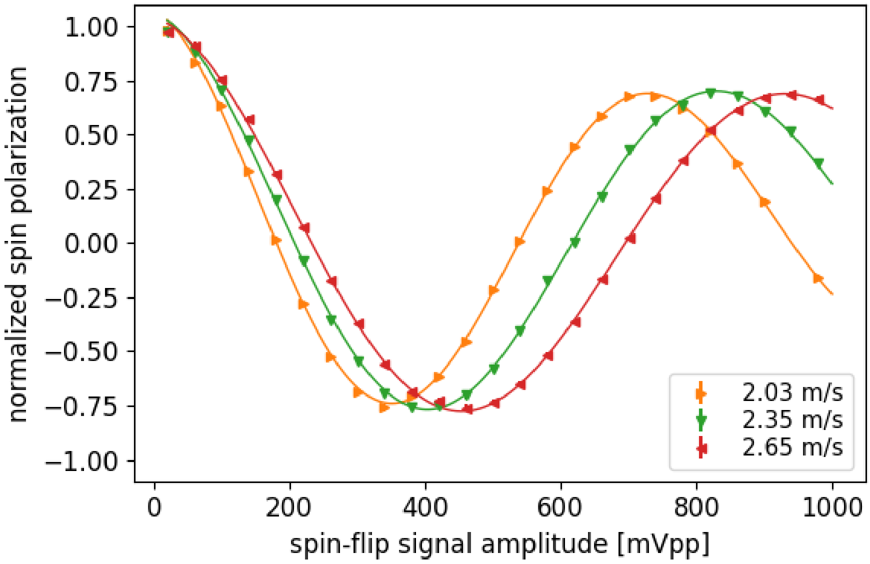

Figure 65: *Rabi amplitude scan on resonance at* $B_0 \approx 12\ \mu\mathrm{T}$ $(500\ \mathrm{Hz})$ *with the same velocities and colors as in Fig. 64a. The data are fitted with the convolution of a sinusoidal function with an exponential decay (solid lines). The fitted period of the sinusoidal can be used to calculate the required amplitude for the desired flipping angle.*

9 Ramsey Interferometry

A typical measurement that can be performed with two spin-flip coils in the interaction zone is the Ramsey measurement [56, 57]. In this type of measurement, the spins are first flipped by $\pi/2$. Then, they precess freely before they are flipped again by $\pi/2$. The two spin-flip signals are phase-locked and running at the same frequency. If this frequency is scanned over the resonance, a typical Ramsey pattern as shown in Fig. 66 is obtained. As described in Sec. 7.3, we placed the two spin-flip coils with a center-to-center separation of $600\ \mathrm{mm}$.

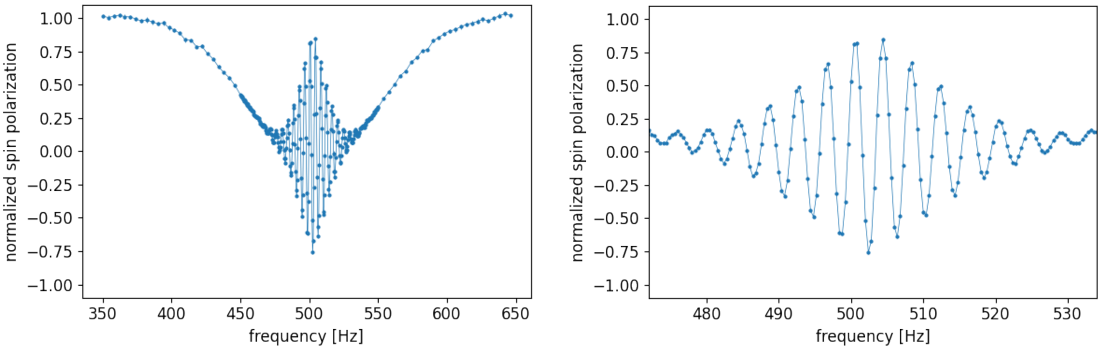

Figure 66: *Typical resonance pattern obtained with Ramsey's method of separated oscillatory fields at a magnetic field of* $B_0 \approx 12\ \mu\mathrm{T}$*. The average velocity of the water was* $2.35\ \mathrm{m/s}$*. The right figure shows a zoom in the central frequency range. The fringe period is approximately* $4\ \mathrm{Hz}$*. The measurement time per point was roughly* $18\ \mathrm{s}$ *and the total measurement time* $1\ \mathrm{h}\ 30\ \mathrm{min}$*. The solid lines serve only as a guide for the eyes.*

The overall envelope arises from the single-spin-flip resonance. The fringes in the central region are the Ramsey interference pattern of the two spin-flip coils. The fringe period decreases with a longer interaction distance between the spin-flip coils, making the experiment more sensitive. The visibility of the fringes above and below the resonance frequency is reduced due to mixing of protons with different velocities. In case of all protons having the same velocity, all fringes would reach the maximum normalized spin polarization of one.

Another option for a Ramsey-type measurement is to keep the frequency of both spin-flip signals fixed on resonance but scan the relative phase between the two oscillating signals. This has the advantage of always being on resonance and obtaining data in the shape of a simple sinusoidal curve that can be fitted easily. The signal of such a phase scan is shown in Fig. 67.

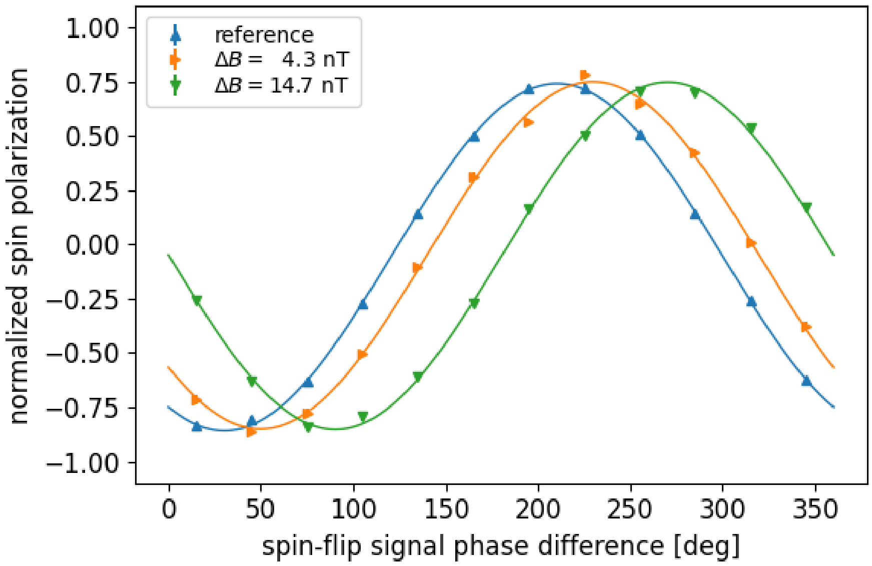

Figure 67: *Ramsey phase scan on resonance at* $500\ \mathrm{Hz}$, *corresponding to a magnetic field of* $B_0 \approx 12\ \mu\mathrm{T}$. *Shown is the normalized spin polarization as a function of the phase between the two spin-flip signals. The water flow velocity was* $2.35\ \mathrm{m/s}$. *To test functionality of the setup and the method, we performed a reference measurement (blue) and changed the magnetic field slightly to see the change in phase (orange and green). The data are fitted with sinusoidal functions with a fixed period of* $360°$ *(solid lines). The measurement time per phase scan is roughly* $2\ \mathrm{min}$.

Ramsey's technique is very sensitive to (pseudo-)magnetic field effects. A tiny change in the main magnetic field ΔB results in a change of the phase that the protons acquire during the precession in the interaction region

$$\Delta\varphi = \gamma_p \Delta B \frac{L_{\text{eff}}}{v} \ , \tag{31}$$

where L_{eff} is the effective interaction length [78] and v is the water flow velocity.[p] This is visible in Fig. 67 where we changed the magnetic field by $(4.3 \pm 0.3)\ \mathrm{nT}$ and $(14.7 \pm 0.3)\ \mathrm{nT}$. This values were measured with the fluxgate after the second spin-flip coil. The average field between the spin-flip coils might be slightly different. These values for the magnetic field change resulted in a phase shift of $19.5° \pm 0.4°$ and $60.0° \pm 0.4°$, respectively. This agrees,

---

[p] The effective interaction length is slightly longer than the separation of the spin-flip coils. The reason is, that the spins start already to precess within the spin-flip coil when partially flipped.

within the limits of uncertainty, with the theoretical values that can be calculated using Eq. (31).

To get the phase shift as a function of the magnetic field change we performed several more measurements. A linear fit through the data resulted in a value of $\Delta\varphi/\Delta B = (4.1 \pm 0.1)$ °/nT as presented in Fig. 68.

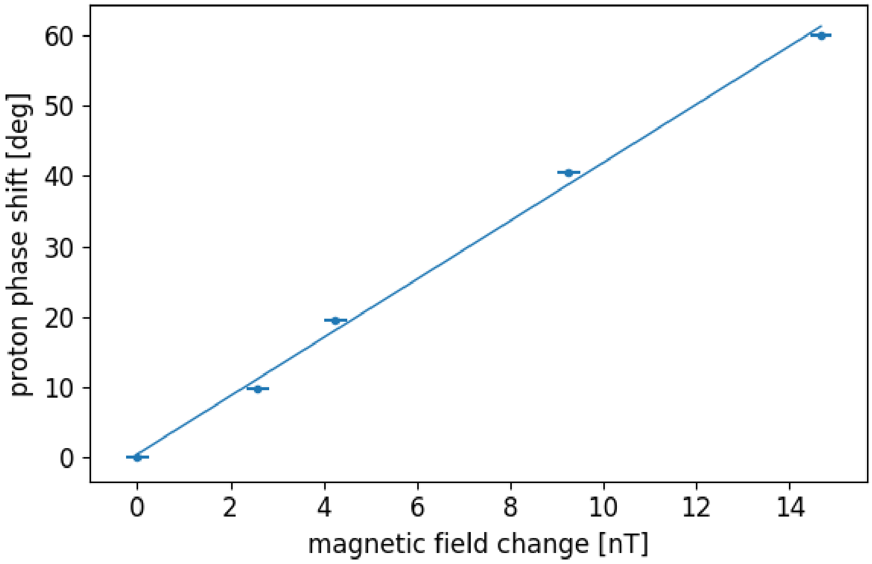

Figure 68: *Measured phase shift $\Delta\varphi$ as a function of the magnetic field change ΔB. The settings were the same as in Fig. 67. The linear fit (solid line) resulted in a value of* $\Delta\varphi/\Delta B = (4.1 \pm 0.1)$ °/nT.

The sensitivity of the full apparatus is defined by the precision of the phase determination and the stability of the field. To characterize the stability, we performed phase scans as shown in Fig. 67 over 60 hours with the end caps of the mu-metal shield opened and closed in two consecutive measurement sequences. The stability was then analyzed by calculating the overlapping Allan deviation [134, 135] shown in Fig. 69.

Both show a minimum in the Allan standard deviation at about 30 minutes. The open shield has minimum of $0.43°$ (105 pT) and the full shield of $0.34°$ (83 pT). This implies, that after 30 minutes, a new reference measurement has to be taken. If the setup has to be changed, e.g. a polarity change in the magnetic field to account for systematic effects, this should be done within that time frame.

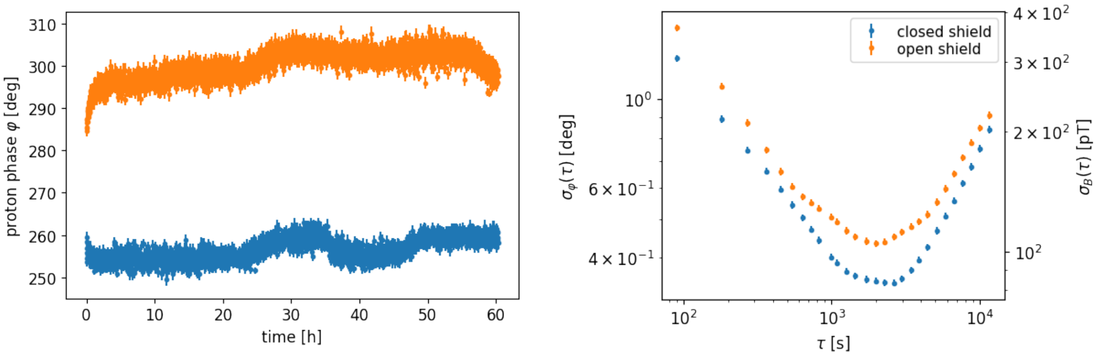

(a)

(b)

Figure 69: *Proton phase stability for a setup with the end caps of the mu-metal shield closed (blue) and opened (orange). (a) Time series of the two consecutive measurements. (b) Overlapping Allan deviation of the phase as a function of the observation time. The vertical axis on the right side shows the corresponding magnetic field stability using the conversion factor of the linear fit in Fig. 68.*

10 Bloch-Siegert Shift

In a Rabi resonance measurement with a single spin-flip coil, an oscillating field at the Larmor frequency $\omega_0 = -\gamma_p B_0$ is applied to flip the spin of a particle. For technical reasons, the applied field is usually linearly oscillating and of the form $B_{\mathrm{rf}} = 2B_1 \cos(\omega_{\mathrm{rf}} t)$. The amplitude of the oscillating flipping field is often represented in the form of $\omega_1 = -\gamma_p B_1$ which is called the Rabi frequency.

In a mathematical description, this field can be regarded as the sum of two rotating fields, one of them rotating clockwise and the other anti-clockwise with frequencies $\pm\omega_{\mathrm{rf}}$. To calculate the effective field around which the spins are precessing, a transformation in the local frame of the particle's spin is performed. After this, one of the fields is rotating slow with $\omega_{\mathrm{rf}} - \omega_0$ and the other is rotating fast with $\omega_{\mathrm{rf}} + \omega_0$. In the rotating-wave approximation, the fast rotating field is neglected. An argument for this is that the time scale of the counter rotating field is to fast for the relevant transitions and averages to zero. The approximation holds under the assumption of being close to resonance ($\omega_{\mathrm{rf}} \simeq \omega_0$) and having a low oscillating field intensity.

In Sec. 10.1 we describe the measurement of the Bloch-Siegert shift in a Rabi-type setup with a single spin-flip coil. We then show, how the shift can be compensated and enhanced by inducing a second oscillating signal with the proper choice of frequency and amplitude. We further explain the Bloch-Siegert shift in a Ramsey-type setup in Sec. 10.2. We show that the phase pick-up due to a slightly off-resonance flipping field can be used to compensate the shift in such a setup.

10.1 Bloch-Siegert Shift in a Rabi-type Setup

The Bloch-Siegert shift is a well-known effect of the counter-rotating field [136]. It is a shift of the resonance frequency, that depends on the amplitude of the oscillating field and in the first order is

$$\delta_{\mathrm{BS}}^{\mathrm{Rabi}} \approx \frac{1}{4}\frac{(\gamma B_1)^2}{\gamma B_0} = \frac{1}{4}\frac{\omega_1^2}{\omega_0}\ , \tag{32}$$

Figure 70 shows the Rabi resonances for various values of the spin-flip signal amplitude. The amplitude of the resonance depends on the flipping angle that is different for all the signal amplitudes. For higher signal amplitudes, the resonance is shifted to higher frequencies. The shift of the resonance frequency for two settings of ω_0 is shown in Fig. 71.

The values of the curvature from the quadratic fit are $(31 \pm 2)\ \mathrm{Hz/V_{pp}^2}$ and $(17.1 \pm$

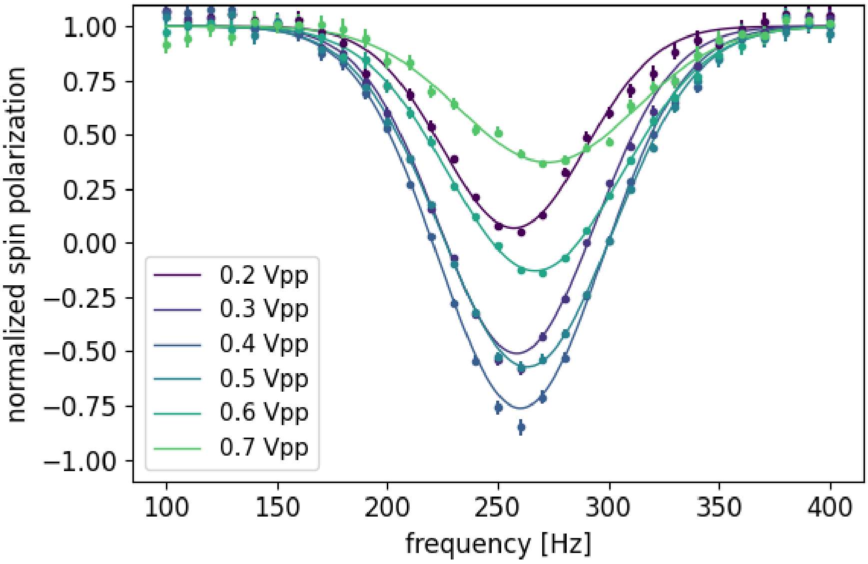

Figure 70: *Rabi resonances at* $\omega_0 = 2\pi \times 250$ Hz *for six amplitudes of the oscillating field* B_1. *Shown is the normalized spin polarization as a function of the oscillation frequency of the spin-flip signal. The resonance frequency shifts to higher values with increasing field amplitude as predicted by Eq. 32.*

$0.8)\ \mathrm{Hz/V_{pp}^2}$ for the resonance frequencies of (251.8 ± 0.3) Hz and (499.7 ± 0.1) Hz, respectively. The resonance frequencies were determined by the fitted offset of the quadratic function and are subtracted from the data in Fig. 71 to make the measurements comparable. The curvatures can not be directly compared with Eq. (32) since the corresponding B_1 fields are unknown but the two values are in agreement with each other since they scale linearly with ω_0.

The Bloch-Siegert shift can lead to a systematic effect in measurements that use a resonance method like the Rabi or Ramsey method. It was pointed out by G. L. Greene and N. F. Ramsey [137], that the Bloch-Siegert shift can be eliminated by applying a second oscillating signal at the right frequency and amplitude. This can be done with the power combiners explained in Sec. 7.3 and schematically shown in Fig. 52. The Bloch-Siegert shift after adding this compensation signal has the following form

$$\delta_{\mathrm{BS}}^{\mathrm{Rabi}} = \frac{1}{2}\left(\frac{\omega_1^2}{2\omega_0} + \frac{(a\omega_1)^2}{\omega_0(1-b)} + \frac{(a\omega_1)^2}{\omega_0(1+b)}\right) \tag{33}$$

$$= \frac{1}{4}\frac{\omega_1^2}{\omega_0}\left(1 - \frac{4a^2}{b^2-1}\right) . \tag{34}$$

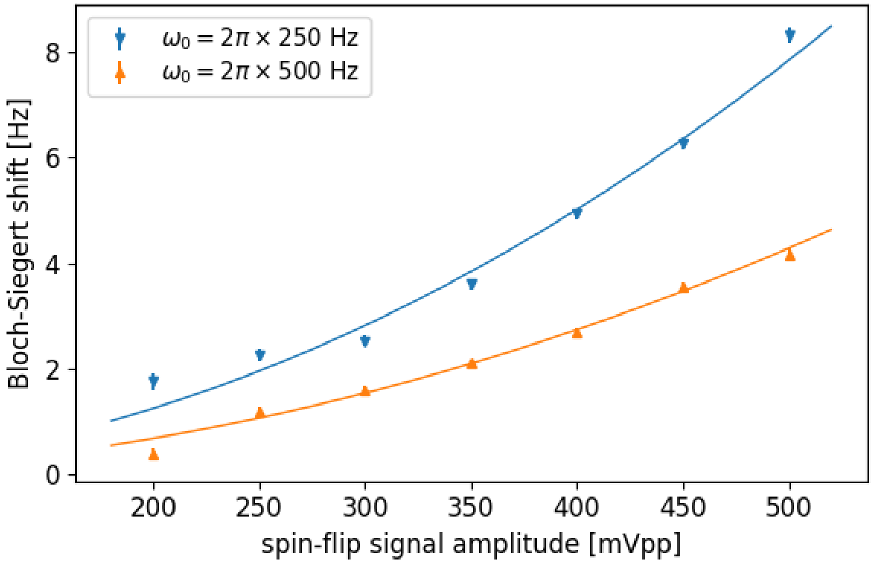

Figure 71: *Bloch-Siegert shift for the two resonance frequencies at roughly* $\omega_0 = 2\pi \times 250$ Hz *(blue ▼) and* $\omega_0 = 2\pi \times 500$ Hz *(orange ▲). The shift of the resonance frequency is shown as a function of the applied spin-flip signal amplitude. The solid lines correspond to a quadratic fits where the linear term is fixed to zero. The fitted offset corresponds to resonance frequency without the Bloch-Siegert shift and is subtracted from the data.*

The first term in Eq. (33) is the regular Bloch-Siegert shift. The other two terms correspond to the rotating and counter-rotating field of the compensation signal where a is the fractional amplitude factor and b the fractional frequency factor. This means that the second oscillating signal is applied with the amplitude $a \cdot B_1$ at a frequency of $b \cdot \omega_{\mathrm{rf}}$. In the simplified form of Eq. (34) it becomes evident that the shift is compensated if

$$\frac{4a^2}{b^2 - 1} = 1 \; . \tag{35}$$

One example of a choice that fulfills the condition of Eq. (35) is $b = 4$ and $a = \sqrt{15}/2$. In principle any combination that fulfills condition Eq. (35) is possible with the constraint that the compensation frequency has to be far enough off-resonance to not directly flip the spins.

The same argument can also be applied to enhance the shift in the resonance frequency. With a choice of, e.g., $b = 0.5$ and $a = \sqrt{0.75}/2$, the shift gets doubled. We measured those two cases, together with regular Bloch-Siegert shift at $\omega_0 = 2\pi \times 500$ Hz.

Figure 72 shows that the enhancement and compensation indeed work. The values of the curvature from the quadratic fit are (18.6 ± 0.7) Hz/V$_{\mathrm{pp}}^2$ (standard), (3.7 ± 0.5) Hz/V$_{\mathrm{pp}}^2$

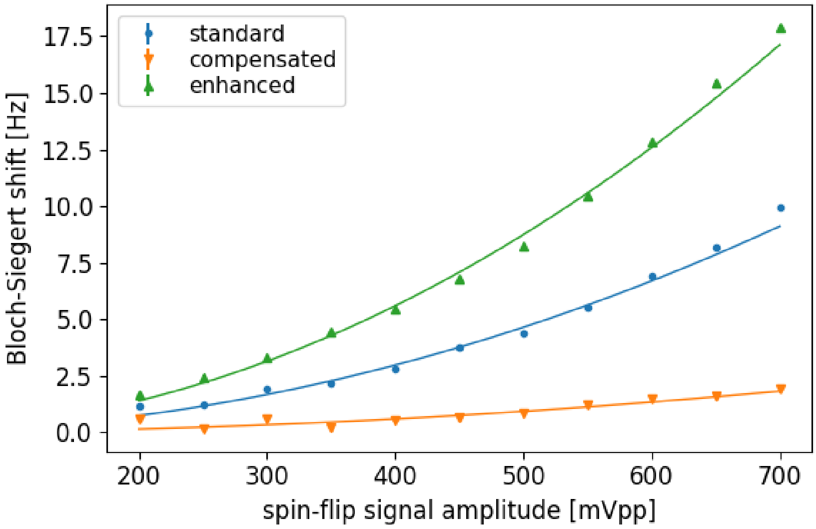

Figure 72: *Bloch-Siegert shift at* $\omega_0 = 2\pi \times 500$ Hz *without compensation (blue ●), partially compensated (orange ▼), and enhanced (green ▲). Shown is the shift of the resonance frequency as a function of the amplitude of the oscillating spin-flip signal. The solid lines correspond to quadratic least-squares fits where the linear term is fixed to zero.*

(compensated), and $(35 \pm 1)\ \mathrm{Hz}/\mathrm{V}_{\mathrm{pp}}^2$ (enhanced). However, the chosen parameters for the compensation did not fully eliminate the Bloch-Siegert shift. We tested other combinations of parameters but they did not compensate fully as well.

To find the parameters for a full compensation we fixed a value of a and scanned b around the theoretical value of the compensation. For each of combination of a and b we measured the resonance frequency for each spin-flip signal amplitude and fitted a quadratic function. The curvature of the quadratic fit as function of b for $a = 4$ is shown in Fig. 73. The root of the quadratic fit results in a value of $b = 7.3 \pm 0.2$ for a full compensation which is about 10% off from the predicted value, indicated by the orange point in Fig. 73.

To investigate this issue further, we performed the same measurement for various values of ω_0. Figure 74 shows that the deviation from the predicted value increases with higher resonance frequency ω_0. The extrapolation to $\omega_0 = 0$ leads to a value of $b = 8.0 \pm 0.2$ which is in good agreement with the prediction of $b = \sqrt{65} \approx 8.1$ from Eq. (35).

Those data suggest, that there is another term that shifts the resonance frequency, which is proportional to ω_0. Yet, we are not sure if this term belongs to the Bloch-Siegert shift itself or has a different origin. Higher order terms of the Bloch-Siegert shift are not a reasonable explanation since they are suppressed by ω_0. For example, the next-to-leading-order term is $\propto 1/\omega_0^3$.

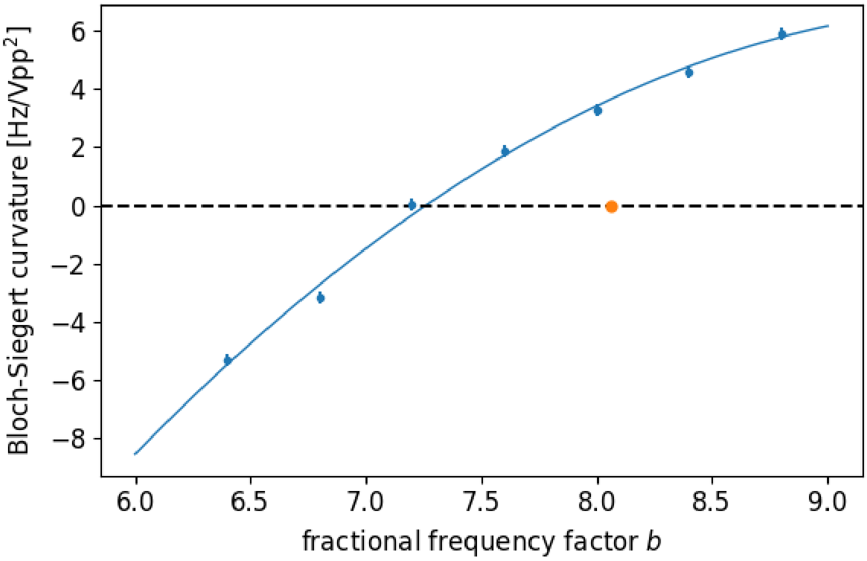

Figure 73: *Scan of the fractional frequency factor* b *to compensate for the Bloch-Siegert shift at* $\omega_0 = 2\pi \times 500\ \mathrm{Hz}$. *Shown is the curvature of the Bloch-Siegert shift as a function of* b *for a fractional amplitude factor of* $a = 4$. *The solid line corresponds to a quadratic fit, the dashed line indicates zero curvature, and the orange point to the theoretical value according to Eq. (35).*

We also searched for the fractional frequency factor b that cancels the Bloch-Siegert shift at the same resonance frequency $\omega_0 = 2\pi \times 500\ \mathrm{Hz}$ for various fractional amplitude factors a. The data are presented in Fig. 75. To compare the measurement with the model we also plotted the curve of Eq. (35) in Fig. 75 together with a linear fit through the data. It shows that the model and the measurement are in better agreement for lower values of a but diverge for higher ones. Additionally, all the measured value are below the theoretical curve.

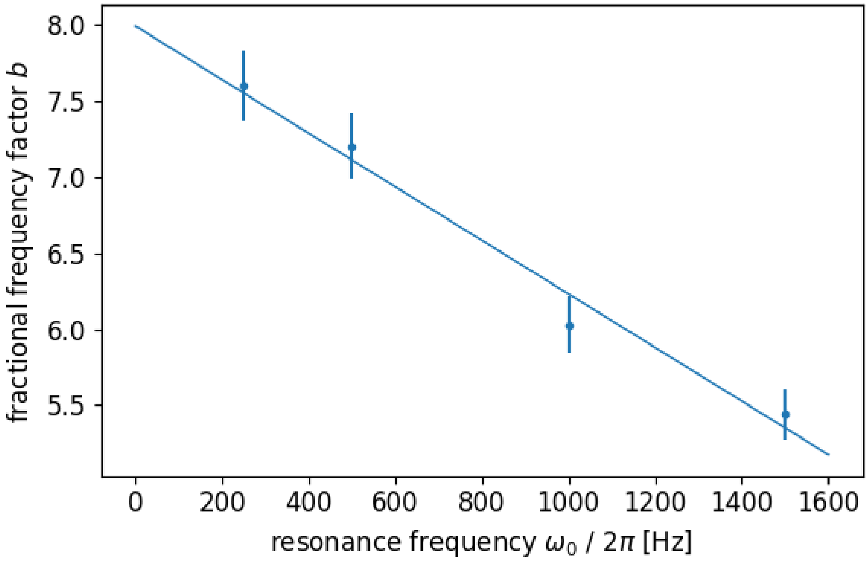

Figure 74: *Optimized fractional frequency factor* b *that cancels the Bloch-Siegert shift with a fractional amplitude factor of* $a = 4$ *for various values of* ω_0. *The solid line corresponds to a linear fit.*

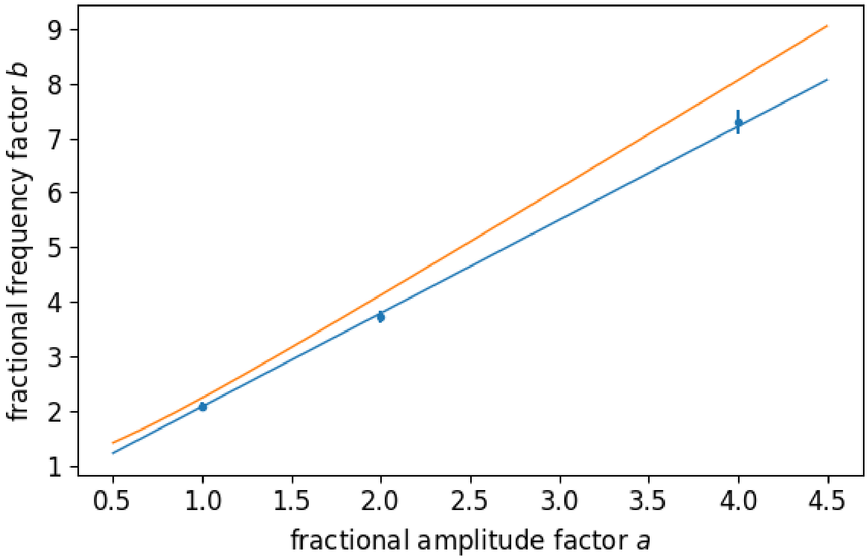

Figure 75: *Optimized fractional frequency factor* b *at* $\omega_0 = 2\pi \times 500\ \mathrm{Hz}$ *for various fractional amplitude factors* a *(blue dots). The blue line corresponds to a linear fit through the data and the orange line to the theoretical curve according to Eq. (35).*

10.2 Bloch-Siegert Shift in a Ramsey-type Setup

The shift of the resonance frequency in a Rabi-type setup with a single spin-flip coil leads to a shift of the Ramsey pattern of Fig. 66 and Fig. 67. The first-order shift of the resonance frequency in a Ramsey-type setup [137, 138] takes the form of

$$\delta_{\mathrm{BS}}^{\mathrm{Ramsey}} = \frac{l_{\mathrm{sf}}}{l_{\mathrm{int}}} \frac{\tan(\chi)}{\chi + \frac{2l_{\mathrm{sf}}}{l_{\mathrm{int}}}\tan(\chi)} \times \delta_{\mathrm{BS}}^{\mathrm{Rabi}}, \tag{36}$$

where

$$\chi = \frac{\tau}{2}\sqrt{\left((\omega_0 + \delta_{\mathrm{BS}}^{\mathrm{Rabi}}) - \omega_{\mathrm{rf}}\right)^2 + (\gamma B_1)^2}\ . \tag{37}$$

In the above equations l_{sf} is the length of the spin-flip coils, l_{int} the distance between the spin-flip coils, and $\tau = l_{\mathrm{sf}}/v$ the interaction time with the spin-flip signal.

We can calculate the Bloch-Siegert shift in a Ramsey-type setup with typical measurement parameters $\omega_0 = \omega_{\mathrm{rf}} = 2\pi \times 990\ \mathrm{Hz}$, $v = 2.35\ \mathrm{m/s}$, $l_{\mathrm{int}} = 0.58\ \mathrm{m}$, and $l_{\mathrm{sf}} = 0.02\ \mathrm{m}$.[q] We chose the amplitude $B_1 = \frac{\gamma\pi v}{2l_{\mathrm{sf}}}$ such that the spins are flipped by $\pi/2$. This results in a shift of $\delta_{\mathrm{BS}}^{\mathrm{Ramsey}} \approx 55\ \mathrm{mHz}$ that corresponds to approximately $5°$ in a Ramsey phase scan.

Compared to a Rabi-type setup, there is the additional free parameter ω_{rf}. Usually, ω_{rf} is set to the resonance frequency ω_0 and the spins are flipped around the axis of the B_1 field. If $\omega_{\mathrm{rf}} \neq \omega_0$, the effective field B_{eff} that the spins see in their laboratory frame is rotated away from the B_1 axis due to the off-resonance field $\Delta B = (\omega_0 - \omega_{\mathrm{rf}})/\gamma$. This leads to an additional phase that the spins acquire during their rotation. This behaviour is schematically presented in Fig. 76.

The phase pick-up due to the off-resonance field can be calculated by applying a rotation of angle $\pi/2$ around the axis of the effective field to a spin vector oriented along z. The movement or path of the spin for such a rotation is indicated by the dashed lines in Fig. 76b. A reasonable choice is $\omega_0 - \omega_{\mathrm{rf}} = 2\pi \times 1.4\ \mathrm{Hz}$ as this corresponds to half the difference of the measured resonance frequencies of the first and second spin-flip signals of $(991.6 \pm 0.2)\ \mathrm{Hz}$ and $(988.8 \pm 0.1)\ \mathrm{Hz}$, respectively. A rotation of angle α around an arbitrary unit vector $\hat{\vec{n}}$ can be described by the rotation matrix

$$\left[R_{\hat{\vec{n}}}(\alpha)\right]_{ij} = \Big(1 - \cos(\alpha)\Big) n_j n_j + \cos(\alpha)\delta_{ij} + \sin(\alpha)\epsilon_{ijk} n_k\ , \tag{38}$$

where δ_{ij} is the Kronecker delta and ϵ_{ijk} is the Levi-Civita symbol. In our case we apply the rotation $R_{\hat{\vec{B}}_{\mathrm{eff}}}(\pi/2)$ on the initial spin along the z-axis $\vec{s} = (0, 0, 1)$. The phase with respect

---

[q] We use the effective spin-flip coil length calculated in Sec. 8.

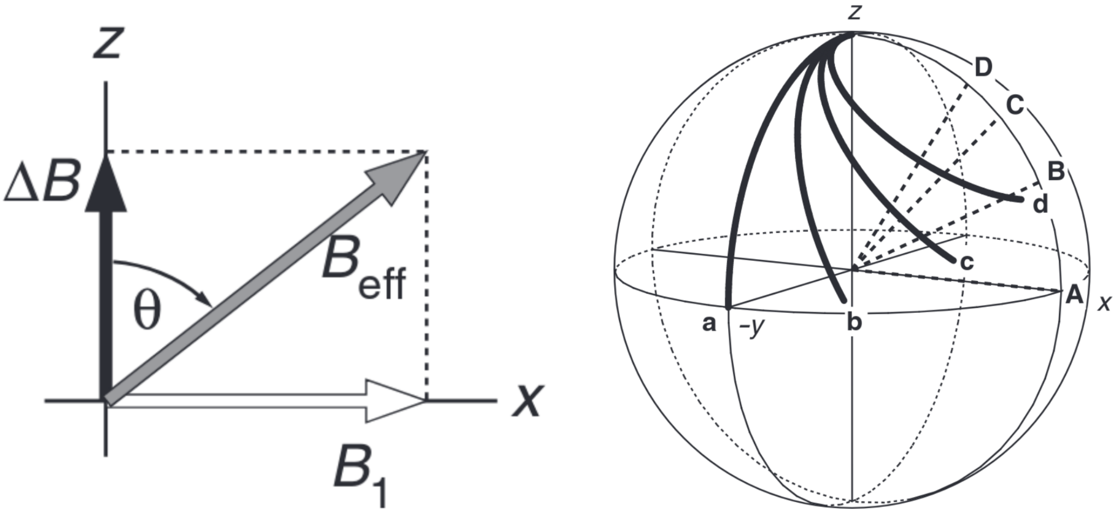

(a)

(b)

Figure 76: *(a) Schematic of the effective field axis around which the spins are rotated in their laboratory frame.* $\Delta B = (\omega_0 - \omega_{\mathrm{rf}})\,/\,\gamma$ *is the off-resonance field. (b) Schematic of the path (solid black lines) that the spins follow when flipped in their laboratory frame. The path* ***a*** *corresponds to the on-resonance case where the effective field lies along the dashed axis* ***A****. The other paths* ***b****,* ***c****, and* ***d*** *correspond to off-resonance fields of various offsets with effective fields along* ***B****,* ***C****, and* ***D****. The schematics are Figs. 3.10 and 3.25 in the lecture notes of J. Keeler in 2002 [125].*

to the y-axis can then be calculated by

$$\delta\varphi = \arctan(\vec{s}_x/\vec{s}_y) \ , \tag{39}$$

where $\vec{s}_x$ and $\vec{s}_y$ are the x and y components of the spin after the rotation, respectively. This results in $\delta\varphi \approx 2.5°$. A more detailed derivation of this off-resonance phase pick-up can be found in Appendix A.2.

The phase shifts due to the Bloch-Siegert effect and the off-resonance phase pick-up are on the same order of magnitude. A reasonable measurement of the Bloch-Siegert shift is therefore only possible, if the off-resonance effect is under control. To achieve this, the resonance frequencies at both spin-flip coils have to be known, stable, and the same frequency. This can be achieved by a better magnetic shielding and by adding a trimming field around the spin-flip coils shown in Fig. 51 to shift the resonances to the same frequencies.

We measured the effect of the off-resonance phase shift. For various ω_{rf} we scanned the amplitude of the spin-flip signal. For each amplitude we performed a Ramsey phase scan.

The data with a fits of the function $ax^4 + c$, where we call a the curvature, are shown in Fig. 77. Please note that those measurement include the phase shift due to the Bloch-Siegert and the off-resonance effect.

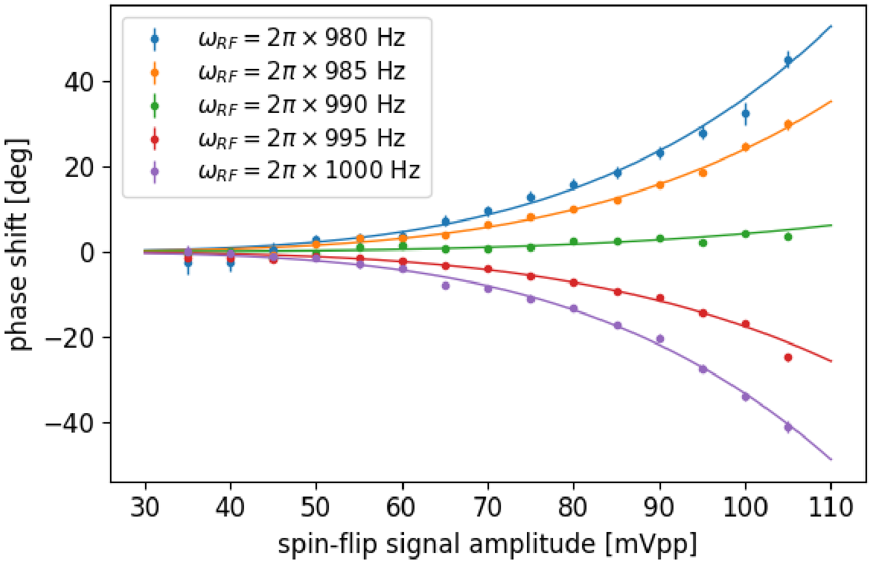

Figure 77: *Measurement of the off-resonance phase shift as a function of the spin-flip signal amplitude for various ω_{rf} (color labels in legend). The resulting phase shifts also include the Bloch-Siegert shift. The data are fitted with the function $ax^4 + c$ (solid lines), where we call a the curvature. The fitted offset c is subtracted from the data.*

The measurements show that the off-resonance phase shift can cancel the Bloch-Siegert shift if the spin-flip signal frequency is chosen such that the curvature is zero. Figure 78 shows the curvature a as a function of the spin-flip signal frequency with a linear fit that provides a root at $\omega_{\mathrm{rf}} = (990.9 \pm 0.1)$ Hz.

Only if the true resonance is known, the Bloch-Siegert shift can be isolated. This could be done, for example, by inducing the second oscillating signal in each spin-flip coil that cancels the Bloch-Siegert shift in the Rabi-type setup as explained in Sec. 10.1. It becomes evident from Eq. (36) that the shift gets cancelled in the Ramsey case if it was cancelled in the Rabi case. With the cancelled Bloch-Siegert shift, the off-resonance effect could be measured. Then the frequency where the curvature is zero corresponds to the true resonance. Any further measurement without the second oscillating signal contains only the isolated Bloch-Siegert effect. Nevertheless, the magnetic field has to be stable over the full time of this procedure which is not given by the current setup.

In conclusion, we showed measurements of the Bloch-Siegert shift in a Rabi-type setup

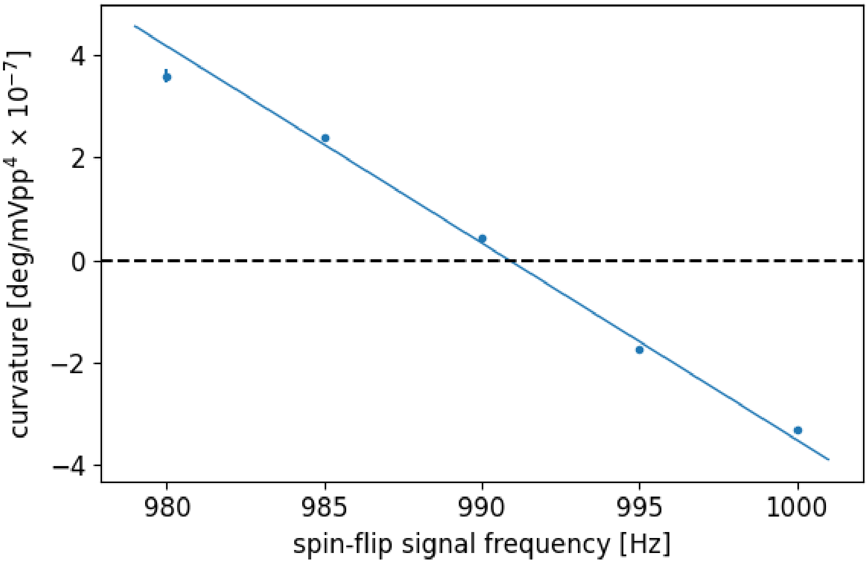

Figure 78: *Curvature a of the measurements shown in Fig. 77 as a function of the applied spin-flip signal frequency. The data are fitted with a linear function that provides a root at* $\omega_{\mathrm{rf}} = 2\pi \times (990.9 \pm 0.1)\ \mathrm{Hz}$. *The dashed line indicates zero curvature.*

with a single spin-flip coil. We further showed how the shift can be compensated or enhanced by inducing a second oscillating signal with a certain combination of frequency and amplitude. The calculated values for this compensation signal do not fully cancel the shift but the right combination can be searched for empirically. We further calculated the Bloch-Siegert shift in a Ramsey-type setup and compared it to the phase pick-up due to an off-resonance pulse. We explained why it is not a simple task to isolate the two effects. Nevertheless, we argued that with a proper choice of the spin-flip signal frequency the two effects cancel each other.

11 Dressed Spin States

The term *dressed states* or *dressed atoms* appeared for the first time in 1969 in a publication by C. Cohen-Tannoudji [139]. In quantum optics it is better known and described by the Jaynes-Cummings model [140, 141]. It describes the interaction of an atom with an RF field where the atom is dressed by the RF photons. In quantum optics, this RF field/photons originate from an optical cavity. In our setup, it can be created by a high-power oscillating magnetic field induced via the spin-flip coil. This dressing with a high number of photons or a high intensity field can lead to a change of the g-factor g of the atom and may even cancel it. This means that the precession can be altered, stopped, and even inverted.

The dressed spin states and consequent effects have also been measured with neutrons [142] and the application for the neutron-antineutron oscillation measurement has been investigated [143]. They were measured recently with ^{3}He in cell and in a Ramsey-type beam experiment [144–146].

The application of dressed spin states could be advantageous in various measurements that are highly sensitive to magnetic field effects. It was suggested to use ^{3}He as a spin analyzer and co-magnetometer in the measurement of the neutron electric dipole moment using ultra-cold neutrons. To minimize systematic effects of small changes in the magnetic field, the change of the g-factor due to dressed states could be applied [144, 145, 147, 148]. At a certain *critical* dressing field, the resonance frequencies of the two species of particles becomes the same and some systematic effects cancel. The dressed spin states could be further applied to optically pumped magnetometers (OPMs) [149–151] to expand the measurement range on the cost of sensitivity.

Here we present the investigation of the dressed spin states of protons. The dressing field is applied via the same coil as the spin-flip signal. The connection diagram is the one presented in Fig. 52 with only one spin-flip coil in use. We show how the dressing field can be used to reduce and increase the gyromagnetic ratio of a particle in Sec. 11.1 and Sec. 11.2, respectively. We further test the application of the dressing field to OPMs to in-situ tune the measurement range and the sensitivity.

11.1 Reducing the Gyromagnetic Ratio

This qualitative derivation follows the one in [147]. It explains the reduction of the gyromagnetic ratio $\gamma = g\mu_N/\hbar$, where μ_N is the nuclear magneton, in the presence of an RF field in a semi-classical framework.

Let's start with an initial spin pointing upwards along z. There is the additional dressing field oriented along x of high enough amplitude B_d, but off-resonance, oscillating with frequency ω_d

$$B_x(t) = B_d \sin(\omega_d t) \ . \tag{40}$$

This field leads to a precession of the spin around the x-axis with

$$\omega(t) \equiv \dot{\vartheta}(t) = \gamma B_x(t) \ . \tag{41}$$

Since the dressing field is oscillating off-resonance and there are no other external fields yet, the movement of the spin can be described as a jitter/wiggling. Integration leads to a time dependent angle with respect to the z-axis of

$$\vartheta(t) = -\gamma \frac{B_d}{\omega_d} \cos(\omega_d t) \ . \tag{42}$$

The projection of the spin vector with angle $\vartheta(t)$ onto the z-axis can be calculated using that $\vartheta_z(t) = \cos(\vartheta(t))$ and the time average becomes

$$\langle \vartheta_z(t) \rangle_T = \frac{1}{T} \int_T \cos\left(\frac{-\gamma B_d}{\omega_d} \cos(\omega_d t) \right) \mathrm{d}t \equiv J_0\left(\frac{\gamma B_d}{\omega_d} \right) \ , \tag{43}$$

where $J_0(x)$ is the Bessel function of the first kind with order zero and dressing parameter $x = \gamma B_d / \omega_d$, which is shown in Fig. 79.

This means that the average z-component of the magnetic moment $\vec{\mu} = \hbar \gamma \vec{\sigma}$ of the spin is reduced. Since this defines the interaction with a magnetic field, it leads to an effective/observed gyromagnetic ratio in the dressing field altered by the Bessel function

$$\gamma_{\text{eff}} = \gamma \times J_0\left(\frac{\gamma B_d}{\omega_d} \right) \ . \tag{44}$$

This argument holds under the condition that the oscillation is fast enough such that taking a time average is reasonable or $2\pi/\omega_d \ll \tau$, where τ is the interaction time with the spin-flip signal.

We measured the effective frequency of the dressed protons at $B_0 \approx 12\ \mu\mathrm{T}$ that corresponds to a resonance frequency of $500\ \mathrm{Hz}$. For various dressing field frequencies we scanned the amplitude of the dressing field and measured the Rabi resonance for each setting. The Rabi-resonance curves for the dressing field frequency $\omega_d = 2\pi \times 2000\ \mathrm{Hz}$ and various amplitudes are shown in Fig. 80. The determined resonance frequencies with a fit of the Bessel function $\omega_0/2\pi \times J_0(x)$ are shown in Fig. 81.

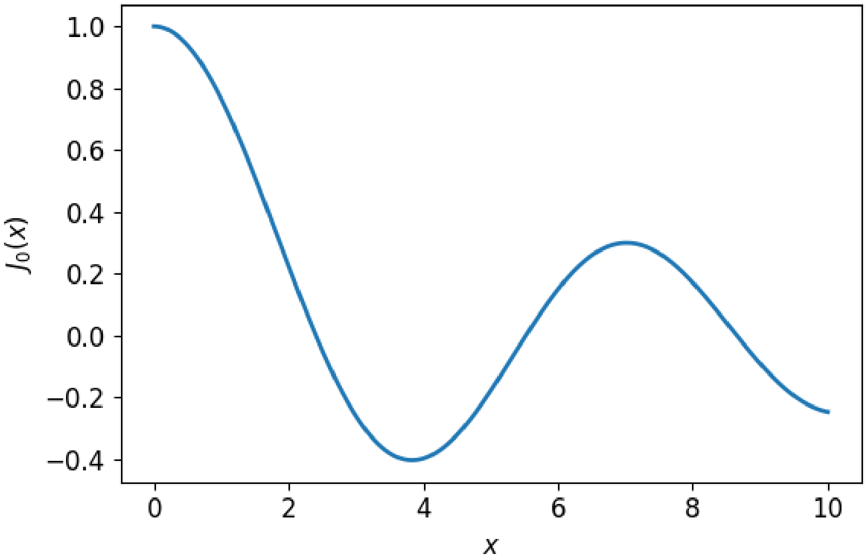

Figure 79: *Bessel function of the first kind of order zero* $J_0(x)$*. In the framework of dressed spin states, the Bessel function describes the modulation of the g-factor and gyromagnetic ratio in the presence of an off-resonance RF field with the dressing parameter* $x = \gamma B_d/\omega_d$*.*

The measurement shows that it is possible to reduce and even cancel the gyromagnetic ratio and, therefore, the resonance frequency. The semi-classical derived model that describes this effect fits well with the data for various dressing field frequencies. As the value of B_d can not be measured and is unknown, it was calculated from the fitted value of the dressing parameter x, using Eq. (44). To put the dressing field amplitude in perspective: the first point of the dressing field amplitude in Fig. 81 of $B_d \approx 1.8\ \mu\mathrm{T}$ corresponds to roughly the spin-flip signal amplitude whereas the last point is a factor of twenty higher.

11.2 Increasing the Gyromagnetic Ratio

It was demonstrated that the precession frequency of ^{3}He in a cell can be increased when applying a dressing field with a frequency lower than the Larmor frequency [145]. This problem can be qualitatively derived, similarly to the case where the dressing field frequency is higher than the Larmor frequency.

Lets assume there is the dressing field of Eq. (40) as before but with a frequency much lower than the Larmor frequency $\omega_d \ll \omega_0$. This means that in the presence of a constant

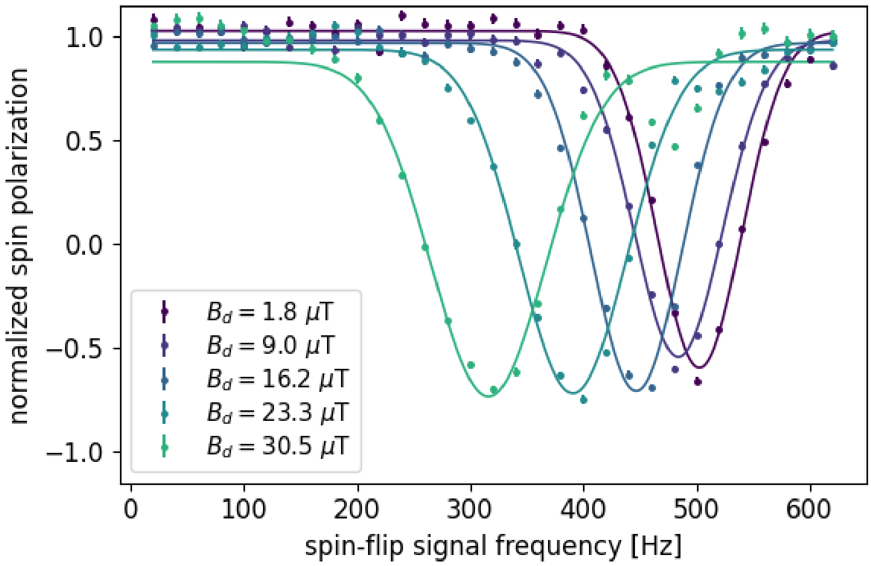

Figure 80: *Rabi resonances at* $\omega_0 = 2\pi \times 500$ Hz *for five amplitudes of the dressing field* B_d *at a frequency of* $\omega_d = 2\pi \times 2000$ Hz. *Shown is the normalized spin polarization as a function of the spin-flip signal frequency. The resonance frequency shifts to lower values with increasing amplitude* B_d *as predicted by Eq. (44).*

vertical magnetic field B_0, the magnitude of the magnetic field is

$$|B| = \sqrt{B_0^2 + B_d^2 \sin^2(\omega_d t)} \approx B_0 + \frac{B_d^2 \sin^2(\omega_d t)}{2B_0} \ , \tag{45}$$

where in the second step we used that $B_d \ll B_0$.

We can calculate a time average of the field, as long as $2\pi/\omega_d \ll \tau$, meaning that the spin interacts with multiple oscillations of the dressing field.

$$\langle |B| \rangle_T = B_0 + \frac{B_d^2}{2B_0} \frac{1}{T} \int_T \sin^2(\omega_d t) \mathrm{d}t = B_0 + \frac{B_d^2}{4B_0} = B_0 \left(1 + \frac{B_d^2}{4B_0^2}\right) \tag{46}$$

This time average is the effective field that the spins see while passing the spin-flip coil. It is still vertically oriented along the z-axis but has a higher magnitude as the last term of Eq. (46) indicates. Since the effective field increases, so does the effective gyromagnetic ratio with the same quadratic dependence

$$\gamma_{\text{eff}} = \gamma \times \left(1 + \frac{B_d^2}{4B_0^2}\right) \ . \tag{47}$$

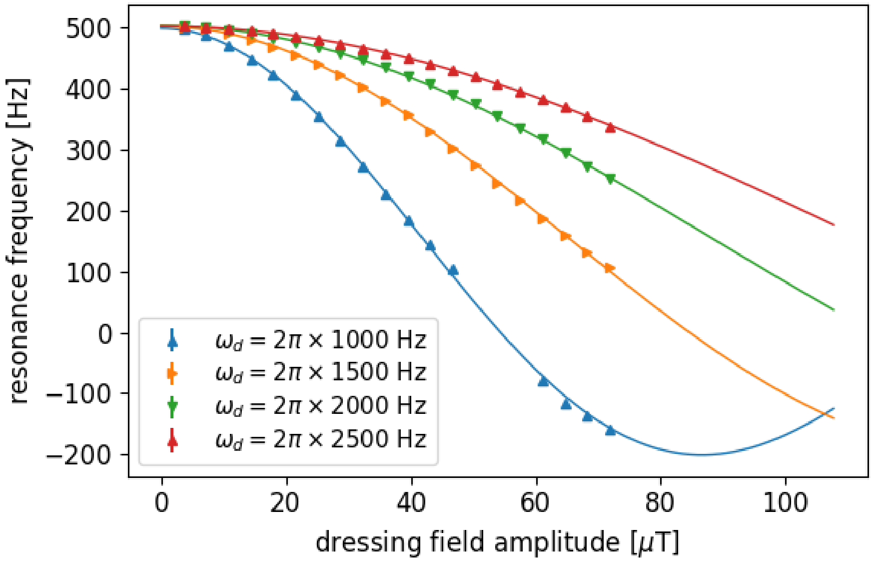

Figure 81: *Measurement of the dressed proton resonance frequency in a magnetic field of* $B_0 \approx 12\ \mu\mathrm{T}$. *We scanned the amplitude of the dressing field* B_d *at* $1000\ \mathrm{Hz}$ *(blue ▲),* $1500\ \mathrm{Hz}$ *(orange ▶),* $2000\ \mathrm{Hz}$ *(green ▼), and* $2500\ \mathrm{Hz}$ *(red ◀). The data are fitted with Bessel functions of the first kind and order zero. Points with an absolute resonance frequency smaller than* $75\ \mathrm{Hz}$ *were not included in the analysis. The sign of the negative points was flipped manually since the Rabi method is not able to distinguish between positive and negative resonance frequencies.*

We measured the effective frequency of the dressed protons at $B_0 \approx 24\ \mu\mathrm{T}$ that corresponds to a resonance frequency of $1000\ \mathrm{Hz}$. The dressing field frequency was set to $250\ \mathrm{Hz}$ and the amplitude of the dressing field B_d was scanned. The Rabi-resonance curves for various amplitudes of the dressing field are shown in Fig. 82 and the determined resonance frequencies with a quadratic fit are shown in Fig. 83.

The data show that the resonance frequency, or equivalent the gyromagnetic ratio, can be increased by inducing a dressing field with a frequency lower than the Larmor frequency. Because the qualitative derivation makes the assumption that $B_d \ll B_0$, we did not include data points in the fit that do not fulfill this condition. As the value of B_d cannot be measured and is unknown, we use the same scaling as in Sec. 11.1 where the dressing field amplitude of the first point is roughly the same as the spin-flip signal amplitude.

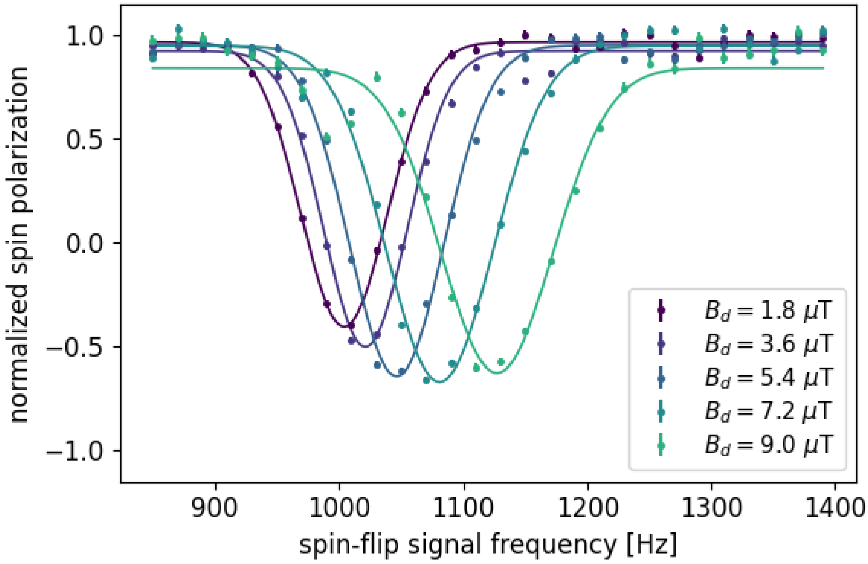

Figure 82: *Rabi resonances at* $\omega_0 = 2\pi \times 1000$ Hz *for five amplitudes of the dressing field* B_d *at a frequency of* $\omega_d = 2\pi \times 250$ Hz*. Shown is the normalized spin polarization as a function of the spin-flip signal frequency. The resonance frequency shifts to higher values with increasing amplitude* B_d *as predicted by Eq. (47).*

11.3 Rubidium Magnetometer Range Tuning

One application of the dressed spin states is in the field of OPMs. The sensor we tested is a Gen-2 QuSpin zero-field magnetometer [151]. It has a measurement range of about ± 3 nT and field sensitivity of $< 15\ \mathrm{fT}/\sqrt{\mathrm{Hz}}$.

The basic principle of an OPM is as follows. They have a small gas cell, in the case of our sensor it is a rubidium gas at about 40 °C. A laser is then passed through the gas and creates a magnetically sensitive state that has a transmission function of the laser light that depends on the external magnetic field. A photo diode is placed behind the cell that measures the light transmission. The voltage of the photo diode is linearly proportional to the magnetic field within the measurement range

$$V(B) = A_0 \gamma_{\mathrm{Rb}} T_r B \ , \tag{48}$$

where A_0 is a proportionality constant, $\gamma_{\mathrm{Rb}} \approx 7\ \mathrm{Hz/nT}$ [152] the gyromagnetic ratio of the rubidium, and T_r the relaxation time of the sensitive state of the rubidium.

To alter the measurement range and the sensitivity either T_r or γ_{Rb} can be changed. T_r is given by the sensor. It depends on the gas volume and density and can only be changed by

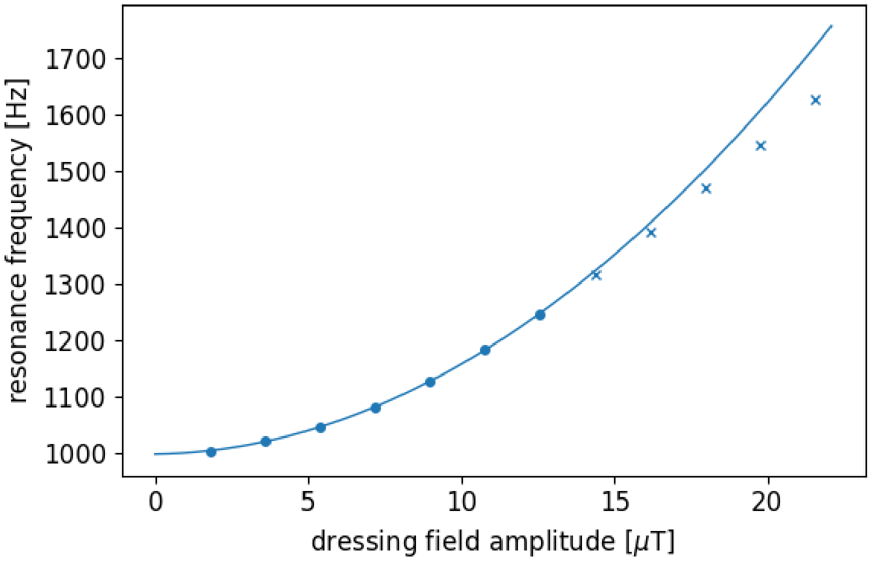

Figure 83: *Measurement of the dressed proton resonance frequency in a magnetic field of* $B_0 \approx 24\ \mu\mathrm{T}$*. We scanned the amplitude of the dressing field* B_d *at* $250\ \mathrm{Hz}$*. The data are fitted with a quadratic function (solid line). Points with a dressing field amplitude of* $B_d > 13\ \mu\mathrm{T}$ *(blue crosses) were not included in the quadratic fit as they do not fulfill the condition* $B_d \ll B_0$*.*

the manufacturer. On the other hand, with the dressed spin method, a high-frequency field can be applied via an external coil around the sensor. This would change γ_{Rb} and, therefore, also results in an altered measurement range.

To qualitatively test this idea, we created a simple setup with one rubidium sensor surrounded by a coil to apply the dressing field as shown in Fig. 84. The coil is a single loop of copper wire around the rubidium sensor, orthogonal to the sensitive axis of the sensor. The sensor and the coil are mounted on a holder that is placed in the center of a four-layer mu-metal shield Twinleaf MS-2 [153]. The shield itself has internal coils on a Kapton-foil that can be used to create magnetic field in all three spatial direction.

To measure the response of the OPM, we applied an oscillating voltage in the vertical direction at a frequency of $500\ \mathrm{mHz}$ at various amplitudes. This serves as a reference measurement and corresponds to the blue data in Fig. 85. We then applied dressing fields of various amplitudes at $\omega_d = 2\pi \times 2000\ \mathrm{Hz}$. For each dressing field amplitude we repeated the measurement. The data are presented in Fig. 85.

For higher dressing field amplitudes, the ratio of the measured field and the applied field reduces. It is one by definition for the case were no dressing field is applied. For the dressing

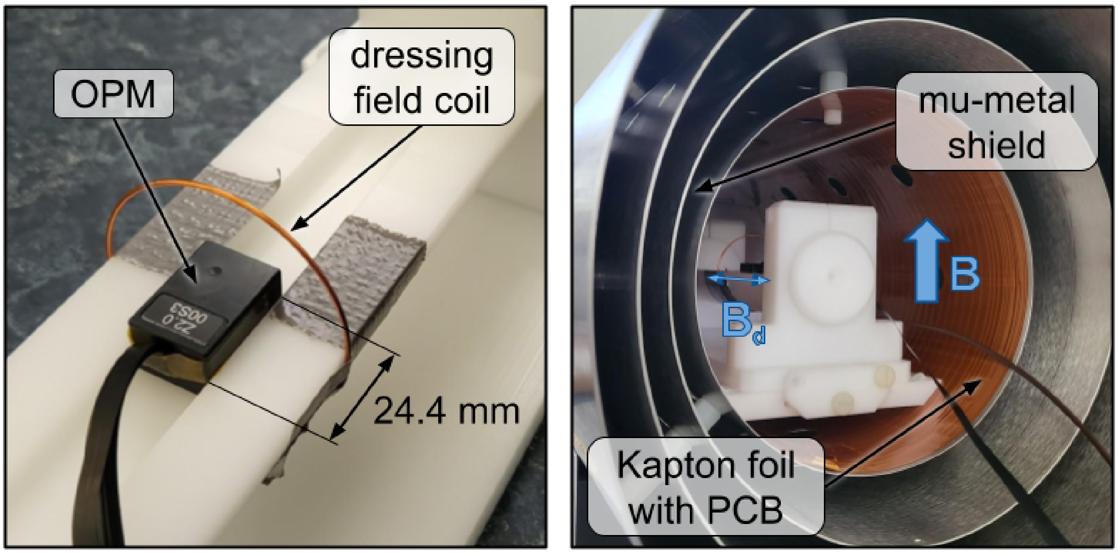

(a) (b)

Figure 84: *Photos of the setup used to test the in-situ tuning of the measurement range of the rubidium magnetometer. (a) The rubidium sensor is placed in a holder such that the sensitive cell is in the center of the copper-wire loop. (b) The holder with the sensor and the wire to apply the dressing field is placed in a four-layer mu-metal shield. The orange Kapton layer inside of the innermost mu-metal layer has printed electronic circuits that can be used to apply magnetic fields in all spatial directions. The end caps of all four mu-metal layers were removed for the photo but mounted for the measurement.*

field at the applied voltages of $50\ \mathrm{mV}$, $100\ \mathrm{mV}$, and $150\ \mathrm{mV}$ the linear fit shown in Fig. 85a revealed a slope of 0.77 ± 0.03, 0.44 ± 0.01, and 0.262 ± 0.005. This slope is proportional to the sensitivity and inversely proportional to the measurement range. For a dressing field with an applied voltage of $150\ \mathrm{mV}$ for instance, the sensitivity reduces to 26% and the range increases by a factor of 3.8.

Figure 85b shows that for the measurements with an applied dressing field, the relation between the measured and applied field is not linear anymore. The data are fitted with a quadratic function but it can be seen that it does not fit well. Nevertheless, the data show that indeed the measurement range could be increased by applying a dressing field.

To confirm or disprove that this change in sensitivity is actually due to the effect of the dressed spin states, we performed an amplitude scan of the dressing field while keeping the amplitude of the main field at the same value. According to the theory and the measurements presented in Sec. 11.1, the measured field amplitude as a function of the dressing field

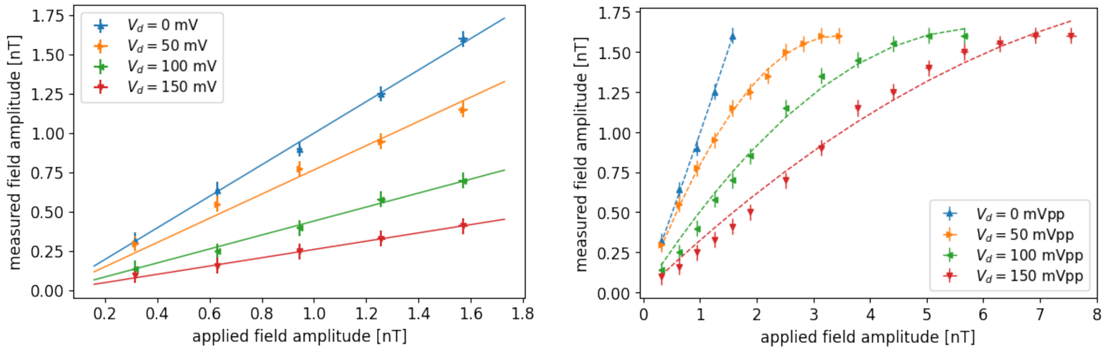

(a) (b)

Figure 85: *Measured magnetic field amplitude of the rubidium magnetometers as a function of the applied field amplitude. The measurement without a dressing field (blue ▲) serves as a reference. The dressing field at* $\omega_d = 2\pi \times 2000$ Hz *was applied with a voltage of* 50 mV *(orange ▶),* 100 mV *(green ▼), and* 150 mV *(red ◀). (a) Linear measurement range of the sensor. The data are fitted with linear functions that go through the origin. The measured field amplitude of the sensor compared to the applied field amplitude was reduced due to the dressing field. (b) Full measurement range up to the field where the sensor was saturated. The dashed lines correspond to quadratic least-squares fits and serve only as a guide for the eyes.*

amplitude should follow a Bessel function. For this measurement we sampled the read-out of the rubidium sensor with 10 kHz instead of 10 Hz as before. This revealed that the dressing field signal is also present in the data from the rubidium sensor. In the measurement before it was just averaged out. To avoid this, we increased the dressing frequency to $\omega_d = 2\pi \times 10$ kHz. We tested this by sampling the OPM read-out much faster than the dressing frequency. The dressing signal was not present anymore.

Figure 86 presents the data of the dressed field amplitude scan. It does not show the behaviour of a Bessel function but rather an exponential suppression. The increased measurement range shown in Fig. 85 must either be suppressed at high dressing field amplitudes or originate from another effect. Yet, it is not clear why the range could be increased. Therefore, the effect of the dressing field frequency and amplitude on the OPMs must be further tested.

A possible reason is a saturation effect if the dressing field is also present in the active axis of the sensor. To avoid this, the alignment of the dressing field coil and the sensor should be improved. A single loop may not be enough to create a homogeneous field so a Helmholtz-type coil could help. Additionally, the sensor has actually two sensitive axes and

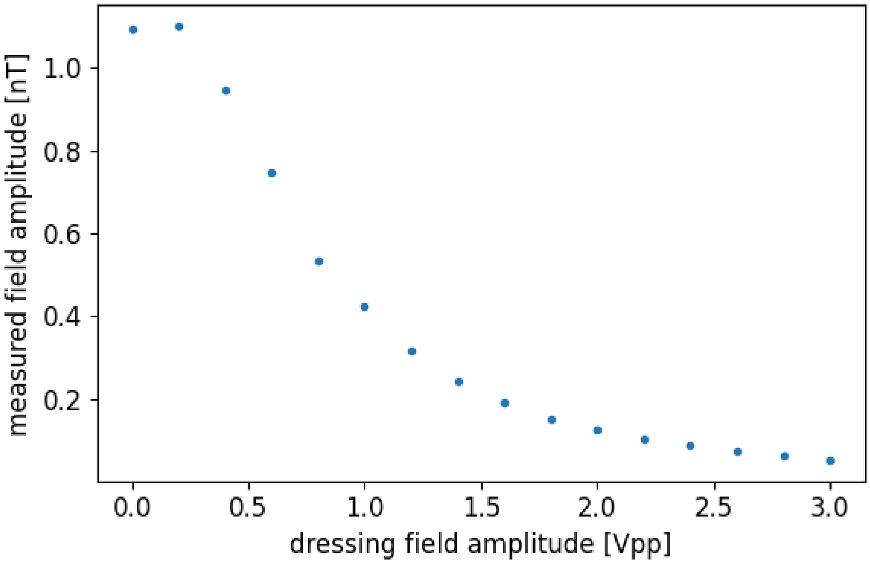

Figure 86: *Measured field amplitude for an amplitude scan of the dressing field at a fixed frequency* $\omega_d = 2\pi \times 10\ \mathrm{kHz}$. *If the dressing field had changed the gyromagnetic ratio of the rubidium, the data would follow a Bessel function. The data show rather an exponential suppression.*

for the measurement both were active. There could be some crosstalk between the two when high-frequency fields are applied. The sensor should be used with only one axis active and the dressing field should be in the direction were the sensor is insensitive.

In conclusion, we investigated for the first time the dressed spin states of protons. Besides the well-known suppression of the g-factor or the gyromagnetic ratio, we also performed a measurement where we enhanced them. For the enhancement we developed an intuitive way, approaching the shift analytically with only basic assumptions. The model seems to be valid within the applicable range. Additionally, we tried to apply this technique to OPMs to tune the sensitivity and measurement range in-situ. Even though we were able to tune the sensitivity, it is unclear if the effect is related to the dressed spin states. Nevertheless, further investigation is needed to find an explanation for the observed behaviour.

12 Exotic Interaction

12.1 Theory and Introduction

Extensions of the SM usually predict new particles and gauge bosons. Recently, long-range interactions between macroscopic objects mediated by light bosons have been parametrized [154, 155]. Such an interaction can be represented by the Feynman diagram shown in Fig. 87.

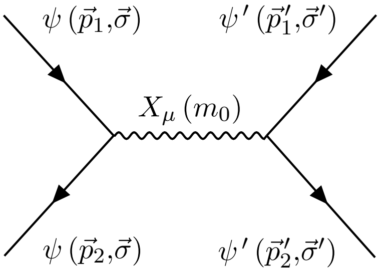

Figure 87: *Generic elastic interaction between two fermions ψ and ψ' via the exchange of a single vector boson X_μ with mass m_0. The fermions are characterized by their momentum $\vec{p}$ and spin $\vec{\sigma}$.*

The parametrization resulted in a complete set of 16 spin- and momentum-dependent potentials between two fermions assuming only rotational invariance. In the case of the exchange of a single new light but massive spin-1 vector boson X_μ the low-energy interaction with a fermion ψ can be described with the Lagrangian

$$\mathcal{L} = \overline{\psi}\left(g_V\gamma^\mu + g_A\gamma^\mu\gamma^5\right)\psi X_\mu \ , \tag{49}$$

where g_V is the vector coupling constant, g_A the axial-vector coupling constant, and $\gamma^5 = i\gamma^0\gamma^1\gamma^2\gamma^3$ the Dirac matrices.[r] Without loss of generality, it can be assumed that X_μ is the gauge boson associated with the symmetry breaking of a $U(1)$ symmetry. The coupling constants are in general different for electrons, protons, and neutrons which is indicated with superscript e, p, and n, respectively. Certain requirements and constraints may apply. For example, to have a self-consistent theory that includes the new $U(1)$ gauge group but avoids new fermions charged by it, then $g^p_{V,A} + g^e_{V,A} = 0$ has to be satisfied [156]. This

---

[r] Similarly, the interaction with the exchange of a spin-0 boson can be parametrized by the scalar and pseudo-scalar coupling constants g_S and g_P, respectively.

would mean that the coupling is only proportional to the number of neutrons.

For a monopole-dipole interaction where the spin of one point-like object is $\vec{\sigma}$ and the other object is unpolarized, the corresponding interaction potential gets the form

$$V_\sigma(\vec{r},\vec{v}) = \frac{1}{8\pi r}\left(f_v\,\vec{\sigma}\cdot\vec{v} + \left(f_r\,\vec{\sigma}\cdot\hat{\vec{r}} + f_\perp\,\vec{\sigma}\cdot\left(\vec{v}\times\hat{\vec{r}}\right)\right)\frac{1+r/\lambda}{m_\sigma r}\right)e^{-r/\lambda}\ , \tag{50}$$

where $\hat{\vec{r}}$ is the unit vector pointing from the unpolarized object to the polarized one, $\vec{v}$ the center-of-mass velocity or the relative velocity between the two objects assuming their particles having the same mass, m_σ the mass of the polarized probe particle, and $\lambda = \hbar/m_0 c$ the interaction range of the exchange boson with mass m_0. This potential corresponds to Eq. (4.3) in [154]. The f_v, f_r, and $f_\perp$ are dimensionless coefficients of the potentials that belong to the corresponding configuration of $\hat{\vec{r}}$, $\vec{v}$, and $\vec{\sigma}$.

The first measurement of a velocity dependent potential was performed using a torsion pendulum containing polarized electrons. They could constrain the $|g_P^e g_S^{\mathcal{N}}|$ and $|g_A^e g_V^{\mathcal{N}}|$ for interaction length on the order of the mean earth-sun distance $\lambda > 1\,\mathrm{AU} \approx 10^{11}$ [157]. Many other searches of these new long-range interactions from subatomic to astronomical distances have been performed [158–164]. Depending on their experimental configuration they could constrain couplings between various combinations of fermions (electrons, protons, neutrons), various combinations of couplings (scalar, pseudo-scalar, vector, axial-vector), and various types of interactions (monopole-monopole, monopole-dipole, dipole-dipole). Yet, such long-range interactions have to our knowledge never been measured using polarized protons as probe particles.

We intend to use protons from hydrogen nuclei in water molecules as probe particles and a copper block as the source. The source should have a high nucleon number density and be non-magnetic. The polarized protons pass by the unpolarized copper sample in close proximity. The geometrical configuration is such that $\vec{\sigma} \perp \vec{v} \perp \hat{\vec{r}}$. Therefore, only the $f_\perp$ term of Eq. (50) remains and the potential becomes

$$V_\perp^{\text{point}} = \frac{f_\perp}{8\pi m}\frac{e^{-r/\lambda}}{r}\left(\frac{1}{r}+\frac{1}{\lambda}\right)\vec{\sigma}\cdot\left(\vec{v}\times\vec{r}\right)\ , \tag{51}$$

where the superscript *point* indicates that it is the potential between two point-like objects.

The full term of $f_\perp$ is given by Eq. (5.28) in [154]

$$f_\perp^{p\mathcal{N}} = \left(\frac{1}{2}+\frac{m_p}{m_{\mathcal{N}}}\right)g_V^p g_V^{\mathcal{N}} + \frac{m_p^2}{2m_{\mathcal{N}}^2}g_A^p g_A^{\mathcal{N}} + 4\left(1+\frac{m_p}{m_{\mathcal{N}}}\right)g_V^{\mathcal{N}}\frac{v_h m_p}{M^2}\,\mathrm{Re}(C_p)\ , \tag{52}$$

where the superscripts p and $\mathcal{N}$ indicate the interaction between a proton and a nucleon.

They can be replaced by whatever particles are involved in the interaction. It can be seen that in the case of an electron as a probe particle, most of the terms are highly suppressed by the mass ratios. The first term includes only vector couplings, whereas the second term only includes axial couplings. The third term corresponds to a higher-dimensional interaction describing magnetic- and electric-like dipole couplings. It is suppressed by some mass scale $1/M^2$ that is larger than the vacuum expectation value v_h of the symmetry breaking field. C_p is a dimensionless complex parameter.

The sample geometry is chosen such that it can be regarded semi-finite. Since the potentials of the individual nucleons add up coherently, the point-like potential of Eq. (51) can be integrated over the copper volume. Additionally, the interaction potential is linearly proportional to the proton spins and can be regarded as a pseudo-magnetic field effect $V = -\mu_p B^* = -\frac{1}{2}\gamma_p \hbar \vec{\sigma} \cdot \vec{B}^*$ [165]. Therefore, the pseudo-magnetic field can be calculated analytically, resulting in

$$B_\perp(\Delta x) = \frac{f_\perp}{2} \frac{N\hbar v}{\gamma_p m_p c} \lambda e^{-\Delta x/\lambda} \,, \tag{53}$$

where Δx is the distance from the protons to the copper surface, γ_p the gyromagnetic ratio of the proton, $N = 5.4 \times 10^{30}\ \mathrm{m}^{-3}$ the nucleon number density of copper, and m_p the proton mass. The calculation of the integration over the copper volume and the derivation of Eq. (53) can be found in Appendix A.3.

The additional phase that the protons acquire in the Ramsey-type setup due to the new interaction is

$$\Delta\varphi = \gamma_p B_\perp \frac{l}{v} = \frac{f_\perp}{2} \frac{N\hbar l}{m_p c} \lambda e^{-\Delta x/\lambda} \,, \tag{54}$$

where l is the length of the copper sample.

12.2 Add-On of the Setup to Measure Exotic Interactions

An add-on to the interior described in Sec. 7.3 was designed to measure the exotic interaction. The requirement was to be able to move the copper sample close to the glass capillary between the spin-flip coils without changing anything on the setup. Most crucial is the mu-metal, as touching it can easily change the magnetic field in the interior slightly. This could mimic the effect of an exotic interaction. A second requirement was the repeatability of the sample position and its separation to the capillary.

The solution is a base plate with notches that guide a sled with pins. The sample can be put on the sled and be fixed with headless screws. The sled can be pushed in from both sides and when being close to the center position, the notches guide it to the capillary. Pins of various diameters can be mounted below the capillary. They define the stop position of the sled and the separation to the water. A CAD rendering of the add-on is shown in Fig. 88 and a photo of the view into the mu-metal with the add-on is presented in Fig. 89.

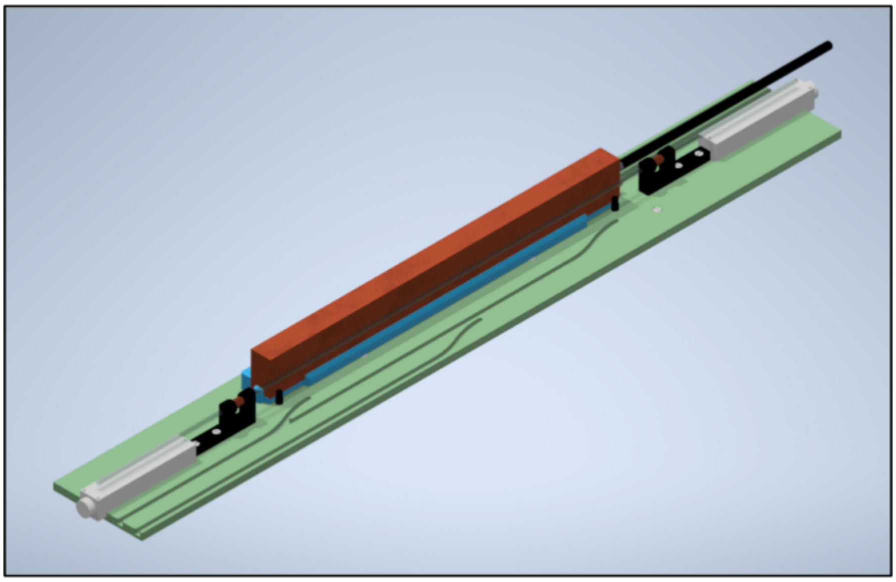

Figure 88: *CAD rendering of the add-on for measuring the exotic interaction. It shows the base plate with the notches (green) that guide the sled (blue) where the copper sample (orange) can be placed on top. The sled can be placed on both sides of the water pipe and can be moved by the handle. Two fluxgates (white) measure the magnetic field before and after the spin-flip coils (black). The two positioning pins at the edge of the copper are also shown in black.*

The holding structure of the spin-flip coils was redesigned. It was necessary to design them as slim as possible such that the sample can pass by. The coils themselves have the same dimensions as described in Sec. 7.3 but with one winding more as they were wound tighter, resulting in 17 windings in total.

To have a more accurate measurement of the magnetic field, a second fluxgate was added before the first spin-flip coil. Since only one SENSYS FGM3D/125 fluxgate was available, we switched to two FGM3D/250 fluxgates [65]. They are exactly the same but with a broader measurement range of $\pm 250\ \mu\mathrm{T}$ and a slightly higher noise level.

12.3 Copper Sample

The copper sample that we use to measure the exotic interaction is made from oxygen-free copper of quality C11000, also known as electrolytic-tough pitch (ETP). It has a copper content of $> 99.9\%$ [166]. This ultra-pure copper is required to minimize magnetic impurities

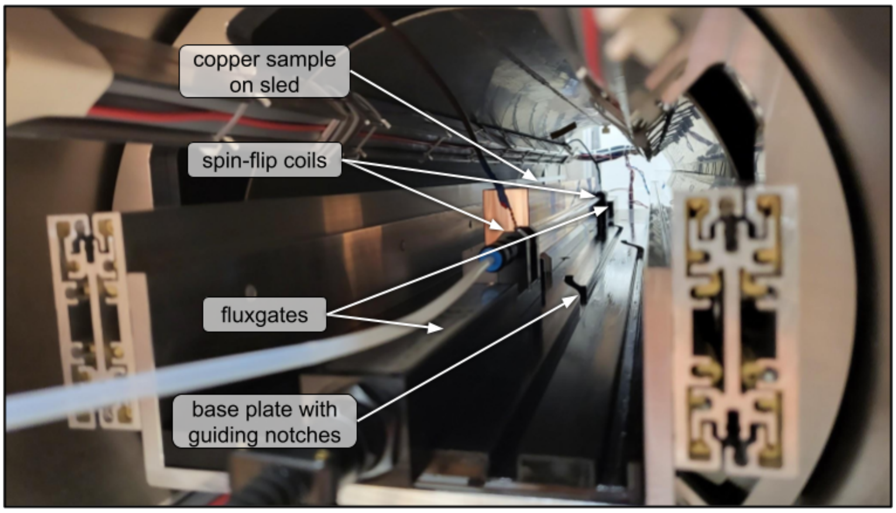

Figure 89: *Photo of the view into the mu-metal with the add-on for the exotic interaction mounted onto the U-profile. The notches of the base plate are visible right of the center. The sled with a copper sample mounted is visible left of the glass capillary.*

that could mimic a false exotic effect. The sensitivity of the measurement is proportional to the length. We maximized the length of the sample to $500\ \mathrm{mm}$ to still be able to fit it between the two spin-flip coils.

The transversal size of the copper sample was chosen such that it can be assumed to be infinite from an exotic interaction point of view. If the sample is at the position close to the capillary, the distance to the center of the water pipe is $\Delta x = 3.5\ \mathrm{mm}$. The Yukawa-like potential of the interaction under test Eq. (51) is proportional to e^{-r}, where r is the distance from the protons in the water to the nucleons of the copper sample. The effect of nucleons further away than $5 \cdot \Delta x = 17.5\ \mathrm{mm}$ from the water pipe have an effect of less than 1% and can be neglected. To fulfill this condition, we chose a transversal size of $28 \times 49\ \mathrm{mm}^2$. The flatness of all surfaces facing the water is better than $0.01\ \mathrm{mm}$.

The copper sample is divided into two blocks of length $250\ \mathrm{mm}$. This has the advantage of easier processing, testing, and handling. The two blocks were manufactured such that there is no gap and no visible edge when put next to each other. A photo of the sled with the two copper blocks mounted on top is presented in Fig. 90.

The remanent magnetic fields of the copper blocks were measured at the Physikalisch-technische Bundesanstalt in Berlin, Germany. They have a magnetically shielded room with a detector using superconducting quantum interference devices (SQUIDs) to measure relative magnetic fields changes on the sub-pT level [167]. The distance from the used sensor to the surface of the copper was $35\ \mathrm{mm}$. The sensor was at a fixed position and a turn-table

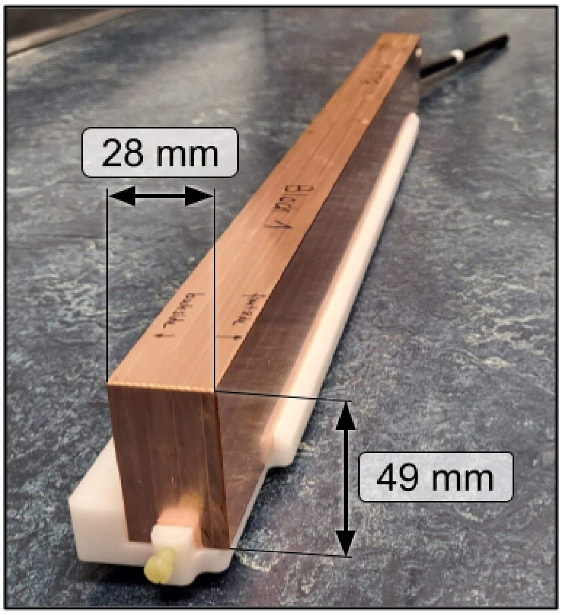

Figure 90: *Photo of the sled with the copper sample mounted on top. The lever to push the sled into the mu-metal is visible in the background. The copper sample is made of two blocks with a cross-section of* $28 \times 49\ \mathrm{mm}^2$ *and a length of* $250\ \mathrm{mm}$ *each. There is no visible edge between the two blocks.*

with both blocks on opposite sides rotated below it. The magnetic field of the blocks was measured in two runs, one for each side of the copper facing the SQUID.

It was shown, that the copper samples can be magnetized to over $500\ \mathrm{pT}$ from peak to peak with a strong permanent magnet and/or demagnetized or degaussed with a degaussing device as the SV91M [168]. The data presented in Fig. 91 indicate that the copper has a remanent magnetic field of $< 20\ \mathrm{pT}$ from peak to peak at a distance of $35\ \mathrm{mm}$ after the degaussing. Additionally it became clear during the measurements that also thermal effects are present that could mimic a magnetic field.

To qualitatively check the data presented in Fig. 91, we measured the remanent magnetic field of the copper in a non-cryogenig environment in our laboratory in Bern, using a Gen-2 QuSpin zero-field magnetometer [151] with a measurement range of about $\pm 3\ \mathrm{nT}$. Since the sensor is small, the active cell can measure the magnetic field of the copper at a distance of only about $9\ \mathrm{mm}$. The sensor was placed in the center of a four-layer mu-metal shield Twinleaf MS-2 [153] with the endcaps on one side removed. The copper sample was manually moved over the sensor. We measured the magnetic field after magnetization with a strong permanent magnet and after degaussing. The former measurement showed that the sample

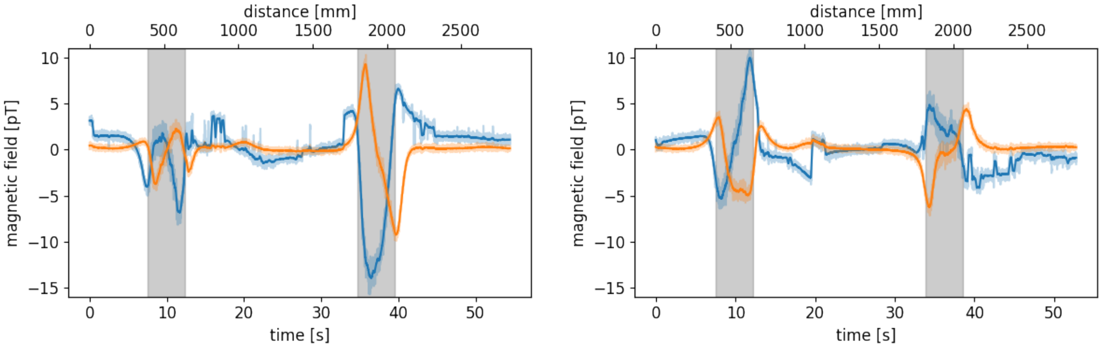

(a)

(b)

Figure 91: *Measurement of the remanent magnetic field of the copper blocks using a SQUID sensor at a distance of* $35\ \mathrm{mm}$*. As the table with the samples is rotating below the sensor, the horizontal axis below is the measurement time of a full rotation. The horizontal axis above is the corresponding distance along the circumference on which the samples are centered. Subfigures (a) and (b) show the data of the frontside and the backside, respectively. The blue line corresponds to the direction of the surface normal and the orange line to the longitudinal direction. The light colors correspond to the full data and the dark colors to the data after applying a Savitzky-Golay filter [97]. The gray shaded areas in each subfigure indicate the position of block 1 (left) and block 2 (right).*

can indeed be magnetized as the QuSpin sensor was saturated at $3\ \mathrm{nT}$. After degaussing the remanent magnetic field was again well within the range of the sensor. To get quantitative results, a device should be designed to move the sample in a controllable way over the sensor.

Since the copper sample has a remanent magnetic field even after degaussing, we had to develop a measurement scheme to compensate the magnetic effects. This scheme is described in Sec. 12.4. There exist also copper of even better quality than the C11000 which could be used to further reduce the remanent magnetic fields.

12.4 Measurement Scheme

The measurement scheme has to be able to observe the effect of the exotic interaction but distinguish it from other magnetic effects. This can be done by placing the sample on both sides of the water pipe such that the same side faces the capillary. This changes the surface normal $\hat{\vec{r}}$ with respect to the proton velocity $\vec{v}$ and flips the sign of the pseudo-magnetic field of the exotic interaction $B_\perp$ while keeping the sign of all other magnetic effects from the external magnetic field B_0 and the copper itself B_c. By subtracting the two measurements, these systematic effects can in principle be compensated. Additionally, the magnetic field may slightly changed by δB when moving the sample from one side to the other. The reason for this is that all the mechanical parts of the experiment are fixed to the mu-metal shield. Placing the sample in the interaction zone results in mechanical stress of the mu-metal that changes its magnetization. This can be accounted for by taking a reference measurement of the proton phase after each changing of the sample side. Table 3 summarizes the measurement scheme to compensate for both systematic effects and Fig. 92 shows a schematic of the four measurement positions. The reference measurement was performed by moving the sample far away from the water pipe such that the magnetic effects from the sample are negligible.

label	**side**	**separation**	**fields**
p_0	right	$3.5\ \mathrm{mm}$	$+B_\perp + B_c + B_0$
p_1	right	$20\ \mathrm{mm}$	$+B_0$
p_2	left	$3.5\ \mathrm{mm}$	$-B_\perp + B_c + B_0 + \delta B$
p_3	left	$20\ \mathrm{mm}$	$+B_0 + \delta B$
$p_r = p_0 - p_1$	right		$+B_\perp + B_c$
$p_l = p_2 - p_3$	left		$-B_\perp + B_c$
$p_r - p_l$			$2B_\perp$

Table 3: *Positions of the copper sample to measure the exotic interaction and the corresponding fields that interact with the proton spins. The left and right position, indicated with subscripts l and r, are viewed from upstream to downstream. The exotic interaction $B_\perp$ has a different sign on the left side compared to the right side whereas the other magnetic field effects from the copper B_c and from the external magnetic field B_0 have the same sign. The δB indicated that there could be a magnetic field change due to the repositioning of the copper from one side to the other. The exotic field and the magnetic effects from the copper are assumed to be negligible in the far position.*

12.5 Measurement of the Exotic Interaction

We performed several measurements of the exotic interaction. It quickly became clear, that the measurement could not be performed properly with the current setup as there were too many systematic effects. The weight of the copper sample and the friction of the sled on the POM base plate were too high to be able to change the sample position without changing the magnetic field. We reduced the sample length by half to reduce the weight. The systematic effects reduced but still a proper exotic measurement was impossible to perform. Nevertheless, the data and analysis are presented.

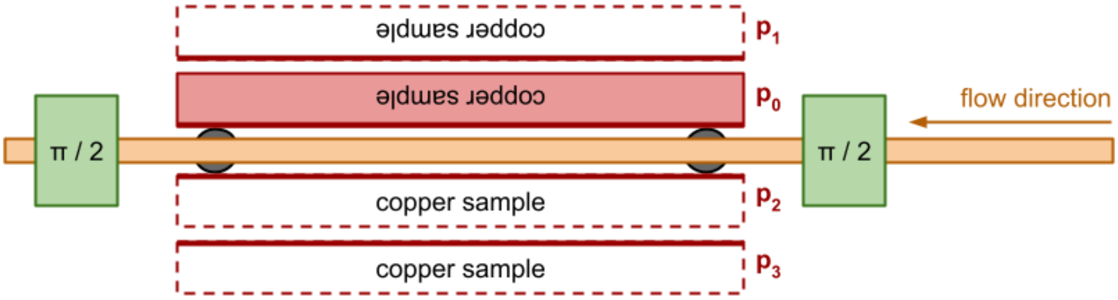

Figure 92: *Schematic with the four positions of the copper sample (p_0 to p_3) to measure the exotic interaction. The copper sample (red) is placed such that always the same side is facing the water, indicated by the thick solid edge. The water flows from right to left through the glass capillary (orange). The two positioning pins (black) between the two spin-flip coils (green) allow for a precise positioning of the copper in the close position.*

The exotic measurement was performed in ten sequences. In each sequence, the copper sample was placed at the four different positions as summarized in Table 3. At each position, three consecutive Ramsey phase scans were performed and averaged. This led to a total measurement time of about 30 minutes for one sequence which is within the time frame of the phase stability as shown in Fig. 69.

The first indication that systematic effects are dominating the measurement of the exotic interaction is the magnetic field data that was measured by the two fluxgates. We calculated the average of the vertical magnetic field component of both fluxgates over the measurement time of all three phase scans at each position. Figures 93a and 93b show the resulting magnetic fields and the difference of the magnetic fields between the close and the far position on each side, respectively.

The fluxgate data show that the external magnetic field B_0 was different for each measurement position and so is δB. At least the B_0 fields for the two measurements on each side, i.e., p_0/p_1 or p_2/p_3, have to be the same for the measurement scheme to work. This would be the case if all values in Fig. 93b were in agreement with zero. This is never the case for the magnetic field values of both sides. Therefore, none of measurement sequences can be used for a test of the exotic interaction.

The second indication of the large systematic effects of the measurement with the current setup is visible in the proton phase data presented in Fig. 94. It shows the resulting phase shift due to "only" the exotic interaction $B_\perp$, corresponding to the last row in Table 3. It is evident that the fluctuation of the data is not in agreement with their uncertainty. If there was no exotic interaction, all values should be statistically distributed around zero. These shifts can be explained by the magnetic field changes measured by the fluxgates. We tried to

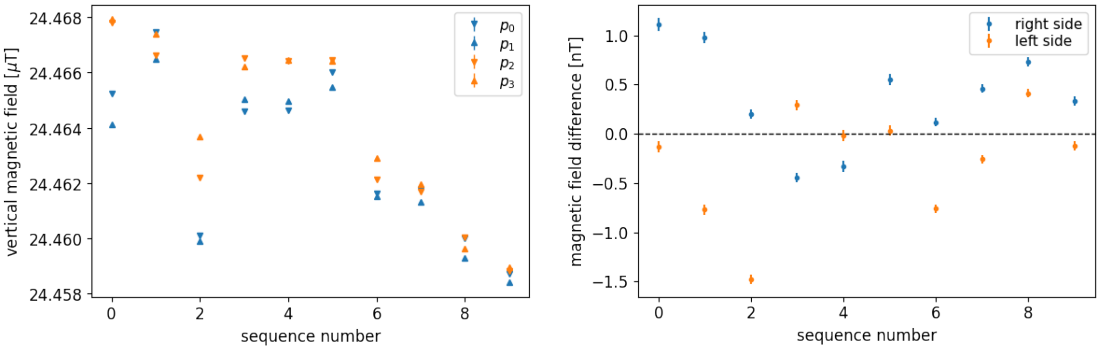

(a) (b)

Figure 93: *(a) Magnetic field values for the measurements on the right side (blue) and the left side (orange) as a function of the sequence number. The close positions with a separation of* 3.5 mm *are indicated with* ▼ *and the far positions with a separation of* 20 mm *with* ▲. *The vertical magnetic field components of both fluxgates was averaged over the measurement time of all three phase scans at each position. (b) Difference of the close and the far of the magnetic field values shown in (a) for each side. The dashed line indicates zero magnetic field difference.*

use the magnetic field data to correct for the phase changes. Since the fluxgates do measure before and after the interaction region and maybe also due to inhomogeneous field changes, the correction could not improve the situation.

One solution to this problem would be to implement a second water pipe that can be used as a reference measurement without a copper sample as it was done for the neutron measurement of the same interaction at ETHZ [61]. This would sample the external magnetic field at the same time as the exotic interaction, making the measurements p_1 and p_3 unnecessary. It was not implemented in this work due to time constraints.

Since the data cannot be used for an investigation of the exotic interaction, we use a value of $\Delta\varphi = 0° \pm 1°$ as an example for an illustrative analysis and to get a projected sensitivity. The analysis is simple since we only measured at a single separation of $\Delta x = (3.5 \pm 0.1)$ mm. We did not take into count the form factor of the water pipe since this will only be a small effect. In Eq. (54), all the constants can be substituted to simplify the equation to

$$\Delta\varphi = \varphi_0 \times e^{-\Delta x/\lambda} \,, \tag{55}$$

where φ_0 is the only free parameter that can be fitted or in our case analytically calculated

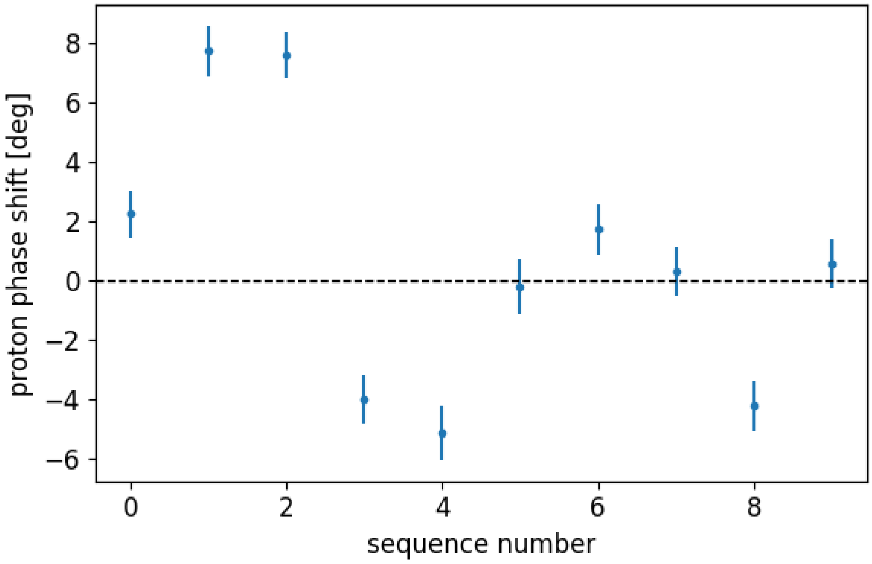

Figure 94: *Proton phase shift as a function of the sequence number. In principle the values should statistically fluctuate around the same value. If no exotic interaction was present they should fluctuate around zero (dashed line).*

for each interaction range λ

$$\varphi_0 = \Delta\varphi \times e^{\Delta x/\lambda} \ . \tag{56}$$

Figure 95 illustrates the exponential function through the measured phase shift. As an example, for $\lambda = 2$ mm and $\lambda = 10$ mm it results in a value of $\varphi_0 = 0.0° \pm 5.8°$ and $\varphi_0 = 0.0° \pm 1.4°$, respectively. These values correspond to the y-intercept of the exponential curves.

To calculate the upper limit of the coupling coefficient at 95% confidence level (C.L.) we can use Eqs. (54) and (56) for each λ to get

$$f_\perp < \frac{1}{2}\frac{2m_p c}{Nl\hbar}\frac{1}{\lambda}\left(|\varphi_0| + 1.96 \cdot \sigma_{\varphi_0}\right) \ , \tag{57}$$

where the additional factor of $1/2$ is due to the fact that we calculated the phase shift from the difference of the measurements on both sides and σ_{φ_0} is the uncertainty of φ_0. This leads to the projected exclusion sensitivity for a measurement precision of $1.0°$ presented in Fig. 96. Sensitivity projections for a phase precision of $0.3°$ and $0.1°$ are also shown.

Most experiments actually do not present their measured constraint on $f_\perp$ but on the coupling constant g_A^2. However, this can be misleading since it includes certain assumptions that are often not stated. As mentioned above, the coupling constants $g_{A,V}$ may be different

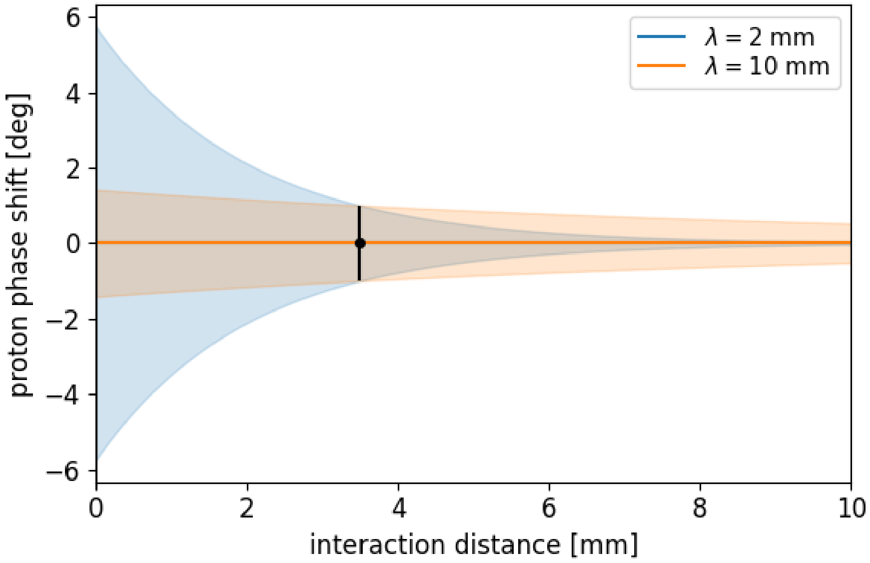

Figure 95: *Two examples of the exponential function that goes through the phase shift* $\Delta\varphi = 0° \pm 1°$ *(black) for* $\lambda = 2\ \mathrm{mm}$ *(blue) and* $\lambda = 10\ \mathrm{mm}$ *(orange) as as a function of the interaction distance. The values of* φ_0 *correspond to the* y*-intercept.*

for all fermions. Usually it is assumed that the coupling to electrons is zero, i.e., $g^e_{A,V} = 0$. It is further assumed that the coupling to protons and neutrons is identical, i.e., $g^p_{A,V} = g^n_{A,V} =: g^{\mathcal{N}}_{A,V}$. The same or similar assumptions may apply for experiments measuring the scalar or pseudo-scalar coupling $g_{S,P}$. Under these assumptions, only the coupling constant for the nucleons $g^{\mathcal{N}}_{A,V}$ is left. We therefore omit the superscript $\mathcal{N}$ in the rest of the document.

The Seattle torsion pendulum experiment constrained the vector coupling constant to $g_V^2 < 5 \times 10^{-40}$ [160]. This value is more then twenty orders of magnitude smaller than our projected sensitivity of g_A^2. The first term of Eq. (52) is, therefore, negligible. Additionally, the third term of Eq. (52) is suppressed by some mass scale $1/M^2$ and can therefore be assumed to be negligible too. Using further that $m_p/m_{\mathcal{N}} \approx 1$, the term for the coupling coefficient Eq. (52) can be simplified to $g_A^2 = 2f_\perp$.

The same way as in Eq. (57), the upper limit of the coupling at 95% C.L. can be calculated for each λ using

$$g_a^2 < \frac{1}{2}\frac{4m_p c}{Nl\hbar}\frac{1}{\lambda}\left(|\varphi_0| + 1.96 \cdot \sigma_{\varphi_0}\right) \ . \tag{58}$$

This leads to a projected sensitivity that is presented in Fig. 97 together with constraints set by other experiments.

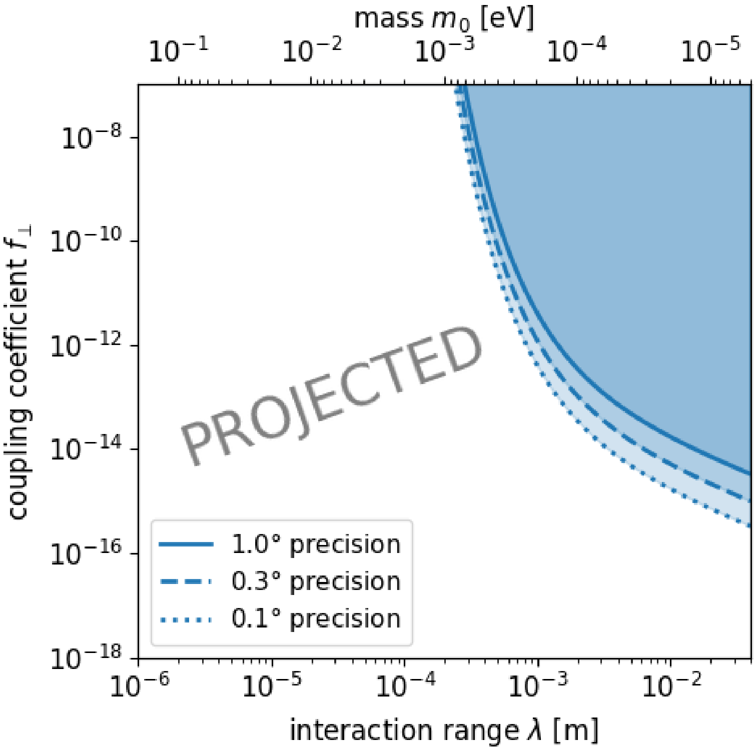

Figure 96: *Projected sensitivity on the coupling coefficient* $f_\perp$ *(*95% *C.L.) as a function of the interaction range and the mass of a new vector boson for various precisions of the measured proton phase shift. The precision of* 1.0° *can be achieved with a single measurement and the precision of* 0.1° *in* 24 *hours of data taking.*

The sensitivity projections of this measurement in Figs. 96 and 97 are for the coupling between the probe protons and a copper sample. We intend to use protons for the first time in a measurement of the axial-vector coupling constant g_A^2. A direct comparison to the other measurements in Fig. 97 where the probe particles were neutrons can only be done under the assumption of $g^p_{A,V} = g^n_{A,V}$.

For an interaction distance of approximately $10\ \mathrm{mm}$, the sensitivity is on the same order as the measurement of ETHZ [61]. At shorter distances our constraint is much weaker. The reason is that in this measurement, the separation between the probe particles and the sample is $3.5\ \mathrm{mm}$ whereas it was only $0.57\ \mathrm{mm}$ in the ETHZ measurement. They used free

---

[5] There seems to be a mistake of the limit by a factor of four in the publication. Here we show the corrected limit.

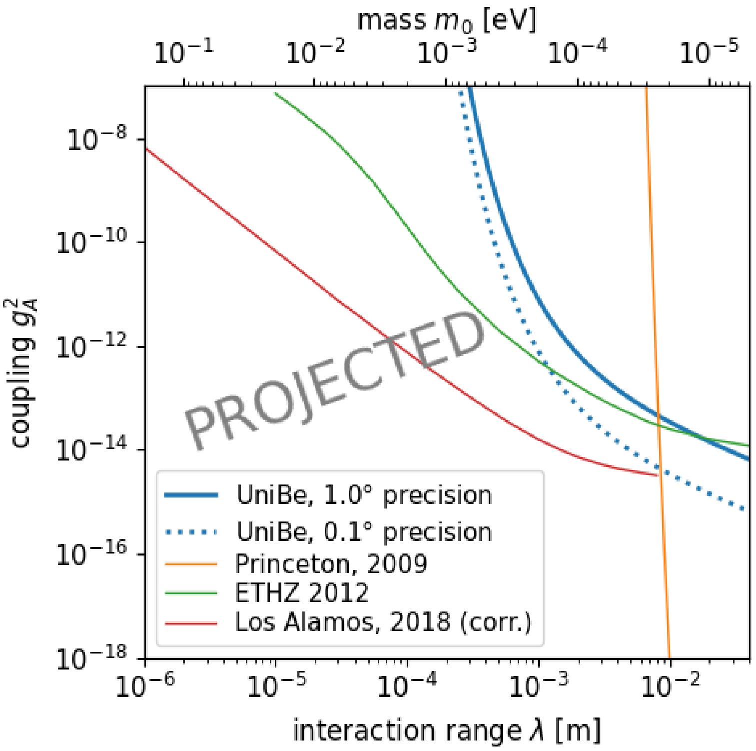

Figure 97: *Limits on the axial-axial coupling* g_A^2 $(95\%$ *C.L.) as a function of the interaction range and the mass of a new vector boson. The solid blue line corresponds to the projected sensitivity of a single measurement and dotted blue line is the projected sensitivity for* 24 *hours of measurement. It is the only measurement where the probe particle is a proton. The other measurements of Princeton (orange) [161], ETHZ (green) [61], and Los Alamos (red) [164] all used neutrons as a probe particles.*[s]

neutrons in air and could put the copper sample much closer to the probe beam compared to the water setup where a glass capillary has to be use to guide the water.

The sensitivity of an exotic measurement can be expected to be better by an order of magnitude for 24 hours of measurement. We assumed that the uncertainty of the phase of a single measurement is the same. The systematic effects have to be under control. This can be achieved with an upgrade to two water pipes to measure the exotic interaction and the reference at the same time. Additionally, the mechanics should be built such that the interior is not supported by the mu-metal shield but mechanically isolated.

13 Summary

In summary, we described in detail the experimental *Proton NMR* apparatus that we developed and build. The setup applies Ramsey's method to the proton spins of the hydrogen atoms in the water. We described each element in detail. This includes the polarizer that creates a sizable polarization of the protons spins, the interaction zone that is magnetically shielded in mu-metal and where the spins are manipulated by various fields, and the NMR system that allows to analyze and measure the spin polarization after the interaction. We used the well-understood resonance measurements of Rabi and Ramsey to characterize the sensitivity and stability of the setup. A Ramsey-type setup could for example be used as a magnetometer of the *Beam EDM* apparatus. In such a scenario, multiple glass capillaries could sense the average magnetic field through the setup and be part of a magnetic field stabilization feedback loop. We also investigated the Bloch-Siegert effect which shifts the resonance frequency at higher amplitudes of the oscillating field. We tested ways to compensate it. Even though the compensation worked, it does not fully agree with the expected values from theory. Besides, we measured for the first time the dressed spin states of protons. They can change the gyromagnetic ratio of a particle which can be used to reduce systematic effects in magnetic field measurements. We developed a qualitative approach in a semi-classical framework to understand the enhancement of the gyromagnetic ratio. Finally, we also tried to measure a new Yukawa-like interaction in the millimeter interaction range. Even though the setup is not yet in a stage to perform a full exotic measurement, we showed how the procedure works and projected the sensitivity of a single measurement and 24 hours of data taking. The planned upgrade containing two water pipes through the setup to simultaneously sense the exotic interaction and the background field will allow to compensate for magnetic field drifts. The setup could also be placed inside the magnetically shielded room that is currently being built in our laboratory in Bern. Together with other improvements, such as a control or stabilization of the room temperature or magnetic field probes between the spin-flip coils would allow to search for this new Yukawa-like interaction.

14 Acknowledgements

First, I thank Florian for giving me the Ph.D. position in his group. I really like the work in the low-energy particle physics field. You gave me great opportunities and a lot of freedom to implement my ideas. It was so much fun working together and solving problems in many vivid discussions. I am overwhelmed by how much time you spend with people from the group to push everyone to their best. It was also fun to see how often you came to my office to discuss something or wanted to go for a coffee when you had to write funding proposals or read reports. I am really grateful for everything.

I thank Gilberto and Dieter for agreeing to be experts on my Ph.D. and my defense. It takes a lot of time to read a thesis, attend the exam, and evaluate it. I do not take this effort for granted that you invested without getting much back.

A lot of my work may have been possible but certainly much less fun without all the *Fundamental Neutron and Precision Physics Group* members. Was it at a beam time at the Institut Laue-Langevin (ILL), where we all were at our limit at some point, in all the discussions during lunch, or any other debate, I really enjoyed working with you. So thank you, Alex, Anastasio, Andreas, Andrew, Ciro, Estelle, Florian, Gjon, Ivan, Jacob, Julia, Marc 1, Marc 2, Moritz, Oliver, Pascal, Philipp, Severin, and Zach.[t]

I also thank Torsten for all the invaluable advice and suggestions. Quite often, we thought we had a reasonable decision on something, you told us your opinion and thoughts, and mostly you were right, and we had to reevaluate. This helped me a lot to improve my scientific thinking, and I am thankful for that.

I am also grateful to all the people I worked with at the University besides my group, starting with Roger, Jan, Silas, Lorenzo, Camilla, and Pascal from the mechanical and electronics workshop and Marco and Gianfranco from the IT. Then all the other people from LHEP, especially Ursula and Marcella, for all the administrative work and the many funny coffee breaks. You all played an essential role for me and my work.

During the first few months of my Ph.D., I had to get to know NMR techniques for building the *Proton NMR* setup. I was sent to Patrick at the Paul Scherrer Institut (PSI), who explained everything and gave me many tricks. You were always available when I had questions and still now are offering help to read the technical content of my NMR-related publications. Thank you for all that.

---

[t] alphabetic order

A big thank goes to Aldo. You are the reason why I started to love experimental particle physics in the field we are working. You inspired me with your passion, and I really hope that we can work together again in some way in the future.

A special thank goes to Oliver Zimmer. You were my savior in distress at our beamtime at the ILL in 2020. You organized and provided an alternative high-voltage power supply essential for my search for axions and axion-like particles.

Some of the most important to thank is my family. First of all, I thank my parents, Thomas and Christa. When asking who was ultimately responsible that I could end up here, the answer is always you. You supported me my whole life and are one of the main reasons for who I am now. My sister, Renée, is also very important to me. Because of how we live together, I always like to come home because I can enjoy being alone if needed, but there is always somebody to talk to, at least when you are around. Then I thank Christoph. You are the one to ask me about what contains the universe, and we can spend evenings discussing it. You have brought me further in life by reflecting on me and giving me the input to think about myself and how I want to be. This is invaluable. I also thank Anja for being part of my life. You made the time in the home office during the second COVID-19 lockdown fun, and I enjoyed spending time with you. You understand how science works, and I like to discuss it with you. Thank you all. I love you very much.

I also thank Rafaela and Fernanda. Besides being good friends and very important to me, you both helped me in the last stage of this work by giving me final remarks on the overall content and the English.

Besides everybody mentioned above, many people around me helped, supported, and motivated me in one way or another. You are too many to say you all but be sure I did not forget you. Next time we meet, I will for sure tell you.

Last, this work was supported via the European Research Council under the ERC Grant Agreement no. 715031 (BEAM-EDM) and via the Swiss National Science Foundation under grants no. PP00P2-163663 and 200021-181996.

References

1. Boucenna, S. M. & Morisi, S. Theories relating baryon asymmetry and dark matter. *Frontiers in Physics* **1.** doi:10.3389/fphy.2013.00033 (2014).
2. Chadha-Day, F., Ellis, J. & Marsh, D. J. E. Axion dark matter: What is it and why now? *Science Advances* **8,** eabj3618. doi:10.1126/sciadv.abj3618 (2022).
3. Schulthess, I., Chanel, E., Fratangelo, A., Gottstein, A., Gsponer, A., Hodge, Z., Pistillo, C., Ries, D., Soldner, T., Thorne, J., *et al. New Limit on Axion-Dark-Matter using Cold Neutrons* arXiv: 2204.01454. 2022. doi:10.48550/arXiv.2204.01454.
4. Peccei, R. D. & Quinn, H. R. CP Conservation in the Presence of Pseudoparticles. *Physical Review Letters* **38,** 1440–1443. doi:10.1103/PhysRevLett.38.1440 (1977).
5. Peccei, R. D. & Quinn, H. R. Constraints imposed by CP conservation in the presence of pseudoparticles. *Physical Review D* **16,** 1791–1797. doi:10.1103/PhysRevD.16.1791 (1977).
6. Weinberg, S. A New Light Boson? *Physical Review Letters* **40,** 223–226. doi:10.1103/PhysRevLett.40.223 (1978).
7. Wilczek, F. Problem of Strong P and T Invariance in the Presence of Instantons. *Physical Review Letters* **40,** 279–282. doi:10.1103/PhysRevLett.40.279 (1978).
8. Pospelov, M. & Ritz, A. Theta-Induced Electric Dipole Moment of the Neutron via QCD Sum Rules. *arXiv:hep-ph/9904483.* arXiv: hep-ph/9904483. doi:10.1103/PhysRevLett.83.2526 (1999).
9. Pospelov, M. & Ritz, A. Theta vacua, QCD sum rules, and the neutron electric dipole moment. *Nuclear Physics B* **573,** 177–200. doi:10.1016/S0550-3213(99)00817-2 (2000).
10. Abel, C., Afach, S., Ayres, N. J., Baker, C. A., Ban, G., Bison, G., Bodek, K., Bondar, V., Burghoff, M., Chanel, E., *et al.* Measurement of the permanent electric dipole moment of the neutron. *arXiv:2001.11966 [hep-ex, physics:nucl-ex, physics:physics].* arXiv: 2001.11966 (2020).
11. Dine, M., Fischler, W. & Srednicki, M. A simple solution to the strong CP problem with a harmless axion. *Physics Letters B* **104,** 199–202. doi:10.1016/0370-2693(81)90590-6 (1981).

12. Zhitnitskii, A. P. Possible suppression of axion-hadron interactions. *Sov. J. Nucl. Phys. (Engl. Transl.); (United States)* **31:2** (1980).

13. Kim, J. E. Weak-Interaction Singlet and Strong CP Invariance. *Physical Review Letters* **43,** 103–107. doi:`10.1103/PhysRevLett.43.103` (1979).

14. Shifman, M. A., Vainshtein, A. I. & Zakharov, V. I. Can confinement ensure natural CP invariance of strong interactions? *Nuclear Physics B* **166,** 493–506. doi:`10.1016/0550-3213(80)90209-6` (1980).

15. Peccei, R. D. The Strong CP Problem and Axions. *arXiv:hep-ph/0607268* **741.** arXiv: hep-ph/0607268, 3–17. doi:`10.1007/978-3-540-73518-2_1` (2008).

16. Gorghetto, M. & Villadoro, G. Topological susceptibility and QCD axion mass: QED and NNLO corrections. *Journal of High Energy Physics* **2019,** 33. doi:`10.1007/JHEP03(2019)033` (2019).

17. Hook, A. Solving the Hierarchy Problem Discretely. *Physical Review Letters* **120,** 261802. doi:`10.1103/PhysRevLett.120.261802` (2018).

18. Di Luzio, L., Gavela, B., Quilez, P. & Ringwald, A. Dark matter from an even lighter QCD axion: trapped misalignment. *Journal of Cosmology and Astroparticle Physics* **2021,** 001. doi:`10.1088/1475-7516/2021/10/001` (2021).

19. Di Luzio, L., Gavela, B., Quilez, P. & Ringwald, A. An even lighter QCD axion. *Journal of High Energy Physics* **2021,** 184. doi:`10.1007/JHEP05(2021)184` (2021).

20. Planck Collaboration, Aghanim, N., Akrami, Y., Arroja, F., Ashdown, M., Aumont, J., Baccigalupi, C., Ballardini, M., Banday, A. J., Barreiro, R. B., *et al.* Planck 2018 results: I. Overview and the cosmological legacy of Planck. *Astronomy & Astrophysics* **641,** A1. doi:`10.1051/0004-6361/201833880` (2020).

21. Preskill, J., Wise, M. B. & Wilczek, F. Cosmology of the invisible axion. *Physics Letters B* **120,** 127–132. doi:`10.1016/0370-2693(83)90637-8` (1983).

22. Abbott, L. & Sikivie, P. A cosmological bound on the invisible axion. *Physics Letters B* **120,** 133–136. doi:`10.1016/0370-2693(83)90638-X` (1983).

23. Dine, M. & Fischler, W. The not-so-harmless axion. *Physics Letters B* **120,** 137–141. doi:`10.1016/0370-2693(83)90639-1` (1983).

24. Kim, J. E. Light pseudoscalars, particle physics and cosmology. *Physics Reports* **150,** 1–177. doi:`10.1016/0370-1573(87)90017-2` (1987).

25. Hwang, J.-c. & Noh, H. Axion as a cold dark matter candidate. *Physics Letters B* **680,** 1–3. doi:`10.1016/j.physletb.2009.08.031` (2009).

26. Domcke, V., Harling, B. v., Morgante, E. & Mukaida, K. Baryogenesis from axion inflation. *Journal of Cosmology and Astroparticle Physics* **2019,** 032–032. doi:10.1088/1475-7516/2019/10/032 (2019).

27. Co, R. T. & Harigaya, K. Axiogenesis. *Physical Review Letters* **124,** 111602. doi:10.1103/PhysRevLett.124.111602 (2020).

28. Dolan, M. J., Ferber, T., Hearty, C., Kahlhoefer, F. & Schmidt-Hoberg, K. Revised constraints and Belle II sensitivity for visible and invisible axion-like particles. *Journal of High Energy Physics* **2017,** 94. doi:10.1007/JHEP12(2017)094 (2017).

29. Curtin, D., Drewes, M., McCullough, M., Meade, P., Mohapatra, R. N., Shelton, J., Shuve, B., Accomando, E., Alpigiani, C., Antusch, S., *et al.* Long-lived particles at the energy frontier: the MATHUSLA physics case. *Reports on Progress in Physics* **82,** 116201. doi:10.1088/1361-6633/ab28d6 (2019).

30. Stadnik, Y. V. & Flambaum, V. V. Axion-induced effects in atoms, molecules, and nuclei: Parity nonconservation, anapole moments, electric dipole moments, and spin-gravity and spin-axion momentum couplings. *Physical Review D* **89,** 043522. doi:10.1103/PhysRevD.89.043522 (2014).

31. Particle Data Group, Zyla, P. A., Barnett, R. M., Beringer, J., Dahl, O., Dwyer, D. A., Groom, D. E., Lin, C. .-., Lugovsky, K. S., Pianori, E., *et al.* Review of Particle Physics. *Progress of Theoretical and Experimental Physics* **2020,** 083C01. doi:10.1093/ptep/ptaa104 (2020).

32. O'Hare, C. *cajohare/AxionLimits: AxionLimits* Version Number: v1.0. 2020. doi:10.5281/zenodo.3932430.

33. Dafni, T. & Iguaz Gutierrez, F. J. Axion helioscopes update: the status of CAST and IAXO. *PoS* **TIPP2014.** arXiv: 1501.01456, 130. doi:10.22323/1.213.0130 (2015).

34. Braine, T., Cervantes, R., Crisosto, N., Du, N., Kimes, S., Rosenberg, L. J., Rybka, G., Yang, J., Bowring, D., Chou, A. S., *et al.* Extended Search for the Invisible Axion with the Axion Dark Matter Experiment. *Physical Review Letters* **124,** 101303. doi:10.1103/PhysRevLett.124.101303 (2020).

35. Bähre, R., Döbrich, B., Dreyling-Eschweiler, J., Ghazaryan, S., Hodajerdi, R., Horns, D., Januschek, F., Knabbe, E. .-., Lindner, A., Notz, D., *et al.* Any light particle search II — Technical Design Report. *Journal of Instrumentation* **8,** T09001–T09001. doi:10.1088/1748-0221/8/09/T09001 (2013).

36. Abudinén, F., Adachi, I., Aihara, H., Akopov, N., Aloisio, A., Ameli, F., Anh Ky, N., Asner, D. M., Aushev, T., Aushev, V., *et al.* Search for Axionlike Particles Produced in e + e − Collisions at Belle II. *Physical Review Letters* **125,** 161806. doi:10.1103/PhysRevLett.125.161806 (2020).
37. Primakoff, H. Photo-Production of Neutral Mesons in Nuclear Electric Fields and the Mean Life of the Neutral Meson. *Physical Review* **81,** 899–899. doi:10.1103/PhysRev.81.899 (1951).
38. Gil, E. C., Albarrán, E. M., Minucci, E., Nüssle, G., Padolski, S., Petrov, P., Szilasi, N., Velghe, B., Georgiev, G., Kozhuharov, V., *et al.* The beam and detector of the NA62 experiment at CERN. *Journal of Instrumentation* **12,** P05025–P05025. doi:10.1088/1748-0221/12/05/P05025 (2017).
39. Ariga, A., Ariga, T., Boyd, J., Cadoux, F., Casper, D. W., Favre, Y., Feng, J. L., Ferrere, D., Galon, I., Gonzalez-Sevilla, S., *et al.* FASER's physics reach for long-lived particles. *Physical Review D* **99,** 095011. doi:10.1103/PhysRevD.99.095011 (2019).
40. Beacham, J., Burrage, C., Curtin, D., De Roeck, A., Evans, J., Feng, J. L., Gatto, C., Gninenko, S., Hartin, A., Irastorza, I., *et al.* Physics beyond colliders at CERN: beyond the Standard Model working group report. *Journal of Physics G: Nuclear and Particle Physics* **47,** 010501. doi:10.1088/1361-6471/ab4cd2 (2020).
41. Aybas, D., Adam, J., Blumenthal, E., Gramolin, A. V., Johnson, D., Kleyheeg, A., Afach, S., Blanchard, J. W., Centers, G. P., Garcon, A., *et al.* Search for axion-like dark matter using solid-state nuclear magnetic resonance. *Physical Review Letters* **126.** arXiv: 2101.01241, 141802. doi:10.1103/PhysRevLett.126.141802 (2021).
42. Budker, D., Graham, P. W., Ledbetter, M., Rajendran, S. & Sushkov, A. O. Proposal for a Cosmic Axion Spin Precession Experiment (CASPEr). *Physical Review X* **4,** 021030. doi:10.1103/PhysRevX.4.021030 (2014).
43. Abel, C., Ayres, N. J., Ban, G., Bison, G., Bodek, K., Bondar, V., Daum, M., Fairbairn, M., Flambaum, V. V., Geltenbort, P., *et al.* Search for axion-like dark matter through nuclear spin precession in electric and magnetic fields. *Physical Review X* **7.** doi:10.1103/PhysRevX.7.041034 (2017).
44. Roussy, T. S., Palken, D. A., Cairncross, W. B., Brubaker, B. M., Gresh, D. N., Grau, M., Cossel, K. C., Ng, K. B., Shagam, Y., Zhou, Y., *et al.* Experimental Constraint on Axionlike Particles over Seven Orders of Magnitude in Mass. *Physical Review Letters* **126,** 171301. doi:10.1103/PhysRevLett.126.171301 (2021).

45. Chang, S. P., Hacıömeroğlu, S., Kim, O., Lee, S., Park, S. & Semertzidis, Y. K. Axionlike dark matter search using the storage ring EDM method. *Physical Review D* **99,** 083002. doi:10.1103/PhysRevD.99.083002 (2019).

46. Piegsa, F. M. New Concept for a Neutron Electric Dipole Moment Search using a Pulsed Beam. *Physical Review C* **88.** arXiv: 1309.1959. doi:10.1103/PhysRevC.88.045502 (2013).

47. Chanel, E., Hodge, Z., Ries, D., Schulthess, I., Solar, M., Soldner, T., Stalder, O., Thorne, J. & Piegsa, F. M. The pulsed neutron beam EDM experiment. *EPJ Web of Conferences* **219** (eds Jenke, T., Degenkolb, S., Geltenbort, P., Jentschel, M., Nesvizhevsky, V., Rebreyend, D., Roccia, S., Soldner, T., Stutz, A. & Zimmer, O.) 02004. doi:10.1051/epjconf/201921902004 (2019).

48. Corasaniti, P. S., Agarwal, S., Marsh, D. J. E. & Das, S. Constraints on dark matter scenarios from measurements of the galaxy luminosity function at high redshifts. *Physical Review D* **95,** 083512. doi:10.1103/PhysRevD.95.083512 (2017).

49. Pillepich, A., Kuhlen, M., Guedes, J. & Madau, P. THE DISTRIBUTION OF DARK MATTER IN THE MILKY WAY'S DISK. *The Astrophysical Journal,* 12 (2014).

50. Blum, K., D'Agnolo, R. T., Lisanti, M. & Safdi, B. R. Constraining axion dark matter with Big Bang Nucleosynthesis. *Physics Letters B* **737,** 30–33. doi:10.1016/j.physletb.2014.07.059 (2014).

51. Stadnik, Y. V. & Flambaum, V. V. Can Dark Matter Induce Cosmological Evolution of the Fundamental Constants of Nature? *Physical Review Letters* **115,** 201301. doi:10.1103/PhysRevLett.115.201301 (2015).

52. Pagliaroli, G., Vissani, F., Costantini, M. & Ianni, A. Improved analysis of SN1987A antineutrino events. *Astroparticle Physics* **31,** 163–176. doi:10.1016/j.astropartphys.2008.12.010 (2009).

53. Scholberg, K. Supernova Neutrino Detection. *Annual Review of Nuclear and Particle Science* **62.** _eprint: https://doi.org/10.1146/annurev-nucl-102711-095006, 81–103. doi:10.1146/annurev-nucl-102711-095006 (2012).

54. Graham, P. W. & Rajendran, S. New Observables for Direct Detection of Axion Dark Matter. *Physical Review D* **88,** 035023. doi:10.1103/PhysRevD.88.035023 (2013).

55. Chanel, E. G. A. *The BeamEDM experiment and the measurement of the neutron incoherent scattering length of 199Hg* PhD thesis (Universität Bern, 2021).

56. Ramsey, N. F. A New Molecular Beam Resonance Method. *Physical Review* **76,** 996–996. doi:10.1103/PhysRev.76.996 (1949).

57. Ramsey, N. F. A Molecular Beam Resonance Method with Separated Oscillating Fields. *Physical Review* **78,** 695–699. doi:`10.1103/PhysRev.78.695` (1950).

58. Essen, L. & Parry, J. V. L. An Atomic Standard of Frequency and Time Interval: A Cæsium Resonator. *Nature* **176,** 280–282. doi:`10.1038/176280a0` (1955).

59. Wynands, R. & Weyers, S. Atomic fountain clocks. *Metrologia* **42,** S64–S79. doi:`10.1088/0026-1394/42/3/S08` (2005).

60. Rosi, G., Sorrentino, F., Cacciapuoti, L., Prevedelli, M. & Tino, G. M. Precision measurement of the Newtonian gravitational constant using cold atoms. *Nature* **510,** 518–521. doi:`10.1038/nature13433` (2014).

61. Piegsa, F. & Pignol, G. Limits on the Axial Coupling Constant of New Light Bosons. *Physical Review Letters* **108.** arXiv: 1205.0340. doi:`10.1103/PhysRevLett.108.181801` (2012).

62. Abele, H., Dubbers, D., Häse, H., Klein, M., Knöpfler, A., Kreuz, M., Lauer, T., Märkisch, B., Mund, D., Nesvizhevsky, V., *et al.* Characterization of a ballistic supermirror neutron guide. *Nuclear Instruments and Methods in Physics Research Section A: Accelerators, Spectrometers, Detectors and Associated Equipment* **562,** 407–417. doi:`10.1016/j.nima.2006.03.020` (2006).

63. Petoukhov, A. K., Nesvizhevsky, V. V., Bigault, T., Courtois, P., Devishvili, A., Jullien, D. & Soldner, T. *Realization of an advanced super-mirror solid-state neutron polarizer for the instrument PF1B at the Institut Laue-Langevin* arXiv:2208.14305 [nucl-ex, physics:physics]. 2022.

64. Fermi, E., Marshall, J. & Marshall, L. A Thermal Neutron Velocity Selector and Its Application to the Measurement of the Cross Section of Boron. *Physical Review* **72,** 193–196. doi:`10.1103/PhysRev.72.193` (1947).

65. SENSYS GmbH. *Sensys FGM3D Datasheet* 2019.

66. Stefan Mayer Instruments. *Data Sheet FLC3-70* 2021.

67. Analog Devices, Inc. *AD5791 Datasheet* 2020.

68. Gsponer, A. *Characterization of the Magnetic Shielding for the Beam EDM Experiment* PhD thesis (Universität Bern, 2021).

69. Gottstein, A. *Passive Magnetic Shielding Characterisation for Static Fields with the BeamEDM Experiment* PhD thesis (Universität Bern, 2021).

70. Keysight Technologies. *Keysight 33500B and 33600A Series Trueform Waveform Generators* 2021.

71. denk-stein:net GmbH. *Smart, Low-Cost & High-PerformanceGPS & Rubidium Reference Source* 2013.
72. MONACOR INTERNATIONAL GmbH. *IMG Stageline STA-1000* 2012.
73. FuG Elektronik GmbH. *HIGH-VOLTAGE POWER SUPPLIES – HCP SERIES* 2021.
74. Klein, M. & Schmidt, C. J. CASCADE, neutron detectors for highest count rates in combination with ASIC/FPGA based readout electronics. *Nuclear Instruments and Methods in Physics Research Section A: Accelerators, Spectrometers, Detectors and Associated Equipment* **628,** 9–18. doi:`10.1016/j.nima.2010.06.278` (2011).
75. PSI & TRIUMF. *MIDAS* 2020.
76. Brun, R. & Rademakers, F. ROOT — An object oriented data analysis framework. *Nuclear Instruments and Methods in Physics Research Section A: Accelerators, Spectrometers, Detectors and Associated Equipment* **389,** 81–86. doi:`10.1016/S0168-9002(97)00048-X` (1997).
77. Stephen Butterworth. On the Theory of Filter Amplifiers. *Experimental Wireless and the Wireless Engineer* **7,** 536–541 (1930).
78. Piegsa, F., van den Brandt, B., Glättli, H., Hautle, P., Kohlbrecher, J., Konter, J., Schlimme, B. & Zimmer, O. A Ramsey apparatus for the measurement of the incoherent neutron scattering length of the deuteron. *Nuclear Instruments and Methods in Physics Research Section A: Accelerators, Spectrometers, Detectors and Associated Equipment* **589,** 318–329. doi:`10.1016/j.nima.2008.02.020` (2008).
79. Piegsa, F. M. A neutron resonance spin flip device for sub-millitesla magnetic fields. *Nuclear Instruments and Methods in Physics Research Section A: Accelerators, Spectrometers, Detectors and Associated Equipment* **786,** 71–77. doi:`10.1016/j.nima.2015.03.018` (2015).
80. Calic, I. *Precision magnetometry using Rb-atomic magnetometers and oscillating neutron Ramsey Method: Producing fake axion fields at the NARZISS beamline* PhD thesis (Universität Bern, 2022).
81. Kepco, Inc. *Kepco's BOP Family Of Four Quadrant Bipolar Power Supplies / Amplifiers* 2011.
82. Graham, M. J., Drake, A. J., Djorgovski, S. G., Mahabal, A. A., Donalek, C., Duan, V. & Maher, A. A comparison of period finding algorithms. *Monthly Notices of the Royal Astronomical Society* **434.** arXiv: 1307.2209, 3423–3444. doi:`10.1093/mnras/stt1264` (2013).

83. Lomb, N. R. Least-squares frequency analysis of unequally spaced data. *Astrophysics and Space Science* **39,** 447–462. doi:`10.1007/BF00648343` (1976).

84. Zechmeister, M. & Kürster, M. The generalised Lomb-Scargle periodogram: A new formalism for the floating-mean and Keplerian periodograms. *Astronomy & Astrophysics* **496,** 577–584. doi:`10.1051/0004-6361:200811296` (2009).

85. Press, W. H. & Rybicki, G. B. Fast algorithm for spectral analysis of unevenly sampled data. *The Astrophysical Journal* **338,** 277. doi:`10.1086/167197` (1989).

86. VanderPlas, J. T. Understanding the Lomb–Scargle Periodogram. *The Astrophysical Journal Supplement Series* **236,** 16. doi:`10.3847/1538-4365/aab766` (2018).

87. The Astropy Collaboration, Robitaille, T. P., Tollerud, E. J., Greenfield, P., Droettboom, M., Bray, E., Aldcroft, T., Davis, M., Ginsburg, A., Price-Whelan, A. M., *et al.* Astropy: A community Python package for astronomy. *Astronomy & Astrophysics* **558,** A33. doi:`10.1051/0004-6361/201322068` (2013).

88. The Astropy Collaboration, Price-Whelan, A. M., Sipőcz, B. M., Günther, H. M., Lim, P. L., Crawford, S. M., Conseil, S., Shupe, D. L., Craig, M. W., Dencheva, N., *et al.* The Astropy Project: Building an Open-science Project and Status of the v2.0 Core Package. *The Astronomical Journal* **156,** 123. doi:`10.3847/1538-3881/aabc4f` (2018).

89. Bradley, L., Shupe, D. L., Patil, A. A., Corrales, L., Brasseur, C. E., Nöthe, M., Donath, A., Tollerud, E., Morris, B. M., Ginsburg, A., *et al.* The Astropy Project: Sustaining and Growing a Community-oriented Open-source Project and the Latest Major Release (v5.0) of the Core Package. *The Astrophysical Journal,* 20 (2022).

90. Piegsa, F. M., Chanel, E., Fratangelo, A., Gottstein, A., Gsponer, A., Hodge, Z., Pistillo, C., Schulthess, I., Solar, M., Soldner, T., *et al.* New Neutron Electric Dipole Moment Search using a Pulsed Beam. *Institut Laue-Langevin (ILL).* doi:`doi:10.5291/ILL-DATA.3-07-393` (2020).

91. Foster, J. W., Rodd, N. L. & Safdi, B. R. Revealing the dark matter halo with axion direct detection. *Physical Review D* **97,** 123006. doi:`10.1103/PhysRevD.97.123006` (2018).

92. Centers, G. P., Blanchard, J. W., Conrad, J., Figueroa, N. L., Garcon, A., Gramolin, A. V., Kimball, D. F. J., Lawson, M., Pelssers, B., Smiga, J. A., *et al.* Stochastic fluctuations of bosonic dark matter. *Nature Communications* **12,** 7321. doi:`10.1038/s41467-021-27632-7` (2021).

93. Weber, M. & de Boer, W. Determination of the local dark matter density in our Galaxy. *Astronomy & Astrophysics* **509,** A25 (2010).

94. Catena, R. & Ullio, P. A novel determination of the local dark matter density. *Journal of Cosmology and Astroparticle Physics* **2010,** 004–004. doi:`10.1088/1475-7516/2010/08/004` (2010).

95. Garcon, A., Blanchard, J. W., Centers, G. P., Figueroa, N. L., Graham, P. W., Jackson Kimball, D. F., Rajendran, S., Sushkov, A. O., Stadnik, Y. V., Wickenbrock, A., *et al.* Constraints on bosonic dark matter from ultralow-field nuclear magnetic resonance. *Science Advances* **5,** eaax4539. doi:`10.1126/sciadv.aax4539` (2019).

96. Raffelt, G. G. Astrophysical methods to constrain axions and other novel particle phenomena. *Physics Reports* **198,** 1–113. doi:`10.1016/0370-1573(90)90054-6` (1990).

97. Savitzky, A. & Golay, M. J. E. Smoothing and Differentiation of Data by Simplified Least Squares Procedures. *Analytical Chemistry* **36,** 1627–1639. doi:`10.1021/ac60214a047` (1964).

98. Greene, G. L., Ramsey, N. F., Mampe, W., Pendlebury, J. M., Smith, K., Dress, W. B., Miller, P. D. & Perrin, P. Measurement of the neutron magnetic moment. *Physical Review D* **20,** 2139–2153. doi:`10.1103/PhysRevD.20.2139` (1979).

99. Sherman, C. Nuclear Induction with Separate Regions of Excitation and Detection. *Physical Review* **93,** 1429–1430. doi:`10.1103/PhysRev.93.1429` (1954).

100. Antoniadis, I., Baessler, S., Büchner, M., Fedorov, V., Hoedl, S., Lambrecht, A., Nesvizhevsky, V., Pignol, G., Protasov, K., Reynaud, S., *et al.* Short-range fundamental forces. *Comptes Rendus Physique* **12,** 755–778. doi:`10.1016/j.crhy.2011.05.004` (2011).

101. Smits, J. *Developments towards a proton-NMR Ramsey apparatus* PhD thesis (Unibersität Bern, 2020).

102. TCS Micropumps ltd. *MGD2000 Data Sheet* 2021.

103. Reynolds Osborne. XXIX. An experimental investigation of the circumstances which determine whether the motion of water shall be direct or sinuous, and of the law of resistance in parallel channels. *Philosophical Transactions of the Royal Society of London* **174,** 935–982. doi:`10.1098/rstl.1883.0029` (1883).

104. Haynes, W. M., Haynes, W. M., Lide, D. R. & Bruno, T. J. *CRC handbook of chemistry and physics: a ready-reference book of chemical and physical data.* OCLC: 1097136026 (CRC Press, 2017).

105. Rotta, J. in *Ingenieur-Archiv* 258 (Springer-Verlag, 1956).

106. Afzal, N., Seena, A. & Bushra, A. Power Law Velocity Profile in Fully Developed Turbulent Pipe and Channel Flows. *Journal of Hydraulic Engineering* **133,** 1080–1086. doi:`10.1061/(ASCE)0733-9429(2007)133:9(1080)` (2007).

107. Sutera, S. P. & Skalak, R. The History of Poiseuille's Law. *Annual Review of Fluid Mechanics* **25,** 1–20. doi:`10.1146/annurev.fl.25.010193.000245` (1993).

108. Brown, G. O. *The History of the Darcy-Weisbach Equation for Pipe Flow Resistance* in *Environmental and Water Resources History* (American Society of Civil Engineers, Washington, D.C., United States, 2002), 34–43. doi:`10.1061/40650(2003)4`.

109. Thermo Fisher Scientific. *Thermo Scientific Manual* 2015.

110. Bloch, F. Nuclear Induction. *Physical Review* **70,** 460–474. doi:`10.1103/PhysRev.70.460` (1946).

111. Hahn, E. L. An Accurate Nuclear Magnetic Resonance Method for Measuring Spin-Lattice Relaxation Times. *Physical Review* **76,** 145–146. doi:`10.1103/PhysRev.76.145` (1949).

112. Supermagnete. *Datenblatt Artikel Q-40-10-05-N* 2018.

113. David Meeker. *Finite Element Method Magnetics* 2019.

114. Magnet-Physik Dr. Steingroever GmbH. *USB Hall-Sonden* 2020.

115. Keysight Technologies. *Keysight B2961A/B2962A 6.5 Digit Low Noise Power Source* 2020.

116. Hahn, E. L. Spin Echoes. *Physical Review* **80,** 580–594. doi:`10.1103/PhysRev.80.580` (1950).

117. Mini-Circuits. *Coaxial Power Splitter/Combiner ZFRSC-2050+* 2008.

118. Pico Technology. *TC-08 Data Logger* 2021.

119. National Instruments Corporation. *PCI/PXI/USB-6289 Specifications* 2022.

120. SpinCore Technologies, Inc. *iSpin-NMR™ Owner's Manual* 2017.

121. SpinCore Technologies, Inc. *NMR Permanent Magnets* 2022.

122. Tiesinga, E., Mohr, P. J., Newell, D. B. & Taylor, B. N. CODATA recommended values of the fundamental physical constants: 2018. *Reviews of Modern Physics* **93,** 025010. doi:`10.1103/RevModPhys.93.025010` (2021).

123. Bunting Magnetics Europe. *BREMAG NdFeB Standard Range* 2017.

124. Kim, S. & Doose, C. *Temperature compensation of NdFeB permanent magnets* in *Proceedings of the 1997 Particle Accelerator Conference (Cat. No.97CH36167)* **3** (IEEE, Vancouver, BC, Canada, 1998), 3227–3229. doi:10.1109/PAC.1997.753163.

125. Keeler, J. *Understanding NMR Spectroscopy* (University of Cambridge, Department of Chemistry, 2002).

126. Heideman, M. T., Johnson, D. H. & Burrus, C. S. Gauss and the history of the fast Fourier transform. *Archive for History of Exact Sciences* **34,** 265–277. doi:10.1007/BF00348431 (1985).

127. Craig, E. C. & Marshall, A. G. Automated phase correction of FT NMR spectra by means of phase measurement based on dispersion versus absorption relation (DISPA). *Journal of Magnetic Resonance (1969)* **76,** 458–475. doi:10.1016/0022-2364(88)90350-2 (1988).

128. Chen, L., Weng, Z., Goh, L. & Garland, M. An efficient algorithm for automatic phase correction of NMR spectra based on entropy minimization. *Journal of Magnetic Resonance* **158,** 164–168. doi:10.1016/S1090-7807(02)00069-1 (2002).

129. Bao, Q., Feng, J., Chen, L., Chen, F., Liu, Z., Jiang, B. & Liu, C. A robust automatic phase correction method for signal dense spectra. *Journal of Magnetic Resonance* **234,** 82–89. doi:10.1016/j.jmr.2013.06.012 (2013).

130. Bakhmutov, V. I. *Practical NMR relaxation for chemists* (Wiley, Chichester, West Sussex, England ; Hoboken, NJ, 2004).

131. Carr, H. Y. & Purcell, E. M. Effects of Diffusion on Free Precession in Nuclear Magnetic Resonance Experiments. *Physical Review* **94,** 630–638. doi:10.1103/PhysRev.94.630 (1954).

132. Meiboom, S. & Gill, D. Modified Spin-Echo Method for Measuring Nuclear Relaxation Times. *Review of Scientific Instruments* **29,** 688–691. doi:10.1063/1.1716296 (1958).

133. Henoumont, C., Laurent, S. & Vander Elst, L. How to perform accurate and reliable measurements of longitudinal and transverse relaxation times of MRI contrast media in aqueous solutions. *Contrast Media & Molecular Imaging* **4,** 312–321. doi:10.1002/cmmi.294 (2009).

134. Allan, D. Statistics of atomic frequency standards. *Proceedings of the IEEE* **54,** 221–230. doi:10.1109/PROC.1966.4634 (1966).

135. Howe, D., Allan, D. & Barnes, J. *Properties of Signal Sources and Measurement Methods* in *Thirty Fifth Annual Frequency Control Symposium* (IEEE, 1981), 669–716. doi:10.1109/FREQ.1981.200541.

136. Bloch, F. & Siegert, A. Magnetic Resonance for Nonrotating Fields. *Physical Review* **57,** 522–527. doi:10.1103/PhysRev.57.522 (1940).

137. Greene, G. L. Observation of the Bloch-Siegert effect in the Ramsey separated-oscillatory-field technique. *Physical Review A* **18,** 1057–1059. doi:10.1103/PhysRevA.18.1057 (1978).

138. Code, R. F. & Ramsey, N. F. Molecular-Beam Magnetic Resonance Studies of HD and D 2. *Physical Review A* **4,** 1945–1959. doi:10.1103/PhysRevA.4.1945 (1971).

139. Cohen-Tannoudji, C. & Haroche, S. Absorption et diffusion de photons optiques par un atome en interaction avec des photons de radiofréquence. *Journal de Physique* **30,** 153–168. doi:10.1051/jphys:01969003002-3015300 (1969).

140. Jaynes, E. & Cummings, F. Comparison of quantum and semiclassical radiation theories with application to the beam maser. *Proceedings of the IEEE* **51,** 89–109. doi:10.1109/PROC.1963.1664 (1963).

141. Shore, B. W. & Knight, P. L. The Jaynes-Cummings Model, 44 (1993).

142. Muskat, E., Dubbers, D. & Schärpf, O. Dressed Neutrons. *Physical Review Letters* **58,** 2047–2050. doi:10.1103/PhysRevLett.58.2047 (1987).

143. Dubbers, D. The dressed neutron-antineutron system. *Nuclear Instruments and Methods in Physics Research Section A: Accelerators, Spectrometers, Detectors and Associated Equipment* **284,** 22–28. doi:10.1016/0168-9002(89)90241-6 (1989).

144. Esler, A., Peng, J. C., Chandler, D., Howell, D., Lamoreaux, S. K., Liu, C. Y. & Torgerson, J. R. Dressed spin of He 3. *Physical Review C* **76,** 051302. doi:10.1103/PhysRevC.76.051302 (2007).

145. Chu, P.-H., Esler, A. M., Peng, J. C., Beck, D. H., Chandler, D. E., Clayton, S., Hu, B.-Z., Ngan, S. Y., Sham, C. H., So, L. H., *et al.* Dressed spin of polarized 3 He in a cell. *Physical Review C* **84,** 022501. doi:10.1103/PhysRevC.84.022501 (2011).

146. Eckel, S., Lamoreaux, S. K., Hayden, M. E. & Ito, T. M. Time-dependent spin dressing using a 3 He atomic beam. *Physical Review A* **85,** 032124. doi:10.1103/PhysRevA.85.032124 (2012).

147. Golub, R. Neutron electric-dipole moment, ultracold neutrons and polarized 3He. *Physics Reports* **237,** 1–62. doi:10.1016/0370-1573(94)90084-1 (1994).

148. Swank, C. M., Webb, E. K., Liu, X. & Filippone, B. W. Spin-dressed relaxation and frequency shifts from field imperfections. *Physical Review A* **98,** 053414. doi:10.1103/PhysRevA.98.053414 (2018).

149. Bell, W. E. & Bloom, A. L. Optical Detection of Magnetic Resonance in Alkali Metal Vapor, 8 (1957).

150. Happer, W. & Tang, H. Spin-Exchange Shift and Narrowing of Magnetic Resonance Lines in Optically Pumped Alkali Vapors. *Physical Review Letters* **31,** 273–276. doi:10.1103/PhysRevLett.31.273 (1973).

151. Tierney, T. M., Holmes, N., Mellor, S., López, J. D., Roberts, G., Hill, R. M., Boto, E., Leggett, J., Shah, V., Brookes, M. J., *et al.* Optically pumped magnetometers: From quantum origins to multi-channel magnetoencephalography. *NeuroImage* **199,** 598–608. doi:10.1016/j.neuroimage.2019.05.063 (2019).

152. Benumof, R. Optical Pumping Theory and Experiments. *American Journal of Physics* **33,** 151–160. doi:10.1119/1.1971285 (1965).

153. Twinleaf LLC. *Twinleaf MS-2 Magnetic shield* 2022.

154. Dobrescu, B. A. & Mocioiu, I. Spin-dependent macroscopic forces from new particle exchange. *Journal of High Energy Physics* **2006,** 005–005. doi:10.1088/1126-6708/2006/11/005 (2006).

155. Fadeev, P., Stadnik, Y. V., Ficek, F., Kozlov, M. G., Flambaum, V. V. & Budker, D. Revisiting spin-dependent forces mediated by new bosons: Potentials in the coordinate-space representation for macroscopic- and atomic-scale experiments. *Physical Review A* **99,** 022113. doi:10.1103/PhysRevA.99.022113 (2019).

156. Appelquist, T., Dobrescu, B. A. & Hopper, A. R. Nonexotic neutral gauge bosons. *Physical Review D* **68,** 035012. doi:10.1103/PhysRevD.68.035012 (2003).

157. Heckel, B. R., Cramer, C. E., Cook, T. S., Adelberger, E. G., Schlamminger, S. & Schmidt, U. New C P -Violation and Preferred-Frame Tests with Polarized Electrons. *Physical Review Letters* **97,** 021603. doi:10.1103/PhysRevLett.97.021603 (2006).

158. Kapner, D. J., Cook, T. S., Adelberger, E. G., Gundlach, J. H., Heckel, B. R., Hoyle, C. D. & Swanson, H. E. Tests of the Gravitational Inverse-Square Law below the Dark-Energy Length Scale. *Physical Review Letters* **98,** 021101. doi:10.1103/PhysRevLett.98.021101 (2007).

159. Nesvizhevsky, V. V., Pignol, G. & Protasov, K. V. Neutron scattering and extra-short-range interactions. *Physical Review D* **77,** 034020. doi:10.1103/PhysRevD.77.034020 (2008).

160. Adelberger, E., Gundlach, J., Heckel, B., Hoedl, S. & Schlamminger, S. Torsion balance experiments: A low-energy frontier of particle physics. *Progress in Particle and Nuclear Physics* **62,** 102–134. doi:`10.1016/j.ppnp.2008.08.002` (2009).

161. Vasilakis, G., Brown, J. M., Kornack, T. W. & Romalis, M. V. Limits on New Long Range Nuclear Spin-Dependent Forces Set with a K − He 3 Comagnetometer. *Physical Review Letters* **103,** 261801. doi:`10.1103/PhysRevLett.103.261801` (2009).

162. Heckel, B. R., Terrano, W. A. & Adelberger, E. G. Limits on Exotic Long-Range Spin-Spin Interactions of Electrons. *Physical Review Letters* **111,** 151802. doi:`10.1103/PhysRevLett.111.151802` (2013).

163. Yan, H. & Snow, W. M. New Limit on Possible Long-Range Parity-Odd Interactions of the Neutron from Neutron-Spin Rotation in Liquid He 4. *Physical Review Letters* **110,** 082003. doi:`10.1103/PhysRevLett.110.082003` (2013).

164. Haddock, C., Amadio, J., Anderson, E., Barrón-Palos, L., Crawford, B., Crawford, C., Esposito, D., Fox, W., Francis, I., Fry, J., *et al.* A search for possible long range spin dependent interactions of the neutron from exotic vector boson exchange. *Physics Letters B* **783,** 227–233. doi:`10.1016/j.physletb.2018.06.066` (2018).

165. Piegsa, F. M. & Pignol, G. A proposed search for new light bosons using a tabletop neutron Ramsey apparatus. *Journal of Physics: Conference Series* **340.** arXiv: 1111.1944, 012043. doi:`10.1088/1742-6596/340/1/012043` (2012).

166. Deutsches Kupferinstitut. *Cu-ETP* 2005.

167. Bork, J., Hahlbohm, H. & Klein, R. *The 8-layered magnetically shielded room of the PTB: Design and construction* 2001.

168. Verity Systems. *SV91M - A Security Approved Hard Drive & Tape Degausser* 2022.

Acronyms

AC alternating current. 25
ALP axion-like particle. 2–10, 14, 15, 17, 18, 21, 22, 24, 25, 28, 32–35, 38, 39, 43, 45–47, 49, 52–56

BBN Big Bang nucleosynthesis. 7, 54

C.L. confidence level. 2, 5, 52–54, 115–118
CAD computer-aided design. 63, 64, 108
CPMG Carr-Purcell-Meiboom-Gill. 76, 77

DAQ data acquisition system. 10, 18, 37
DC direct current. 25–27, 29, 39
DFSZ Dine-Fischler-Srednicki-Zhitnitsky. 3

EDM electric dipole moment. 2, 4, 6, 8, 9, 24, 45, 52, 54, 56
ESS European Spallation Source. 56
ETP electrolytic-tough pitch. 108

FFT fast Fourier transform. 45, 46, 73, 74
FID free induction decay. 71–73, 77
FWHM full width at half maximum. 36, 74, 75, 79, 80

GEM gas electron multiplier. 17

ILL Institut Laue-Langevin. 12, 19, 120, 121

KSVZ e Kim-Shifman-Vainshtein-Zakharov. 3

NMR nuclear magnetic resonance. 59, 60, 66–76, 119, 120

OPM optically pumped magnetometer. 95, 100, 101, 103, 104

POM polyoxymethylene. 13, 112
PSI Paul Scherrer Institut. 6, 18, 19, 24, 36, 40, 120
PTFE polytetrafluoroethylene. 60, 68, 69
PU polyurethane. 60
PVC polyvinylchlorid. 60

QCD quantum chromodynamics. 2, 3, 55

QED quantum electrodynamics. 3

RF radio-frequency. 9, 17, 29–34, 58, 95, 97

SM Standard Model of particle physics. 2, 3, 5, 6, 58, 105

SQUID superconducting quantum interference device. 109–111

A Appendix

A.1 Source Code for Spectral Analysis

```python
def analyze_fft(xData, yData, yErr, FF, full=False):
    """
    Analyze an axion of fake axion data set by calculating the amplitude of a sinusoidal model that minimizes the Chi2.
    This is done by analytically solving the linear system of equations of the Chi2 equations for the amplitude.
    In this solver the sums are calculated using FFT, making the algorithm fast on the cost of loosing some accuracy.

    Parameters
    ----------
        xData : 1d array
            independet variable where the data is measured
        yData : 1d array
            dependent data
        yErr : 1d array
            error of the data (standard deviation)
        FF : 1d array
            frequencies to analyze
        full : bool
            set True to return both amplitude values for the sine and cosine part

    Returns
    -------
        amp : 1d array
            amplitude of the fitted sinusoidal for each frequency
        ampErr : 1d array
            error of the amplitude for each frequency
    """

    # get the frequency parameters from the array
    f0 = FF.min()
    df = FF[1] - FF[0]
    Nf = len(FF)

    trig_sum_kwds = None

    # set up arguments to trig_sum
    kwargs = dict.copy(trig_sum_kwds or {})
```

```
    kwargs.update(f0=f0, df=df, use_fft=True, N=Nf)

    # calculate the weights from the errors
    weights = yErr ** -2.0
    W = weights.sum()
    weights /= W

    # Center the data. Even if we're fitting the offset,
    # this step makes the expressions below more succinct
    yData = yData - np.dot(weights, yData)

    # calculate the time shift
    S, C = trig_sum(xData, weights, **kwargs)
    Sh, Ch = trig_sum(xData, weights*yData, **kwargs)
    S2, C2 = trig_sum(xData, weights, freq_factor=2, **kwargs)

    tan_2omega_tau = (S2 - 2 * S * C) / (C2 - (C * C - S * S))

    # compute some parameters with the time-shift
    S2w = tan_2omega_tau / np.sqrt(1 + tan_2omega_tau * tan_2omega_tau)   #
    ↪ sin(2*omega*tau)
    C2w = 1 / np.sqrt(1 + tan_2omega_tau * tan_2omega_tau)                #
    ↪ cos(2*omega*tau)
    Sw = np.sqrt(0.5) * np.sign(S2w) * np.sqrt(1 - C2w)                   #
    ↪ sin(omega*tau)
    Cw = np.sqrt(0.5) * np.sqrt(1 + C2w)                                  #
    ↪ cos(omega*tau)

    # calculate the sums of the analytical solution following Z&K and using P
    ↪ &R
    YC = Ch * Cw + Sh * Sw
    YS = Sh * Cw - Ch * Sw

    CC_hat = 0.5 * (1 + C2 * C2w + S2 * S2w)
    SS_hat = 0.5 * (1 - C2 * C2w - S2 * S2w)
    CC = CC_hat - (C * Cw + S * Sw) ** 2
    SS = SS_hat - (S * Cw - C * Sw) ** 2

    # calculate the phase and amplitude of the signal
    #D = (SS-S*S)*(CC-C*C)

    aa = YS / SS
    bb = YC / CC
    aaErr = np.sqrt(CC_hat) / (CC * np.sqrt(W))
```

```
    bbErr = np.sqrt(SS_hat) / (SS * np.sqrt(W))

    if full:
        return np.array([aa, aaErr]), np.array([bb, bbErr])

    else:
        amp = np.sqrt(aa**2+bb**2)
        ampErr = np.sqrt(aaErr**2*aa**2/(aa**2+bb**2) + bbErr**2*bb**2/(aa**2+bb**2))
        return np.array([amp, ampErr])


def trig_sum(t, h, df, N, f0=0, freq_factor=1,
             oversampling=5, use_fft=True, Mfft=4):
    """
    Compute (approximate) trigonometric sums for a number of frequencies
    This routine computes weighted sine and cosine sums:
        S_j = sum_i { h_i * sin(2 pi * f_j * t_i) }
        C_j = sum_i { h_i * cos(2 pi * f_j * t_i) }
    Where f_j = freq_factor * (f0 + j * df) for the values j in 1 ... N.
    The sums can be computed either by a brute force O[N^2] method, or
    by an FFT-based O[Nlog(N)] method.

    Parameters
    ----------
    t : array_like
        array of input times
    h : array_like
        array weights for the sum
    df : float
        frequency spacing
    N : int
        number of frequency bins to return
    f0 : float (optional, default=0)
        The low frequency to use
    freq_factor : float (optional, default=1)
        Factor which multiplies the frequency
    use_fft : bool
        if True, use the approximate FFT algorithm to compute the result.
        This uses the FFT with Press & Rybicki's Lagrangian extirpolation.
    oversampling : int (default = 5)
        oversampling freq_factor for the approximation; roughly the number of
        time samples across the highest-frequency sinusoid. This parameter
        contains the trade-off between accuracy and speed. Not referenced
```

```
        if use_fft is False.
    Mfft : int
        The number of adjacent points to use in the FFT approximation.
        Not referenced if use_fft is False.

    Returns
    -------
    S, C : ndarrays
        summation arrays for frequencies f = df * np.arange(1, N + 1)
    """

    df *= freq_factor
    f0 *= freq_factor

    if df <= 0:
        raise ValueError("df must be positive")
    t, h = map(np.ravel, np.broadcast_arrays(t, h))

    if use_fft:
        Mfft = int(Mfft)
        if Mfft <= 0:
            raise ValueError("Mfft must be positive")

        # required size of fft is the power of 2 above the oversampling rate
        Nfft = bitceil(N * oversampling)
        t0 = t.min()

        if f0 > 0:
            h = h * np.exp(2j * np.pi * f0 * (t - t0))

        tnorm = ((t - t0) * Nfft * df) % Nfft
        grid = extirpolate(tnorm, h, Nfft, Mfft)

        fftgrid = np.fft.ifft(grid)[:N]
        if t0 != 0:
            f = f0 + df * np.arange(N)
            fftgrid *= np.exp(2j * np.pi * t0 * f)

        C = Nfft * fftgrid.real
        S = Nfft * fftgrid.imag
    else:
        f = f0 + df * np.arange(N)
        C = np.dot(h, np.cos(2 * np.pi * f * t[:, np.newaxis]))
        S = np.dot(h, np.sin(2 * np.pi * f * t[:, np.newaxis]))
```

```python

    return S, C


def bitceil(N):
    """
    Find the bit (i.e. power of 2) immediately greater than or equal to N
    Note: this works for numbers up to 2 ** 64.
    Roughly equivalent to int(2 ** np.ceil(np.log2(N)))
    """

    return 1 << int(N - 1).bit_length()


def extirpolate(x, y, N=None, M=4):
    """
    Extirpolate the values (x, y) onto an integer grid range(N),
    using lagrange polynomial weights on the M nearest points.

    Parameters
    ----------
    x : array_like
        array of abscissas
    y : array_like
        array of ordinates
    N : int
        number of integer bins to use. For best performance, N should be larger
        than the maximum of x
    M : int
        number of adjoining points on which to extirpolate.

    Returns
    -------
    yN : ndarray
         N extirpolated values associated with range(N)

    Example
    -------
    >>> rng = np.random.RandomState(0)
    >>> x = 100 * rng.rand(20)
    >>> y = np.sin(x)
    >>> y_hat = extirpolate(x, y)
    >>> x_hat = np.arange(len(y_hat))
```

```
    >>> f = lambda x: np.sin(x / 10)
    >>> np.allclose(np.sum(y * f(x)), np.sum(y_hat * f(x_hat)))
    True

    Notes
    -----
    This code is based on the C implementation of spread() presented in
    Numerical Recipes in C, Second Edition (Press et al. 1989; p.583).
    """

    x, y = map(np.ravel, np.broadcast_arrays(x, y))

    if N is None:
        N = int(np.max(x) + 0.5 * M + 1)

    # Now use legendre polynomial weights to populate the results array;
    # This is an efficient recursive implementation (See Press et al. 1989)
    result = np.zeros(N, dtype=y.dtype)

    # first take care of the easy cases where x is an integer
    integers = (x % 1 == 0)
    np.add.at(result, x[integers].astype(int), y[integers])
    x, y = x[~integers], y[~integers]

    # For each remaining x, find the index describing the extirpolation range
    ↪ .
    # i.e. ilo[i] < x[i] < ilo[i] + M with x[i] in the center,
    # adjusted so that the limits are within the range 0...N
    ilo = np.clip((x - M // 2).astype(int), 0, N - M)
    numerator = y * np.prod(x - ilo - np.arange(M)[:, np.newaxis], 0)
    denominator = factorial(M - 1)

    for j in range(M):
        if j > 0:
            denominator *= j / (j - M)
        ind = ilo + (M - 1 - j)
        np.add.at(result, ind, numerator / (denominator * (x - ind)))
    return result
```

A.2 Off-Resonance Phase Pick-Up

In this section we explain in more detail the effect of the off-resonance phase pick-up described in Sec. 10.2. In a Ramsey-Type setup, the frequency of the spin-flip signal $\omega_{\rm rf}$ is a free parameter. Usually, $\omega_{\rm rf}$ is set to the resonance frequency ω_0 and the spins are flipped around the axis of the B_1 field. If $\omega_{\rm rf} \neq \omega_0$, there is an additional off-resonance field

$$\Delta B = \frac{\Delta\omega}{\gamma} = \frac{\omega_0 - \omega_{\rm rf}}{\gamma} \; .$$

This field rotates the effective field that the spins see in their laboratory frame away from the B_1 axis according to

$$B_{\rm eff} = \sqrt{B_1^2 + \Delta B^2}$$

The spins now rotate around this effective field which leads to the pick-up of a phase. This behaviour is schematically presented in Fig. 98.

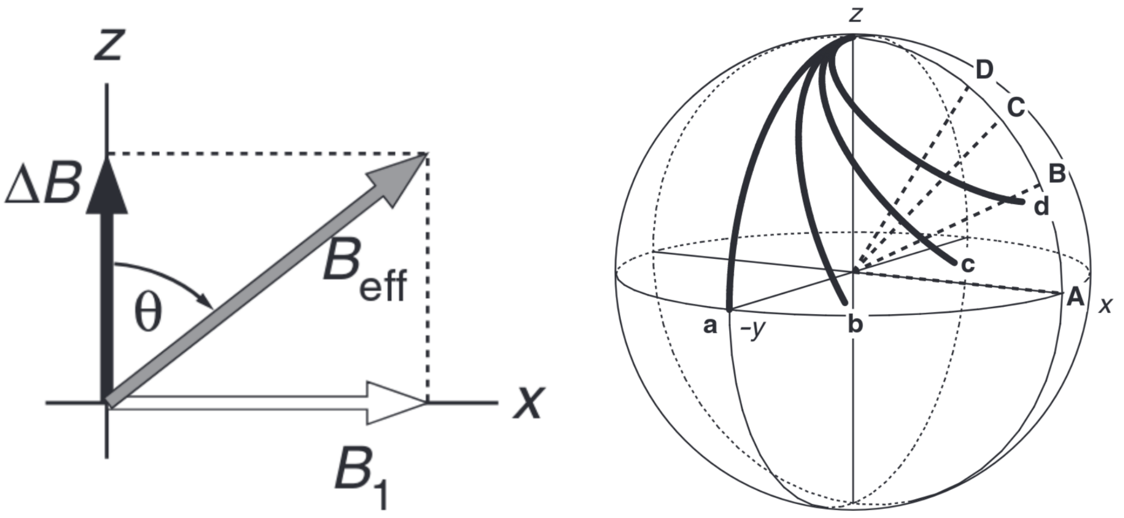

(a) (b)

Figure 98: *(a) Schematic of the effective field axis around which the spins are rotated in their laboratory frame. $\Delta B = (\omega_0 - \omega_{\rm rf}) / \gamma$ is the off-resonance field. (b) Schematic of the path (solid black lines) that the spins follow when flipped in their laboratory frame. The path **a** corresponds to the on-resonance case where the effective field lies along the dashed axis **A**. The other paths **b**, **c**, and **d** correspond to off-resonance fields of various offsets with effective fields along **B**, **C**, and **D**. The schematics are Figs. 3.10 and 3.25 in the lecture notes of J. Keeler in 2002 [125] and the same as Fig. 76 in Sec. 10.2.*

The angle between the effective field and the axis of the main magnetic field can be calculated using one of the following relations

$$\sin(\vartheta) = \frac{B_1}{B_{\text{eff}}},\ \cos(\vartheta) = \frac{\Delta B}{B_{\text{eff}}},\ \tan(\vartheta) = \frac{B_1}{\Delta B}\ .$$

To calculate the phase that the spins pick-up in a $\pi/2$-flip, a spin vector in the z-direction $\vec{s} = (0, 0, 1)$ can be multiplied with a rotation matrix around the effective field direction. A rotation of angle α around an arbitrary unit vector $\hat{\vec{n}}$ can be described by the 3×3-matrix of Eq. (38)

$$\Big[R_{\hat{\vec{n}}}(\alpha)\Big]_{ij} = \Big(1 - \cos(\alpha)\Big) n_j n_j + \cos(\alpha)\delta_{ij} + \sin(\alpha)\epsilon_{ijk} n_k\ ,$$

where δ_{ij} is the Kronecker delta and ϵ_{ijk} is the Levi-Civita symbol.

A.2.1 On-Resonance Case

If the spin-flip signal is driven on resonance, this means that $\omega_0 = \omega_{\text{rf}}$ and $\Delta\omega = 0$. Therefore, the above equations imply that $\Delta B = 0$ and $B_{\text{eff}} = B_1$. This means that the spin is rotated only around the B_1 or the x-axis which simplifies the rotation matrix to

$$R_x(\alpha) = \begin{pmatrix} 1 & 0 & 0 \\ 0 & \cos(\alpha) & -\sin(\alpha) \\ 0 & \sin(\alpha) & \cos(\alpha) \end{pmatrix}\ .$$

For a $\alpha = \pi/2$-flip as common in a Ramsey measurement the rotation matrix becomes

$$R_x(\pi/2) = \begin{pmatrix} 1 & 0 & 0 \\ 0 & 0 & -1 \\ 0 & 1 & 0 \end{pmatrix}\ .$$

If this rotation is applied to the spin-vector in the z-direction $\vec{s} = (0, 0, 1)$, it is flipped to the negative y-axis according to

$$R_x(\pi/2) \cdot \begin{pmatrix} 0 \\ 0 \\ 1 \end{pmatrix}^T = \begin{pmatrix} 0 \\ -1 \\ 0 \end{pmatrix}\ .$$

A.2.2 Off-Resonance Case

If the spin-flip signal is drive slightly off-resonance resulting in a small Ω and, therefore, $B_{\text{eff}} = \sqrt{B_1^2 + \Delta B^2}$. This means the rotation is around the B_{eff} axis which is in the direction of the unit vector $\hat{n} = (B_1, 0, \Delta B)/\sqrt{B_1^2 + \Delta B^2}$. A rotation around an arbitrary vector with angle $\alpha = \pi/2$ is

$$R_{\hat{n}}(\pi/2) = \begin{pmatrix} \frac{B_1^2}{B_{\text{eff}}^2} & -\frac{\Delta B}{B_{\text{eff}}} & \frac{B_1 \Delta B}{B_{\text{eff}}^2} \\ \frac{\Delta B}{B_{\text{eff}}} & 0 & -\frac{B_1}{B_{\text{eff}}} \\ \frac{B_1 \Delta B}{B_{\text{eff}}} & \frac{B_1}{B_{\text{eff}}} & \frac{\Delta B^2}{B_{\text{eff}}^2} \end{pmatrix} ,$$

which applied to the same spin-vector in the z-direction $\vec{s} = (0, 0, 1)$ is

$$R_{\hat{n}}(\pi/2) \cdot \begin{pmatrix} 0 \\ 0 \\ 1 \end{pmatrix}^T = \begin{pmatrix} B_1 \Delta B / B_{\text{eff}}^2 \\ -B_1 / B_{\text{eff}} \\ \Delta B^2 / B_{\text{eff}}^2 \end{pmatrix} .$$

In this case, the spin acquires a phase that is is

$$\varphi = \arctan\left(\frac{s_y}{s_x}\right) = \arctan\left(\frac{-B_1/B_{\text{eff}}}{B_1 \Delta B / B_{\text{eff}}^2}\right) = \arctan\left(\frac{-B_{\text{eff}}}{\Delta B}\right) .$$

This phase can again be written in terms of the angular frequencies

$$\varphi = \arctan\left(\frac{-\sqrt{\omega_1^2 + (\omega_0 - \omega_{\text{rf}})^2}}{\omega_0 - \omega_{\text{rf}}}\right) .$$

A.2.3 Off-Resonance Example

Let's look at an example, where the spins are flipped by $\pi/2$ but with a slightly off-resonance field. The amplitude of the spin-flip signal is $\omega_1 = \gamma B_1$. Therefore, the flipping angle is $\alpha = \omega_1 \tau \overset{!}{=} \pi/2$ with $\tau = l_{\text{sf}}/v$. With typical values of $l_{\text{sf}} = 0.02$ m and $v = 2.35$ m/s this leads to

$$\omega_1 = \frac{\pi v}{2 l_{\text{sf}}} \approx 185 \ \frac{\text{rad}}{\text{s}} . \tag{59}$$

Following our measurements we use a resonance frequency of $\omega_0 = 2\pi \times 991.4$ Hz and a spin-flip signal frequency of $\omega_{\text{rf}} = 2\pi \times 990$ Hz, leading to $\Omega = 2\pi \times 1.4 \text{ Hz} \approx 8.8 \ \frac{\text{rad}}{\text{s}}$. With the equations of Sec. A.2.2 we can calculate the phase to $\varphi_x = -92.5°$ and $\varphi_y = 2.5°$ with respect to the x-axis and the y-axis, respectively.

A.3 Integral Calculation of the Copper Potential

In this section, we calculate the integral of the full copper block from the point-like potential of the individual nucleons. We first recall the point-like potential of Eq. (51) in Sec. 12.

$$V_{\perp}^{\text{point}} = \frac{f_{\perp}}{8\pi m} \frac{e^{-r/\lambda}}{r} \left(\frac{1}{r} + \frac{1}{\lambda} \right) \vec{\sigma} \cdot (\vec{v} \times \vec{r}) \ , \tag{60}$$

To get the potential of the copper sample, we have to integrate over its volume.

$$V_{\perp} = \left(\frac{f_{\perp}^2}{8\pi} \frac{(\hbar c)^2}{mc^2} N \right) \cdot \underbrace{\int_V \vec{\sigma} \cdot \left(\frac{\vec{v}}{c} \times \frac{\vec{r}}{r} \right) \left(\frac{1}{\lambda r} + \frac{1}{r^2} \right) e^{-r/\lambda} \, \mathrm{d}V}_{I} \tag{61}$$

To simplify this calculation we chose the size of the sample such that it can be regarded as an infinite plane. We can calculate the integral in cylindrical coordinates we use that the volume element in these coordinates can be written as

$$\mathrm{d}V = \rho \, \mathrm{d}\varphi \, \mathrm{d}z \, \mathrm{d}\rho \ . \tag{62}$$

A schematic of the used coordinates and variable is shown in Fig. 99.

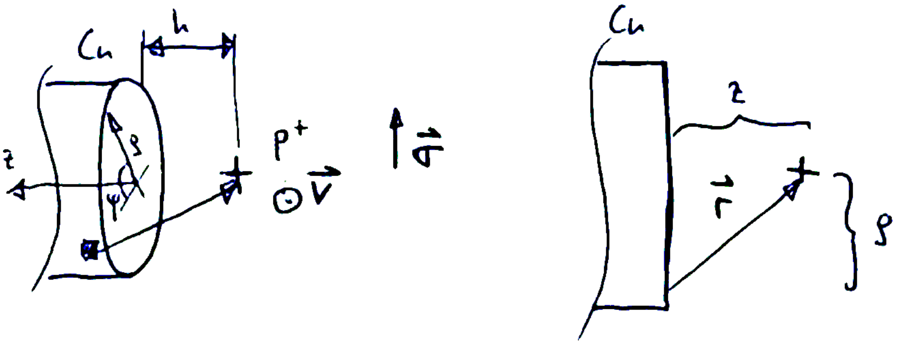

Figure 99: *To perform the integral over the copper volume, cylindrical coordinates are used. A perspective view is sketched on the left, and a side view on the right side. The coordinates and some variables are indicated. The variable $h \equiv \Delta x$ to be consistent with the naming in Sec. 12.*

The integral can be simplified further by using that

$$\vec{\sigma} \cdot \left(\frac{\vec{v}}{c} \times \frac{\vec{r}}{\|\vec{r}\|} \right) = \sigma \frac{v}{c} \frac{z}{\|\vec{r}\|} = \sigma \frac{v}{c} \frac{z}{\sqrt{\rho^2 + z^2}} \ , \tag{63}$$

where we used in the first step that only the z-component of $\vec{r}$ remains since we calculate $\vec{v} \times \vec{r}$ and $\vec{v} \perp \vec{\sigma}$. We further used the definition of the norm $\|\vec{r}\| = \sqrt{\rho^2 + z^2}$. With these transformations the integral becomes

$$I = \frac{\sigma v}{c} \underbrace{\int_0^{2\pi} \mathrm{d}\varphi}_{2\pi} \int_{\Delta x}^{\infty} \mathrm{d}z \int_0^{\infty} \mathrm{d}\rho \; \rho \frac{z}{\sqrt{\rho^2 + z^2}} \left(\frac{1/\lambda}{\sqrt{\rho^2 + z^2}} + \frac{1}{\rho^2 + z^2} \right) e^{-\frac{\sqrt{\rho^2+z^2}}{\lambda}} \quad . \tag{64}$$

We now perform a variable substitution where we define

$$u = \frac{\sqrt{\rho^2 + z^2}}{\lambda}, \; \mathrm{d}u = \frac{\rho}{\sqrt{\rho^2 + z^2}} \frac{1}{\lambda} \, \mathrm{d}\rho, \; \mathrm{d}\rho = \frac{\sqrt{\rho^2 + z^2}}{\rho} \lambda \, \mathrm{d}\rho \; . \tag{65}$$

The integral now becomes

$$I = \frac{2\pi\sigma v}{c} \int_{\Delta x}^{\infty} \mathrm{d}z \int_{z/\lambda}^{\infty} \mathrm{d}u \; \frac{\sqrt{\rho^2 + z^2}}{\rho} \lambda\rho \frac{z}{\sqrt{\rho^2 + z^2}} \left(\frac{1}{u\lambda^2} + \frac{1}{u^2} \frac{1}{\lambda^2} \right) e^{-u} \tag{66}$$

$$= \frac{2\pi\sigma v}{c} \int_{\Delta x}^{\infty} \mathrm{d}z \int_{z}^{\infty} \mathrm{d}u \; \frac{z}{\lambda} \left(\frac{1}{u} + \underbrace{\frac{1}{u^2}}_{\uparrow} \right) \underbrace{e^{-u}}_{\downarrow} \quad . \tag{67}$$

This integral can be calculated by integrating by parts as indicated by the arrows in the above equation.

$$I = \frac{2\pi\sigma v}{c} \int_{\Delta x}^{\infty} \mathrm{d}z \; \frac{z}{\lambda} \frac{\lambda}{z} e^{-z/\lambda} = \frac{2\pi\sigma v}{c} \int_{\Delta x}^{\infty} \mathrm{d}z \; e^{-z/\lambda} = \frac{2\pi\sigma v}{c} \left[-\lambda e^{-z/\lambda} \right]_{\Delta x}^{\infty} \tag{68}$$

$$= \frac{2\pi\sigma v}{c} \lambda e^{-\Delta x/\lambda} \tag{69}$$

Now we can use the result of the integration to get the full potential of the copper sample

$$V_{\perp}\left(\Delta x\right) = \frac{f_{\perp}}{8\pi} \frac{(\hbar c)^2}{mc^2} N \, \frac{2\pi\sigma v}{c} \lambda e^{-\Delta x/\lambda} \tag{70}$$

$$= \frac{f_{\perp}}{4} \frac{\hbar^2}{mc} N \sigma v \lambda e^{-\Delta x/\lambda} \tag{71}$$

The interaction potential is linearly proportional to the proton spins and can be regarded as a pseudo-magnetic field effect

$$V_{\perp} = \frac{1}{2} \gamma_p \hbar \vec{\sigma} \cdot \vec{B}_{\perp} = \frac{1}{2} \gamma_p \hbar \sigma B_{\perp} \; , \tag{72}$$

where we used in the second step that $\vec{\sigma}$ is parallel to $\vec{B}_{\perp}$. This can be solved for $B_{\perp}$, resulting in

$$\begin{aligned} B_{\perp}\left(\Delta x\right) &= \frac{2V_{\perp}\left(\Delta x\right)}{\gamma_{p}\hbar\sigma} = \frac{2}{\gamma_{p}\hbar\sigma}\frac{f_{\perp}\hbar^{2}}{4mc}N\sigma v\lambda e^{-\Delta x/\lambda} \qquad (73) \\ &= \frac{f_{\perp}}{2}\frac{N\hbar v}{\gamma_{p}m_{p}c}\lambda e^{-\Delta x/\lambda} \ , \qquad (74) \end{aligned}$$

which corresponds to Eq. (53) in Sec. 12.1.

B Declaration of Consent

On the basis of Article 18 of the PromR Phil.-nat. 19

Name/First Name:	Ivo Schulthess
Registration Number:	13-918-131
Study Program:	Dissertation
Title of the thesis:	Search for Axion-Like Dark Matter and Exotic Yukawa-Like Interaction
Supervisor:	Prof. Dr. Florian M. Piegsa

I declare herewith that this thesis is my own work and that I have not used any sources other than those stated. I have indicated the adoption of quotations as well as thoughts taken from other authors as such in the thesis. I am aware that the Senate pursuant to Article 36 paragraph 1 litera r of the University Act of September 5th, 1996 and Article 69 of the University Statute of June 7th, 2011 is authorized to revoke the doctoral degree awarded on the basis of this thesis. For the purposes of evaluation and verification of compliance with the declaration of originality and the regulations governing plagiarism, I hereby grant the University of Bern the right to process my personal data and to perform the acts of use this requires, in particular, to reproduce the written thesis and to store it permanently in a database, and to use said database, or to make said database available, to enable comparison with theses submitted by others.

Place/Date:

Signature: